Mathematical Analysis of Ferrofluid

By

Noor Muhammad

Department of Mathematics
Quaid-I-Azam University
Islamabad, Pakistan
2020

Mathematical Analysis of Ferrofluid

By

Noor Muhammad

Supervised By

Prof. Dr. Sohail Nadeem

Department of Mathematics
Quaid-I-Azam University
Islamabad, Pakistan
2020

Mathematical Analysis of Ferrofluid

By

Noor Muhammad

A THESIS SUBMITTED IN THE PARTIAL FULFILLMENT OF THE REQUIREMENT FOR THE DEGREE OF

DOCTOR OF PHILOSOPHY

IN

MATHEMATICS

Supervised By

Prof. Dr. Sohail Nadeem

Department of Mathematics
Quaid-I-Azam University
Islamabad, Pakistan
2020

Certificate of Approval

This is to certify that the research work presented in this thesis entitled **_Mathematical Analysis of Ferrofluid_** was conducted by **_Mr. Noor Muhammad_** under the kind supervision of **_Prof. Dr. Sohail Nadeem_**. No part of this thesis has been submitted anywhere else for any other degree. This thesis is submitted to the Department of Mathematics, Quaid-i-Azam University, Islamabad in partial fulfillment of the requirements for the degree of Doctor of Philosophy in field of Mathematics from Department of Mathematics, Quaid-I-Azam University Islamabad, Pakistan.

Student Name: **Noor Muhammad**　　　　　Signature:_____

External committee:

a) **External Examiner 1**:　　　　　　　　Signature:_____
   Name: **Dr. Muhammad Mushtaq**
   Designation: Assistant Professor
   Office Address: Department of Mathematics, COMSATS University, Park Road, Chak Shahzad, Islamabad.
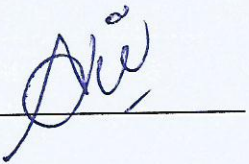
b) **External Examiner 2**:　　　　　　　　Signature:_____
   Name: **Dr. Tariq Javed**
   Designation: Associate Professor
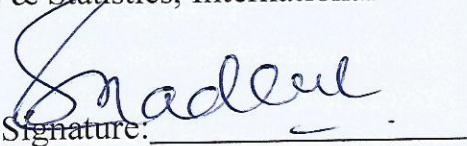   Office Address: Department of Mathematics & Statistics, International Islamic University, H-10, Islamabad.

c) **Internal Examiner**　　　　　　　　　Signature:_____
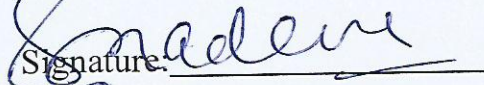   Name: **Prof. Dr. Sohail Nadeem**
   Designation: Professor
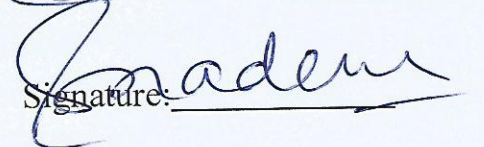   Office Address: Department of Mathematics, QAU Islamabad.

   Supervisor Name:　　　　　　　　　Signature:_____
   Prof. Dr. Sohail Nadeem

   Name of Dean/ HOD　　　　　　　　Signature:_____

   Prof. Dr. Sohail Nadeem

Mathematical Analysis of Ferrofluid
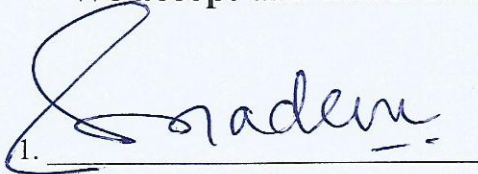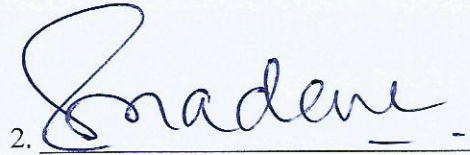
By

Noor Muhammad

CERTIFICATE

A THESIS SUBMITTED IN THE PARTIAL FULFILLMENT OF THE REQUIREMENTS FOR THE DEGREE OF THE DOCTOR OF PHILOSOPHY
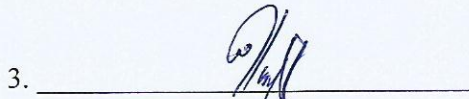
We accept this thesis as conforming to the required standard
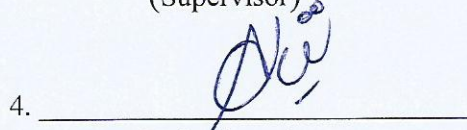
1. _____
   Prof. Dr. Sohail Nadeem
   (Chairman)

2. _____
   Prof. Dr. Sohail Nadeem
   (Supervisor)

3. _____
   Dr. Muhammad Mushtaq
   Department of Mathematics,
   COMSATS University Park
   Road, Chak Shahzad, Islamabad.
   (External Examiner)

4. _____
   Dr. Tariq Javed
   Department of Mathematics &
   Statistics, International Islamic
   University H-10, Islamabad
   (External Examiner)

Department of Mathematics
Quaid-I-Azam University
Islamabad, Pakistan
2020

Author's Declaration

I, *Noor Muhammad*, hereby state that my PhD thesis titled *Mathematical Analysis of Ferrofluid* is my own work and has not been submitted previously by me for taking any degree from Quaid-I-Azam University Islamabad, Pakistan or anywhere else in country/world.

At any time, if my statement is found to be incorrect even after my graduation the university has the right to withdraw my PhD degree.

Name of student: Noor Muhammad

Dated: 20-01-2020

Plagiarism Undertaking

I solemnly declare that research work presented in the thesis titled *"Mathematical Analysis of Ferrofluid"* is solely my research work with no significant contribution from any other person. Small contribution/help wherever taken has been duly acknowledged and that complete thesis has been written by me.

I understand the zero tolerance policy of the HEC and **Quaid-i-Azam University** towards plagiarism. Therefore, I as an Author of the above titled thesis declare that no portion of my thesis has been plagiarized and any material used as reference is properly referred/cited.

I undertake that if I am found guilty of any formal plagiarism in the above titled thesis even afterward of PhD degree, the University reserves the rights to withdraw/revoke my PhD degree and that HEC and the University has the right to publish my name on the HEC/University Website on which names of students are placed who submitted plagiarized thesis.

Student/Author Signature

Name: **Noor Muhammad**

Acknowledgments

Contents

List of Figures

List of Tables

Nomenclature			
u, v	Velocity components, m/s	T	Temperature, K
U_w, U_e	velocity at boundaries, m/s	x, y	Cartesian coordinates, m
μ	Dynamic viscosity, $kg/(ms)$	ρ	Density, kg/m^3
P	Pressure, Pa	α	Thermal diffusivity, m^2/s
h_s	Heat transfer coefficient, $W/(m^2K)$	K	Thermal conductivity
T_c	Curie temperature, K	ν	Kinematic viscosity, m^2/s
T_0	Reference temperature, K	c_p	Specific heat capacity, $J/(kgK)$
k_s, k_1	Rate constants, $L/(mol.s)$	M	Magnetization, A/m
H	Magnetic field, $tesla$	γ_1	Dipole moment per unit length, $J/T.m$
μ_0	Magnetic permeability, N/A^2	δ	Boundary layer thickness, m
Ω	Magnetic scalar potential, $tesla$	b_1, b_2	Dimensional constant, K/m
K_p	pyromagnetic coefficient, $Wb/(m^2K)$	T_∞	Ambient temperature, K
Re	Reynolds number	τ_w	Wall shear stress, N/m^2
C_f	Skin friction coefficient	Nu_x	Nusselt number
λ_1	Ratio of relaxation to retardation times, s	λ_2	Retardation time
Q, S	Dimensionless constants, $1/s$	α_1	Normal stress moduli
ϵ	Porosity of porous medium, $1/m$	k_2	permeability of porous medium, m
A, B, C	Chemical species, $1/m$	a, b, c	Concentrations of Chemical species
a_0	Constant concentration	H_x, H_y	Components of magnetic dipole, $tesla$
l	Reference length, m	φ	solid volume fraction
μ_{nf}	Dynamic viscosity of nanofluid, $kg/(ms)$	k_{nf}	thermal conductivity of nanofluid W/mK
$(\rho c_p)_{nf}$	Heat capacitance of nanofluid, J/kgK	ρ_{nf}	Density of nanofluid, kg/m^3

$(\rho c_p)_f$	Heat capacitance of base fluid, J/kgK	ρ_f	Density of base fluid, kg/m^3
$(\rho c_p)_s$	Heat capacitance of solid particle, J/kgK	ρ_s	Density of solid particle, kg/m^3
μ_s	Dynamic viscosity of solid particle, $kg/(ms)$	k_s	thermal conductivity of solid particle, W/mK
μ_f	Dynamic viscosity of base fluid, $kg/(ms)$	k_f	thermal conductivity of base fluid, W/mK
$C_2H_6O_2$	Ethylene glycol	$NiZnFe_2O_4$	Nickel ZINC ferrite
$MnZnFe_2O_4$	Manganese ZINC ferrite	Fe_3O_4	Magnetite ferrite
H_2O	Water	δ_1,δ_2	Ratio of diffusion coefficients

Chapter 1

Introduction

Introduction

An incredible consequence of boundary layer flows can be watched in the environment where liquid and surface are in direct contact. The development of thin boundary layer [1] transpired where the liquid adjust speed of the body because of drag/friction forces. Influence of such forces is smaller inside the laminar region as compare to turbulence region. Recently, the scientists and researchers are interested to arise the rate of cooling or heating and reduce the friction drag in the advanced technological procedures. Thus different models were constructed for the reduction of drag forces or friction drag, for example, flows through the tail surface of plane, wing, and wind turbine rotor, etc. Although, the friction drag can be decreased by maintaining boundary layer beyond the separation and maintain a secure connection to slow the transition of the laminar to turbulent flow. This function can be accomplished by cause of distinct physical objectives like fluid injection and suction, through moving the surface, and the existence of different body forces. Likewise, the scientists have developed different types of boundary conditions that are applicable in the enhancement of rate of heating/cooling over the surface. Thus, the aim of the analysis concentrates on the reduction of friction drag and enhancement of rate of heating.

The heat transport phenomena due to stretching sheets through the ambient fluid are characterized and reported widely in the modern literature survey. Characteristics of products and materials obtained through engineering and industrial processes, mostly depend on the structure and nature of fluid away from a sheet and also on stretching rate. As the unpredictable change in temperature of the extrudate or the rapid stretching may demolish the expected quality and characteristics of the resulting product, as well as, the heat transfer rate essential to be synchronized carefully. To overcome these difficulties, ambient fluids with significant electromagnetic characteristics are of great curiosity as their flow could be synchronized by the extrinsic magnetic field applied outside from the working fluid. In such situations, ferrofluids are significant in stabilizing the flow of heat. Ferrofluids are fluids that are synthesized in an artificial way and composed of extremely condensed suspensions of narrow magnetic/ferrite particles in a transporter liquid. These fluids perform like usual fluids except magnetization force. Ferrohydrodynamics studies the behavior of motion of magnetic fluid affected by magnetic polarization forces. In heat transfer equipment liquids are frequently utilized as heat transporter. Some examples of consequential benefits of heat transfer liquids involve avionics and vehicular cooling systems in different industries, cooling and hydronic heating systems in buildings, textile, papers, foods, and chemicals. In everything described, thermal conductivity of liquids that

transfer of heat are important in the construction of profitable heat transport material. As global competition intensifies, factories needs to construct improved heat transfer liquids consequentially larger thermal conductivities than are currently available. However, the existing literature on thermal conductivity restricted to micrometer or milimeter-sized particles until 1881. Maxwell's theory [2] demonstrates that introducing ferrite/magnetic spherical particles accelerates thermal conductivity of different suspensions. It is suggested that adding nano-meter sized ferrite/metallic particles in heat transfer liquids e.g., engine oil, water, ethylene glycol, or ethanol to form to a new subclass of fluids along enormous thermal conductivity, the resulting fluid is termed as nanofluid. Nanofluids display better quality when compared with fluids containing micrometer-sized particles and conventional heat transfer liquids. Since heat transfer results on the wall of the particles, it needs to be used nanoparticles with considerable surface area. Ferrite/Nanoparticles have sufficiently large surface area as compare to micrometer-sized particles, and therefore nanofluids have extensive potential for application [3–21] in heat transfer.

Ferrofluids are colloidal liquids made of ferrimagnetic or ferromagnetic ferrite nanoparticles slanged in an electrically non-conducting carrier fluid. In ferromagnetic nanofluids hyperthermia, ferrites nanoparticles of various types like $MnZnFe_2O_4$, Fe_3O_4, and $NiZnFe_2O_4$ or even of hematite are infused in tumor and afterward subjected under enormous magnetic field frequency. These ferrite nanoparticles yield heat that regularly enhances tumor temperature, which can kill cancer cell [22]. A well-tempered of these ferrites are, therefore, characterized by containing the iron atoms situated at the origins of octahedra of oxygen atoms and zinc atoms originated in tetrahedra of oxygen atoms. Characteristically, the normal spinel are paramagnetic and the inverted spinel are ferromagnetic at the room temperature. Further, at low temperature zinc ferrites behave like antiferromagnetic. Ferrofluids do not hold magnetization in the absence of a magnetic dipole and are classified into superparamagnets. A remarkable feature of the ferromagnetic nanofluids is the reliance of magnetization on the temperature and this thermomagnetization coupling makes ferromagnetic nanofluids more applicable in diverse practical applications [23–36]. The impacts of magnetic and thermal field gradients on saturated viscous ferrofluid flow was explored by Neuringer et al. [37]. Crane [38] initiated the Newtonian fluid flow with linear stretching, which later on reduced to non-Newtonian fluids. Anderson and Valnes [39] inspected the work of Crane's for non-conducting viscous ferrofluid. He described the consequence of magnetic field caused by magnetic dipole over a stretching surface (shear driven motion) finalized that influence of magnetic field was to deceler-

ate the movements of liquid particles instead of a hydrodynamic case. The characteristics of localized magnetic field over a free and force convective magnetic fluid flow are scrutinized by Tzirtzilakis et al. [40] and got numerical results for sundry materialized parameters. Impacts of dust particles on ferrofluid with convective porous medium were characterized by Sharma et al. [41]. Zeeshan and Majeed characterized the impacts of magnetic dipole and suction/injection in a Jeffrey fluid flow past a stretchable surface [42]. Sharma et al. [43] explored the influence of dust particles in a ferrofluid with thermal convection. A notable fascinating characteristic of ferrofluids is that magnetization is a function of temperature such characteristic put up ferrofluids more competent in diverse applications. On the motive of electromagnetism, Neuringer and Rosensweig [44] expressed that $\mu_0 \left(\mathbf{M}.\nabla \right) \mathbf{H}$ (magnetic force per unit volume) becomes $\mu_0 \mathbf{M} \nabla \mathbf{H}$ if the subsequent assumptions are stated in a way (i) The direction of $\mathbf{H}$ (magnetic field) of a fluid will be the direction of magnetization $\mathbf{M}$, (ii) the liquid will be non-conductive and (iii) the assumption of displacement current is considered insignificent. In this fashion, ferrohydrodynamics need continuation and existence of a spatially extended field, whereas this is not required in case of magnetohydrodynamics. The viscous ferromagnetic liquid induced by eccentric cylinder along transfer of heat was scrutinized by Kim et al. [45]. Majeed et al. [46] scrutinized the flow of heat in a viscoelastic ferrofluid with an external magnetic dipole. The higher heat transfer were scrutinized in the analysis. Hussanan et al. [47] scrutinized inertial and microstructure features in presence of effective thermal conductivity for the investigation of transferring heat in a magnetite ferrofluid. The influence of friction drag on magnetohydrodynamic rotating ferrofluid past a shrinking/stretching wall was deliberated by Jusoh et al. [48]. Reduction in friction drag was depicted in the analysis for the case of ferrofluid in presence of nonlinear stretching velocity. Experimental analysis of the forced convective ferromagnetic fluid saturated in a magnetizable/non-magnetizable porous media was incorporated by Shafii and Keshavarz [49]. Entropy generation in a magnetohydrodynamic ferrofluid in a cavity having porous medium was examined by Astanina et al. [50].

The viscous materials with the phenomena of thermal stratification has achieved lot of importance among the researchers. Naviers-Strokes expressions are stated to implement certain characteristics of viscous materials. Further, thermal stratification with viscous/Newtonian materials is functional in several engineering and manufacturing processes. It originates in flows due to dissimilar densities of fluids or change in their temperature difference. The relevant examples of thermal stratification include oceans and lakes stratification, ground water reservoirs, salinity in rivers, industrial

oceans, estuaries and food manufacturing processes. It is applicable in lakes since it influences the temperature difference between oxygen and hydrogen. In this direction, thermal stratification is useful in heat transfer. Van Atta [51] characterized the degeneration of turbulence region in the viscous thermally stratified flow. Foisal and Alam [52] deliberated magnetohydrodynamic thermally stratified fluid flow over an inclined plate with high porosity medium. Antoniadis and Papalexandris [53] scrutinized shear flows in pure-fluid domains and superposed porosity with thermal stratification and got the solution via numerical technique. Heat transfer and its impacts on the viscous dissipation and stratification in the flow of a magnetohydrodynamic nanofluid was inspected by Besthapu et al. [54]. Rehman et al. [55] investigated numerically the convection and thermal stratification and its influence on the Casson fluid. Thermal stratification and its impacts on the flow of heat in a two phase γAl_2O_3-$C_2H_6O_2$ and γAl_2O_3-H_2O nanofluid was evaluated by Ahmed et al. [56]. Makinde et al. [57] analyzed the flow of heat in a thermally stratified magnetohydrodynamic Casson fluid along a horizental sheet in presence of Lorentz forces. The analysis of non-linear thermal radiation and its impacts on the chemically reactive Eyring-Powell water-alumina nanofluid in presence of thermal stratification was scrutinized by Koriko et al. [58]. Karim et al. [59] examined the cooling and heating performance in a storage tank along thermal stratification. Paradis et al. [60] scrutinized coiled heat exchanger and thermal storage tank via uni-dimensional model for thermal stratification. Enhancement of thermal stratification in a heated water storage tank was inspected due to an exterior device by Gomez et al. [61]. Some relevant applications to thermal stratification may be seen in [62–67].

Merkin [68] specified four common ways through which temperature distribute from wall to ambient fluid, i.e., (i) prescribed surface heat flux distributions, (ii) prescribed wall temperature distributions, (iii) conjugate conditions, and (iv) Newtonian heating. In conjugate condition, heat flow from a bounding wall of finite heat capacity and thickness. The interface temperature relays on the underlying characteristics of the system, i.e., thermal conductivity of solid particle and liquid. On the other hand, in Newtonian heating, the rate of transfer of heat from the bounding wall (of finite heat capacity) is relative to wall temperature. It is also known as conjugate convective flow. Later on, Salleh et al. [69] scrutinized the flow of heat in viscous fluid flow by incorporating Newtonian heating at the surface. Qasim et al. [70] depicted the Newtonian heating and its impacts in the micropolar fluid flow. Sarif et al. [71] demonstrated numerical simulation via Keller box method to analyze the Newtonian heating and its influence on the liquid flow. Nadeem et al. [72] examined viscoelastic

fluid by taking Newtonian heating at the sheet and analyzed heat transfer for the flow of fluid. Imran et al. [73] scrutinized generalized Maxwell magnetohydrodynamic fluid flow past a nonlinear stretched surface via Newtonian heating. Kamran and Wiwatanapataphee [74] inspected the micropolar chemically reactive species along second order slip past a stretched sheet along Newtonian heating. The impacts of transverse thermophoretic effect in the flow of magnetohydrodynamic fluid along Newtonian heating is evaluated by Mehmood et al. [75]. Newtonian heating and Hall current effects on convective micropolar magnetohydrodynamic liquid flow over a surface are dissected by Kamran et al. [76]. Hussanan et al. [77] scrutinized the transfer of mass and heat in a micropolar nano-fluid by incorporating Conjugate parameter at the wall. Applications of Newtonian heating available in the literature [77–82].

The packed bed tabular reactions of cooled or heated walls are usually employed in industry to accomplish heterogeneous or homogeneous catalytic reactions, which can be endothermic or exothermic. In gas-solid transport-reaction mechanisms, reaction takes place within the solid phase, within liquid phase, or at liquid interface. Reaction between atoms/molecules of sundry coefficients can take place during their collision and or a third distinct atom/molecule may be sufficient for a reaction to occur. Several chemical reactions proceed slowly, on not at all, except in the presence of a catalyst. A survey of the chemical aspects of heterogeneous, or surface reactions has been characterized by Scott [83] and Gray and Scott [84]. A full talk of catalysis and the interpretation of several practical applications mentioned herein [85–87]. A heterogeneous mixture includes of either or both of (i) hydrophilic and hydrophobic materials in a unique mixture, or (ii) sundry conditions of matter; hydrophilic and hydrophobic materials would be a mixture of silicone grease, octane, and water. Fluids, solids, heterogeneous, and gasses might be made homogeneous by mixing, melting, or by permitting time to go for diffusion to appropriate the atoms/molecules equitably. For instance, mixing dye to water will make a heterogeneous solution, however, later on, it reduced to a homogeneous. These reactions are important in several chemically reacting procedures. Merkin [88] initiated the chemically reactive species in the flow induced by stretched surface. The friction drag in a chemically reactive species was scrutinized by Chaudhary and Merkin [89]. Bachok et al. [90] characterized nanofluid flow along chemically reactive species. Kameswaran et al. [91] expressed heat transfer in a chemically reactive species along nanofluid. Khan and Pop [92] deliberated the flow of heat in a chemically reactive species.

Keeping the above importance in mind, this thesis is arranged in the following manner:

In chapter one, a brief discussion is made about heat transfer along friction drag in liquid flows and their applications are further discussed.

Chapter two is devoted to "Heat transfer analysis of a thermally stratified ferromagnetic fluid". In this chapter transfer of heat is explored for the ferromagnetic fluid along thermal stratification. Magnetic dipole is taken to reduce the turbulence in the flow. Temperature field, axial velocity, and heat transfer along friction drag are discussed analytically. Contents of the chapter are published in "Proceedings of the Institution of Mechanical Engineers, Part E: Journal of Process Mechanical Engineering" (2018) 0954408918759244.

Chapter three demonstrates "Evaluation of Fourier's law in a ferrofluid in porous medium". Characteristics of thermomechanical coupling are computed. Heat transfer is implemented for the Jeffrey ferromagnetic fluid along thermal stratification and porous medium. Porous medium play important role in controlling heat transfer. For larger ratio parameter, the drag coefficient at the surface declines. Contents of the chapter are published in "Results in Physics" 7 (2017) $2361 - 2368$.

Chapter four characterizes "Analysis of friction drag and heat transfer in a ferrofluid". Influence of magnetic dipole in a second grade ferrofluid induced by linear stretching sheet is scrutinized in this chapter. Thermal stratification has consequential impacts in controlling transfer of heat. Magneto-thermomechanical interaction decelerates the motion of the fluid. The contents of the chapter are published in "Results in Physics" 7 (2017) $854 - 861$.

Chapter five examines "Hybrid isothermal model for the ferrohydrodynamic chemically reactive species". Influence of Newtonian heating in a ferrofluid is analyzed for three chemical species. Heat flux is examined by incorporating Fourier's law for heat. The analysis is carried out for equal diffusion coefficients of all autocatalyst and reactions. Heat transfer rate and friction drag are depicted for the ferrohydrodynamic chemically reactive species. Contents of the chapter are published in "Communications in Theoretical Physics".

Chapter six reveals "Ferrite nanoparticles $MnZnFe_2O_4$, Fe_3O_4 and $NiZnFe_2O_4$ in flow of ferromagnetic nanofluid". The presence of ferrite nanoparticles enhances the transfer of heat in boundary layer flows. To control thermal and momentum boundary layer thickness, magnetic dipole is introduced in the flow. Solid volume fraction arises the rate of flow of heat situated on the boundary layer is incorporated. The contents of the chapter are published in "The European Physical Journal Plus" 132(9) (2017) 377.

Chapter seven is devoted to "Impacts of ferrite nanoparticles in viscous ferromagnetic nanofluid". Theoretical scrutiny is conducted to demonstrate the heat transfer of six distinct ferromagnetic $C_2H_6O_2$-$MnZnFe_2O_4$ (ethylene glycol-manganese zinc ferrite), $NiZnFe_2O_4$-$C_2H_6O_2$ (nickel zinc ferrite-ethylene glycol), $C_2H_6O_2$-Fe_3O_4 (ethylene glycol-magnetite ferrite), H_2O-$NiZnFe_2O_4$ (water-nickel zinc ferrite), H_2O-$MnZnFe_2O_4$ (water-manganese zinc ferrite), and Fe_3O_4-H_2O (magnetite ferrite-water) nanofluids. Heat transfer enhancement is observed in presence of these ferrite nanoparticles. The contents of the chapter are published in "PloS one" 13(1) (2018) e0188460.

Chapter 2

Heat transfer analysis of a thermally stratified ferromagnetic fluid

2.1   Introduction

This chapter delineates on the transferring of heat in a viscous ferrofluid. The analysis is examined in presence of an external magnetic dipole. The investigation is disclosed by the phenomenon of thermal stratification and stagnation point. Conservation of linear momentum and mass is used to develop expressions of ferrohydrodynamic problem. Heat flux is assessed by employing the Fourier's law of heat. Optimal HAM (Homotopy Analysis Method) and Bvph2-midpoint techniques are employed in the evaluation of the consequence of magneto-thermomechanical coupling on ferrohydrodynamic flow. The impacts of distinct parameters on distribution of temperature and velocity field are depicted by virtue of graphs. Numerical values and graphical results of friction drag and heat transfer rate corresponding to involuted parameters have been discussed and computed. Further, the ferrohydrodynamic parameter declines the axial velocity thereby enhances the temperature profile. From the analysis of thermodynamics, it is determined that the transport of energy occurred because of the interactions of a system with its surrounding.

2.2   Ferrohydrodynamic and thermal energy equations

The characteristics of a steady, electrically nonconducting and an incompressible two-dimensional ferrofluid over an impermeable linear stretching sheet are incorporated. By exerting a force on the sheet located at $y = 0$ introduces stretching in the sheet having velocity $U_w(x)$ (See Figure 3.1). The resulting stretching in the sheet is proportional to length from origin. Further, magnetic dipole is placed outside the surface. A magnetic dipole is placed in the framework whose center is kept on vertical axis at distance d from surface positioned at $y = 0$. The magnetic field points of magnetic dipole are taken along positive $x-$axis. An enhancement in the strength of magnetic field due to magnetic dipole leads to saturate the ferrofluid. The Curie temperature is greater than wall temperature is hypothesized, additionally, the temperature $T = T_\infty$ is assumed to be fluid temperature away from the surface, where $T_\infty < T_w < T_c$. The fluid above Curie temperature is incompetent of magnetization, $T_w = T_0 + b_1 x$ and $T_\infty = T_0 + b_2 x$ are respectively evaluated as the variable temperature at the surface and away from surface. The impacts of heat generation/absorption are considered to be negligible. Making use of boundary layer ap-

proximations ($v = O(\delta) = y, u = O(1) = x$), the governing equations in a ferrofluid become

$$\frac{\partial u}{\partial x} + \frac{\partial v}{\partial y} = 0, \tag{2.1}$$

$$u\frac{\partial u}{\partial x} + v\frac{\partial u}{\partial y} = -\frac{1}{\rho}\frac{\partial P}{\partial x} + \frac{\mu_0 M}{\rho}\frac{\partial H}{\partial x} + \frac{\mu}{\rho}\frac{\partial^2 u}{\partial y^2}, \tag{2.2}$$

$$u\frac{\partial T}{\partial x} + v\frac{\partial T}{\partial y} - \frac{\mu_0 K_p T}{\rho c_p}\left(u\frac{\partial H}{\partial x} + v\frac{\partial H}{\partial y}\right) = \alpha\frac{\partial^2 T}{\partial y^2}. \tag{2.3}$$

Here ρ display the density, (u, v) signify velocity components along (x, y) directions respectively, α exemplify the thermal diffusivity, ν signifies kinematic viscosity, P indicates the pressure, c_p represents the specific heat, whereas, H represents the magnetic field, μ_0 signify magnetic permeability, K_p denotes the pyromagnetic coefficient, T symbolizes the temperature, and M denotes the magnetization. The assumed admissible boundary conditions are of the form

$$u|_{y=0} = U_w(x) = Sx, v|_{y=0} = 0, T|_{y=0} = T_w = T_0 + b_1 x, \tag{2.4}$$

$$u|_{y\to\infty} \to U_e(x) = Qx, T|_{y\to\infty} \to T_c = T_0 + b_2 x. \tag{2.5}$$

Here $U_w(x)$ characterizes the velocity due to stretching, whereas T_∞ identifies temperature of ambient fluid, whereas, b_1 and b_2 are dimensional constants.

2.3   Magnetic dipole

The impact of magnetic field driven by magnetic dipole influences the flow of ferrofluid. Such impact can be described by a well known function named as magnetic scalar potential, which is expressed as

$$\Omega = \frac{\gamma_1}{2\pi}\frac{x}{(y + d)^2 + x^2}, \tag{2.6}$$

here γ_1 symbolizes the dipole moment per unit length, ampere turns meter is dimension of γ_1, the components for the magnetic field are

$$H_x = -\frac{\partial\Omega}{\partial x} = -\frac{\gamma_1}{2\pi}\frac{-(y + d)^2 + x^2}{\left(x^2 + (y + d)^2\right)^2}, \tag{2.7}$$

$$H_y = -\frac{\partial \Omega}{\partial y} = \frac{\gamma_1}{2\pi} \frac{2x(y+d)}{\left((y+d)^2 + x^2\right)^2}. \tag{2.8}$$

Since it is generally known that the magnetic body force is relative to magnetic field gradient of H, we thus have

$$H = \sqrt{\left(\frac{\partial \Omega}{\partial x}\right)^2 + \left(\frac{\partial \Omega}{\partial y}\right)^2}. \tag{2.9}$$

Using Eqs. (2.7) and (2.8) in Eq. (2.9), we obtain the following equations

$$\frac{\partial H}{\partial x} = -\frac{\gamma_1}{\pi} \frac{x}{(y+d)^4}, \tag{2.10}$$

$$\frac{\partial H}{\partial y} = \frac{\gamma_1}{\pi} \left(\frac{2x^2}{(y+d)^5} - \frac{1}{(y+d)^3}\right). \tag{2.11}$$

The linear relation of state approximates the impact of magnetization with temperature given below

$$M = K_p(T_c - T). \tag{2.12}$$

The ferrofluid flow and its physical geometry is revealed in Figure 2.1.
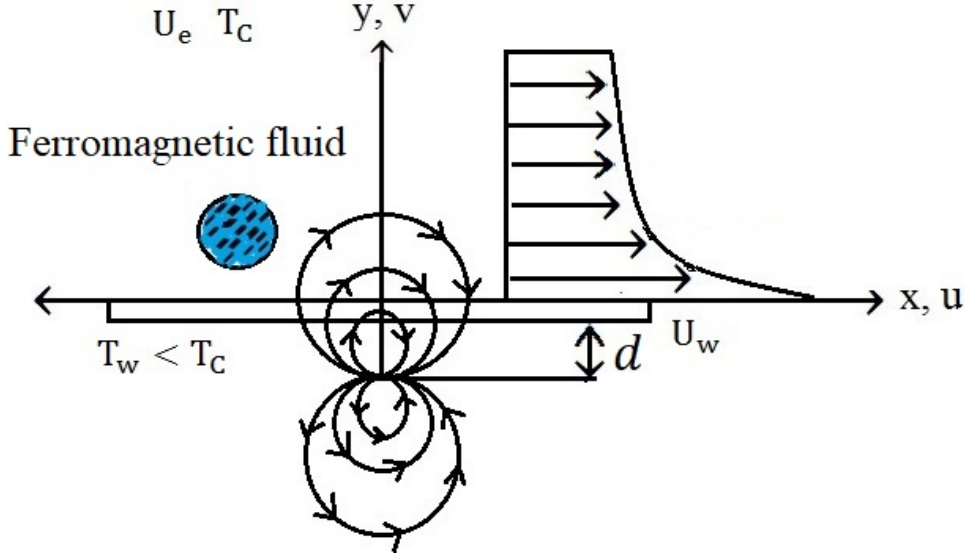
Figure 2.1: Geometry of the flow.

2.4   Solution procedure

Here, we introduced the dimensionless variables

$$\psi(\eta, \xi) = \eta(\frac{\mu}{\rho})f(\xi), \theta(\xi, \eta) \equiv \frac{T_c - T}{T_w - T_0} = \theta_1(\xi) + \eta^2\theta_2(\xi). \tag{2.13}$$

Here $\theta_2(\xi)$ and $\theta_1(\xi)$ exhibit dimensionless temperature, the corresponding dimensionless coordinates are

$$\xi = y\sqrt{\frac{\rho S}{\mu}}, \quad \eta = x\sqrt{\frac{\rho S}{\mu}}. \tag{2.14}$$

The stream function is defined in this fashion that the mass equation satisfies directly, in which the function $\psi(\eta, \xi)$ signifies the stream function, (u, v) symbolize the comparable components of velocity. The velocity stream function relation are defined as

$$u = \frac{\partial\psi(\eta, \xi)}{\partial y} = Sxf'(\xi), v = -\frac{\partial\psi(\xi, \eta)}{\partial x} = -\sqrt{S\nu}f(\xi). \tag{2.15}$$

Employing the similarity transformations given in Eqs. (2.6) to (2.12) and (2.13) to (2.15), Eqs. (2.2) and (2.3) together with the aforesaid boundary conditions given in Eqs. (2.4) and (2.5) transform to the system defined below

$$f''' - f'^2 + ff'' - \frac{2\beta\theta_1}{(\xi + \gamma)^4} + R^2 = 0, \tag{2.16}$$

$$\theta_1'' + Prf\theta_1' + \frac{2\lambda\beta \ f(\theta_1 - \varepsilon)}{(\xi + \gamma)^3} + 2\theta_2 - 4\lambda f'^2 = 0, \tag{2.17}$$

$$\theta_2'' - Pr(2f'\theta_2 - f\theta_2') + \frac{2\lambda\beta \ f\theta_2}{(\xi + \gamma)^3} - 4\lambda f''^2$$
$$+ \beta\lambda \ (\varepsilon - \theta_1)\left(\frac{2f'}{(\xi + \gamma)^4} + \frac{4f}{(\xi + \gamma)^5}\right) = 0, \tag{2.18}$$

$$f'(\xi) = 1, f(\xi) = 0, \theta_1(\xi) = 1 - S_1, \theta_2(\xi) = 0, \quad at \ \ \xi = 0, \tag{2.19}$$

$$f'(\xi) \to R, \theta_1(\xi) \to 0, \theta_2(\xi) \to 0, \quad when \ \ \xi \to \infty. \tag{2.20}$$

In above equations, the parameters β (ferrohydrodynamic interaction), S_1 (thermal stratified parameter), λ (viscous dissipation), R (ratio), ε (Curie temperature), and Pr (Prandtl number) are defined as

$$R = \frac{Q}{S}, Pr = \frac{\nu}{\alpha}, \varepsilon = \frac{T_c}{T_w - T_0}, \beta = \frac{\gamma_1}{2\pi} \frac{\mu_0 K_p (T_w - T_0)\rho}{\mu^2},$$

$$\lambda = \frac{S\mu^2}{\rho K_p (T_w - T_0)}, \gamma = \sqrt{\frac{S\rho d^2}{\mu}}, S_1 = \frac{b_2}{b_1}. \tag{2.21}$$

At the walls, the framework of engineering interest, i.e., the friction drag and rate of heat transfer are

$$C_f = \frac{2\tau_w}{\rho U_w^2}, \ \tau_w = \mu \frac{\partial u}{\partial y}\Big|_{y=0}, \ Nu_x = (\frac{x}{T_w - T_0})\frac{\partial T}{\partial y}\Big|_{y=0}. \tag{2.22}$$

We finally achieved the following non-dimensional equations

$$\frac{1}{2} Re^{1/2} C_f = f''(0), \ Re^{-1/2} Nu_x = -(\theta_1'(0) + \eta^2 \theta_2'(0)). \tag{2.23}$$

2.4.1 Optimal homotopy analysis method

The series solution for the present boundary value problem is deliberated via optimal HAM. The mechanism is utilized to demonstrate solutions for non-linear equations. The entire interpretation can be found in [96, 97]. In the evaluation of the problem one needs the linear operators and initial guesses which are given below for the under discussion problem.

$$L_f(f) = \frac{d^3 f}{d\xi^3} + \frac{d^2 f}{d\xi^2}, \ L_{\theta_1}(\theta_1) = \frac{d^2\theta_1}{d\xi^2} - \theta_1, \ L_{\theta_2}(\theta_2) = \frac{d^2\theta_2}{d\xi^2} - \theta_2, \tag{2.24}$$

$$f_0(\xi) = 1 + (\xi - 1)R - (1 - R)exp(-\xi), \ \theta_{1_0}(\xi) = (1 - S_1)exp(-\xi),$$
$$\theta_{2_0}(\xi) = \xi exp(-\xi), \tag{2.25}$$

where $L_f(f)$, $L_{\theta_1}(\theta_1)$, and $L_{\theta_2}(\theta_2)$ specify the linear operators, additionally $f_0(\xi)$, $\theta_{1_0}(\xi)$ and $\theta_{2_0}(\xi)$ illustrates initial guesses of f, θ_1, and θ_2.

2.4.2 Convergence analysis

The auxiliary/supporting parameters in these analytic solutions are h_f, h_{θ_1}, and h_{θ_2} have remarkable intention in controlling the convergence of series solutions. To get a convergent analytic solutions, preferred values are assigns to h_f, h_{θ_1}, and h_{θ_2}. For this

reason, residual errors are observed for ferrohydrodynamic equations by implementing the expressions defined below

$$\Delta_m^f = \int_0^1 [R_m^f(\xi, h_f)]^2 d\xi, \tag{2.26}$$

$$\Delta_m^{\theta_1} = \int_0^1 [R_m^{\theta_1}(\xi, h_{\theta_1})]^2 d\xi, \tag{2.27}$$

$$\Delta_m^{\theta_2} = \int_0^1 [R_m^{\theta_2}(\xi, h_{\theta_2})]^2 d\xi. \tag{2.28}$$

These expressions are utilized in the evaluation of convergence for the optimal HAM, the resulting convergence and residual errors are listed in tables 2.1 and 2.2. Figures 2.2 and 2.3 reveal the average square residual error for 10th and 12th order. Δ_m^f exhibits the total square residual error, defined in the following equation

$$\Delta_m^t = \Delta_m^f + \Delta_m^{\theta_1} + \Delta_m^{\theta_2}. \tag{2.29}$$

$\begin{array}{c} values\rightarrow \\ order\downarrow \end{array}$	h_f	h_{θ_1}	h_{θ_2}	Δ_m^t
4	-0.85201	-0.32761	-0.83081	5.35012×10^{-7}
6	-0.90042	-0.79320	-0.93011	8.74023×10^{-12}
8	-0.99031	-0.95107	-1.18830	3.82109×10^{-16}
10	-1.03268	-0.98031	-1.89907	2.43981×10^{-19}
12	-1.38020	-0.99521	-1.39987	7.82033×10^{-22}

Table 2.1: Average residual square errors Δ_m^t.

$\begin{array}{c} values\rightarrow \\ order\downarrow \end{array}$	$h_f = -1.38020$	$h_{\theta_1} = -0.99521$	$h_{\theta_2} = -1.39987$
4	1.39811×10^{-7}	8.30932×10^{-8}	5.27890×10^{-9}
8	4.32098×10^{-15}	2.72209×10^{-14}	0.37890×10^{-13}
12	6.38041×10^{-20}	3.03318×10^{-17}	1.40992×10^{-19}
20	1.71109×10^{-25}	6.39804×10^{-23}	3.27088×10^{-21}

Table 2.2: Individual residual square errors for Δ_m^f, $\Delta_m^{\theta_1}$, and $\Delta_m^{\theta_2}$.
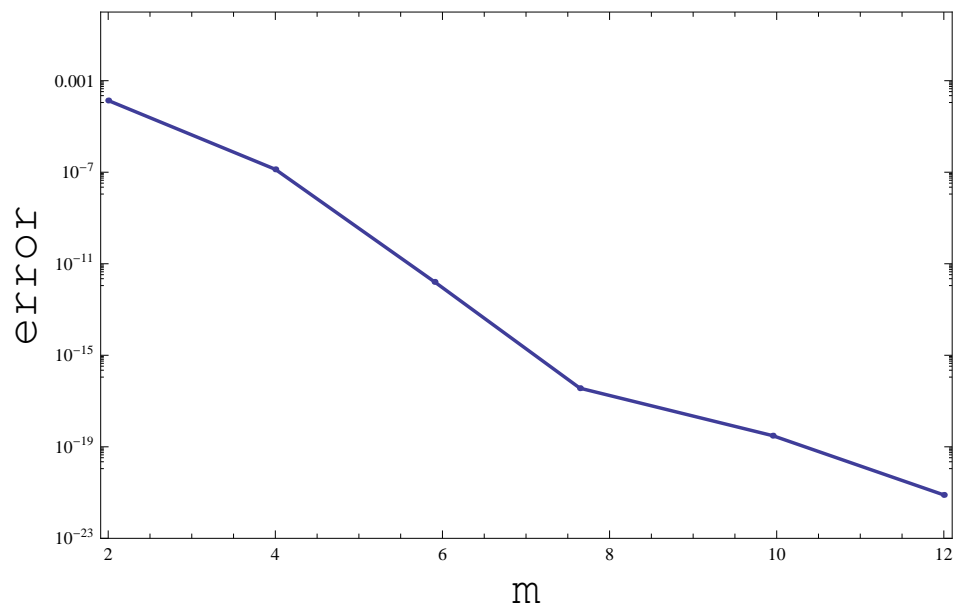
Figure 2.2: Graph for 10th order approximation.
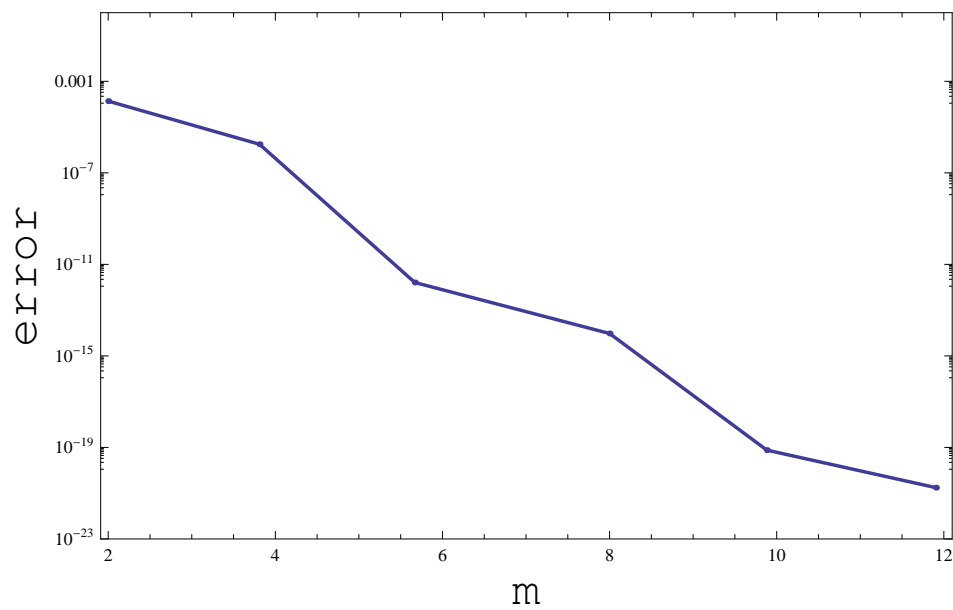
Figure 2.3: Graph for 12th order approximation.

2.5   Discussion

The consequences of present problem described in equations (2.16) to (2.20) is obtained through BVPh2−midpoint technique and optimal HAM. The characteristics of sundry substantial parameters on the flow are inspected. The impacts of dimensionless parameters β (ferrohydrodynamic interaction), λ (viscous dissipation), S_1 (thermal stratified), R (ratio), γ (dimensionless distance from origin to center of magnetic dipole), and Pr (Prandtl number) are scrutinized. Moreover, rest of the parameters appearing in the flow framework are treated fixed. Fixed values for these parameters are appropriated as $\varepsilon = 2.0, \lambda = 0.01, \gamma = 1.0$.

The influence of parameter β (ferrohydrodynamic interaction) is delineated in Figures 2.4 and 2.5. The presence of parameters β (ferrohydrodynamic interaction), ε (Curie temperature), and γ (dimensionless distance from magnetic dipole center to origin) are necessary to prevent the effect of magnetic dipole on the flow. The presence of (micro-sized) ferrite particles in a viscous carrier fluid leads to ferromagnetic fluid, which arises fluid viscosity and consequently a decrease in the velocity field occurs for increasing values of parameter β (ferrohydrodynamic interaction), as evident in Figure 2.4. The impact of β(ferrohydrodynamic interaction) on axial velocity is carried out when magnetic dipole is present. It is perceived that magnetic dipole reduces the axial velocity rapidly. The characteristics of parameter β (ferrohydrodynamic interaction) on temperature field are communicated in Figure 2.5. It is expressed that giving variation to parameter β (ferrohydrodynamic interaction) causes an enhancement in fluid temperature inside the boundary layer. In fact, the interaction between magnetic field action and fluid particles reduces velocity, thereby, arising heating due to friction among liquid layers that leads to thick thermal boundary layer, i.e., depletion in movements of liquid particles causes heat transfer strengthened, which is conspicuous in Figure 2.5.

The consequence of parameter S_1 (thermal stratification) on velocity and temperature fields are evident in Figures 2.6 and 2.7. Figures 2.6 and 2.7 stipulate that axial velocity and temperature field declines for the corresponding variation in thermal stratification parameter S_1. Increase in parameter S_1 (thermal stratified) leads to increase the density of fluid layers, due to which the dense particles of ferrite move toward the surface that gives rise to magnetohydrodynamic interaction, the respective interaction leads to enhance the viscosity of fluid and also effect the thermal conductivity, which is responsible for a reduction in axial velocity and heat transfer.

The characteristics of parameter R (ratio) on axial velocity are described in the current subsection. The parameter R depicts the ratio of ambient fluid velocity to

surface velocity due to stretchable sheet. The behavior for distinct values of parameter R (ratio) on axial velocity is scrutinized in Figure 2.8. The impacts of R is quite different for $R > 1$ and for $R < 1$. $R > 1$ physically states that the fluid have higher velocity, whereas, $R < 1$ demonstrates that surface with high velocity as compare to fluid velocity. Further, there is no change in axial velocity for $R = 1.0$, i.e., both surface and fluid move with same velocity. Improvement in axial velocity is noticed for enlarging values of ratio parameter R.
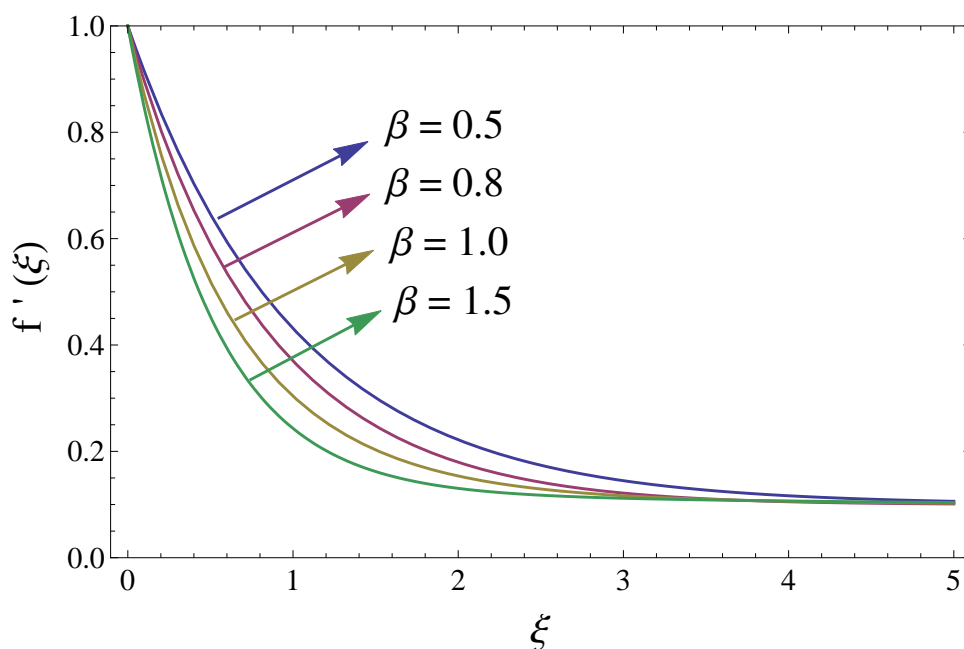
Figure 2.4: Consequence of parameter β (ferrohydrodynamic interaction) on axial velocity.
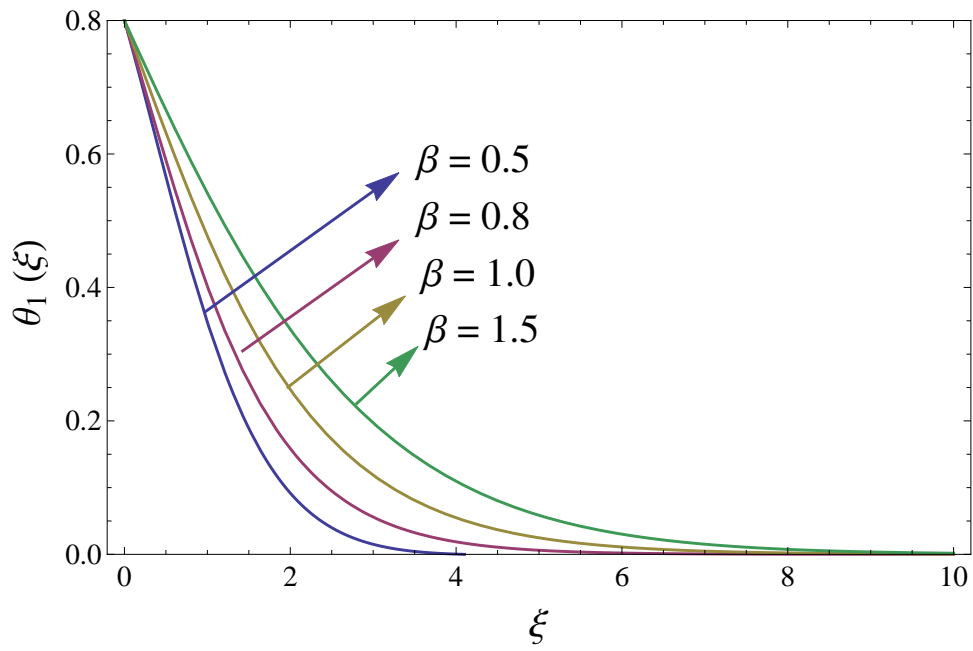
Figure 2.5: Consequence of β ferrohydrodynamic interaction parameter on distribution of temperature.
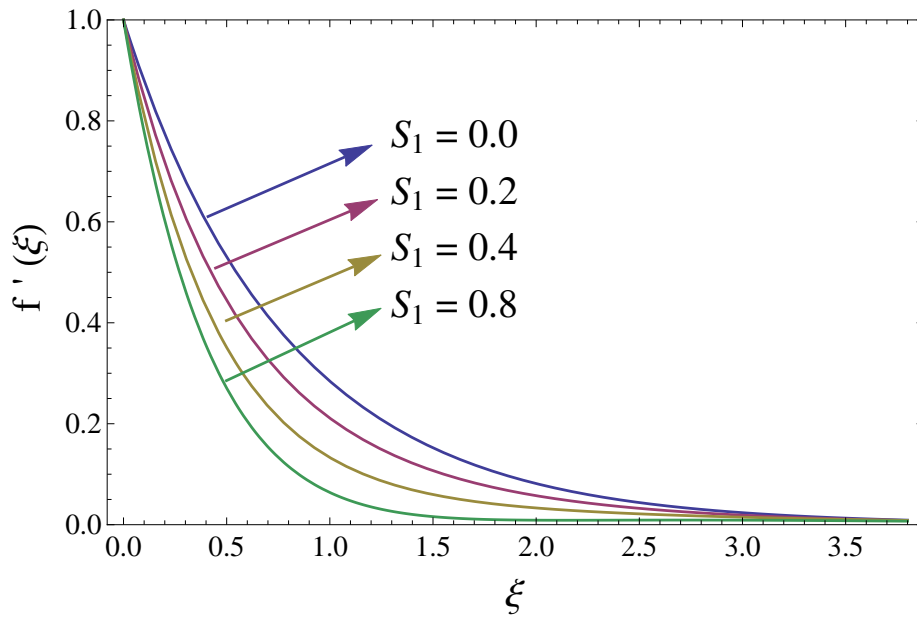
Figure 2.6: Consequence of S_1 thermal stratified parameter on axial velocity.
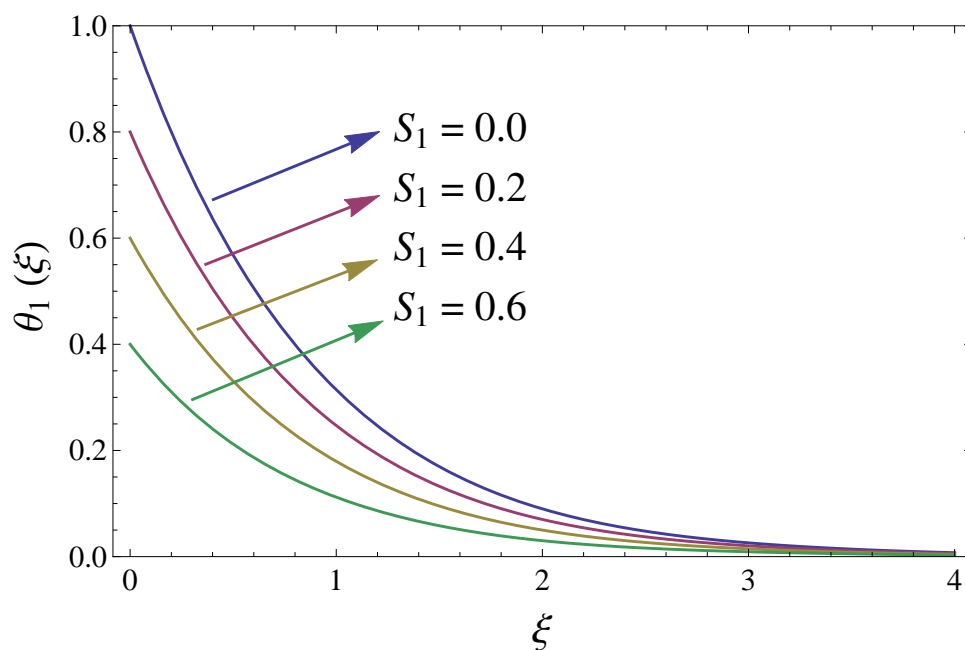
Figure 2.7: Impact of S_1 thermal stratified parameter on distribution of temperature.
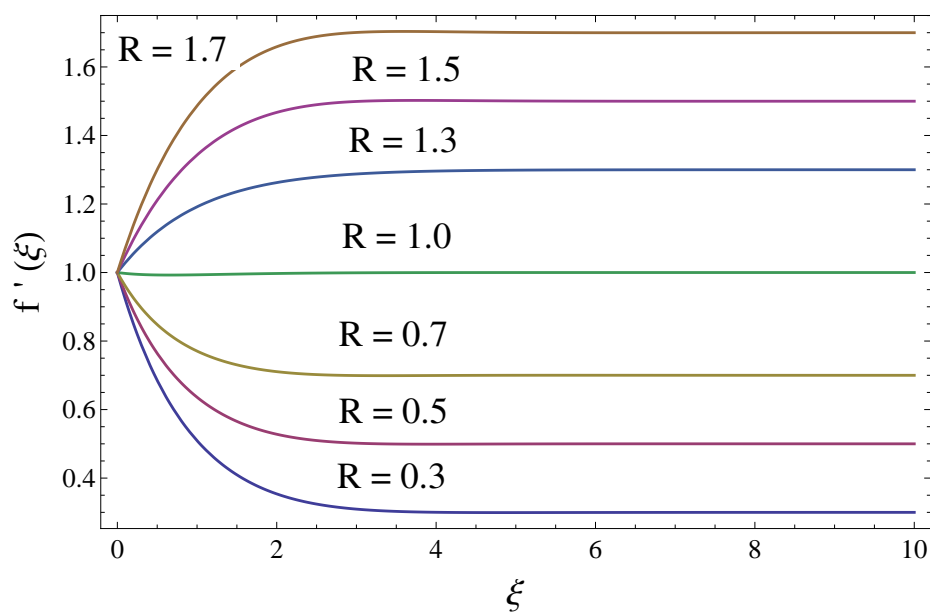
Figure 2.8: Consequence of R ratio parameter on velocity field.

2.5.1   Friction drag and local Nusselt number

Equations (2.22) and (2.23) incorporate mathematical form for friction drag and Nusselt number. The influence of parameter R on friction drag is characterized in Figure 2.9. The friction drag enlarges for increasing values of parameter R. Figure 2.9 designates that when $R = 0$ there is no change and it is because of the similarity between fluid velocity and sheet velocity due to stretching. Further, for prominent values of parameter R, the fluid axial velocity dominates the sheet velocity, which corresponds to enhancement in axial velocity, as a result, skin friction coefficient decreases. While Figure 2.10 exhibits the impact of parameter S_1 (thermal stratified) on wall shear stress. It is analyzed that larger stratification parameter gives rise to wall shear stress. Further, the characteristics of parameters Pr (Prandtl number) and S_1 (thermal stratification) via heat transfer rate are given in Figure 2.11 and 2.12 It is scrutinized from Figure 2.11 that variation in parameter Pr causes reduction in the heat transfer rate, instead from Figure 2.12, it is perceived that parameter S_1 reveals enhancement of rate of heat transfer. Table 2.4 shows the comparison of Nusselt number.
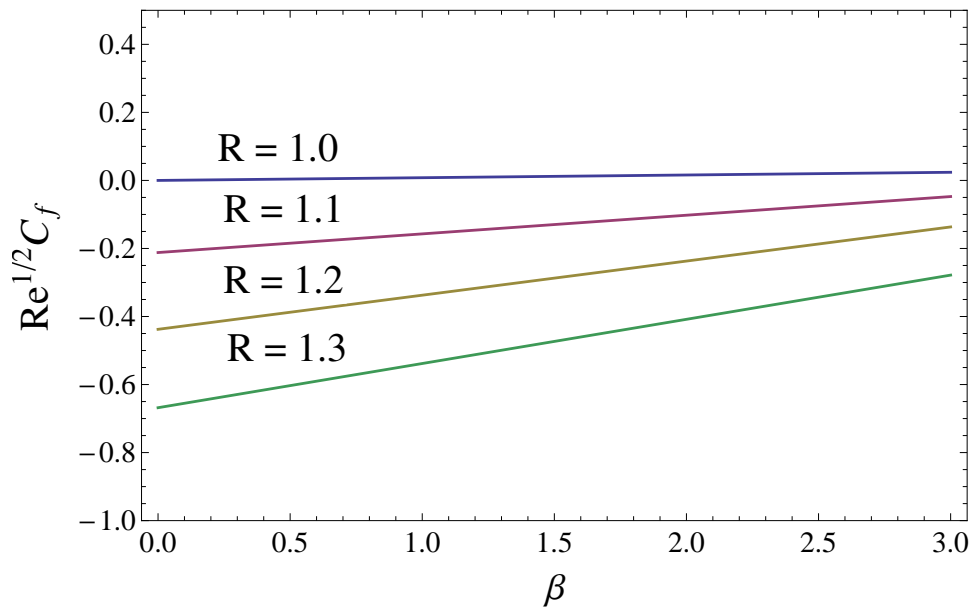
Figure 2.9: Wall shear stress versus ratio parameter R.
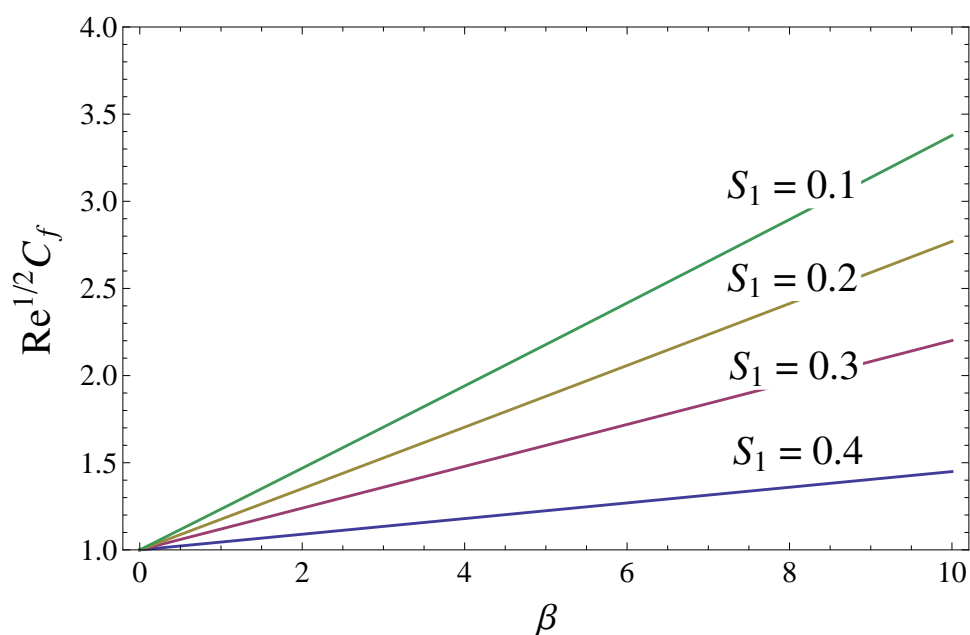
Figure 2.10: Wall shear stress versus thermally stratified parameter S_1.
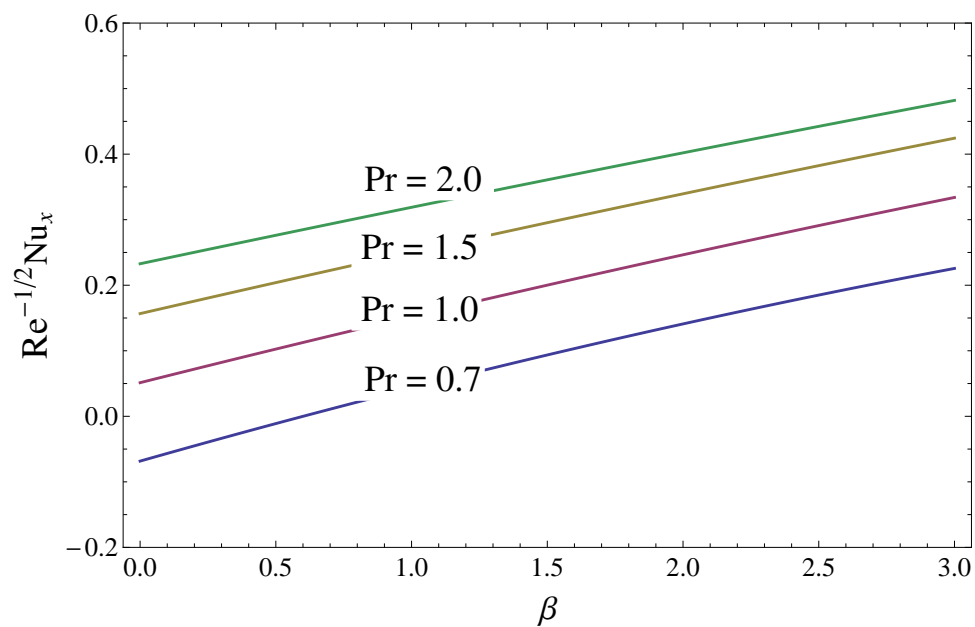
Figure 2.11: Heat transfer rate versus Prandtl number Pr.
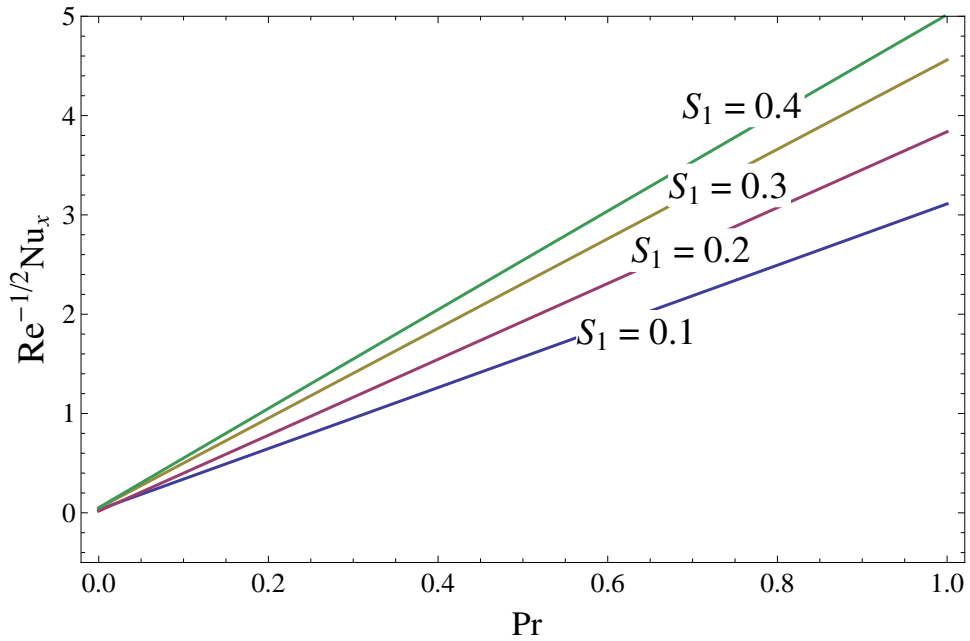
Figure 2.12: Heat transfer rate versus thermal stratified parameter S_1.

Pr	Chen [93]	$\mathrm{Re}^{-1/2}\,\mathrm{Nu}_x$ (Optimal HAM)	$\mathrm{Re}^{-1/2}\,\mathrm{Nu}_x$ (BVPh2-Midpoint)
0.72	1.0885	1.088461	1.0885521
1.0	1.3333	1.333250	1.3333720
2.0	2.0210	2.021910	2.0210619
3.0	2.5097	2.509692	2.5097472
4.0	$---$	2.903481	2.9030492
10.0	4.7968	$---$	4.7968310

Table 2.3: Comparison of Nusselt number.

Concluding remarks

The impacts of thermal stratification on the ferrofluid past a horizontally stretchable surface along an exterior magnetic dipole is evaluated. The main points to investigate the flow are given below.

- An increase in parameter (ferromagnetic interaction) gives rise to heat transfer thereby reducing axial velocity.

- Higher values of parameter S_1 (thermal stratification) correspond to thinning of velocity and temperature fields. Further, the heat transfer rate enhances for increasing values of thermal stratified parameter S_1.

- Variation in parameter R (ratio) results in an increment in axial velocity, while the wall shears stress decreases.

- Giving variation to Pr (Prandtl number) arises axial velocity thereby declines the temperature field.

Chapter 3

Evaluation of Fourier's law in a ferrofluid in porous medium

3.1   Introduction

This chapter delineates the impacts of stagnation point and thermal stratification on friction drag and heat transport phenomena in a Jeffrey fluid. The investigation is performed in presence of an exterior magnetic dipole. The analysis of Jeffrey fluid along magnetic dipole represents the ferromagnetic fluid. The fluid exhibits magnetic properties as a result of inclusion of ferrite particles, thus it is a non-Newtonian Jeffrey ferrofluid. The medium in the analysis is taken to be porous. Fourier's law is implemented in the assessment of heat flux. The respective equations are considered under the assumptions of a boundary layer. After utilizing the similarity variables the resulting equations are analyzed numerically and analytically with the help of BVPh2−midpoint method and Optimal HAM (homotopy analysis method) respectively. Physical features are interpreted via tables and graphs. Numerical values and graphical results of friction drag and heat transfer rate corresponding to involuted parameters have been discussed and computed. Further, the porosity parameter decline the axial velocity and Deborah number enhance the temperature field. Graphical results of several parameters on velocity of flow, friction drag, temperature field, and rate of heat transfer are presented.

3.2   Ferrohydrodynamic and thermal energy equations

An electrically nonconducting, steady, and an incompressible two-dimensional ferrofluid is merged past a stretched surface. The fluid under consideration is a non-Newtonian rate type fluid named as Jeffrey fluid. The stretching is initiated in the sheet having velocity $U_w(x)$ due to a force exerted on the sheet at $y = 0$. The stretching is directly relative to distance from origin. The magnetic dipole is arranged on outer surface at some distance from the fluid. While due to stagnation point flow the velocity as $y \to \infty$ is considered to be $U_e(x) = Qx$. A magnetic dipole is precisely put in the system in such a manner that its center lies at a distance d from below x−axis. An enhancement in magnetic field strength leads to saturate the ferrofluid. Curie temperature is greater than the stretching sheet temperature, whereas temperature of the fluid element away from the sheet is considered $T = T_\infty$ and $T_\infty < T_w < T_c$. The magnetic effect vanishes beyond the temperature T_c. Variable temperature $T_w = T_0 + b_1 x$ and $T_\infty = T_0 + b_2 x$ are scrutinized at wall and away from the wall, and T_0 signify the

reference temperature. The impact of heat absorption/generation is imperceptibly small. For ferrofluid, the governing equations are

$$\frac{\partial u}{\partial x} + \frac{\partial v}{\partial y} = 0, \tag{3.1}$$

$$u\frac{\partial u}{\partial x} + v\frac{\partial u}{\partial y} = -\frac{1}{\rho}\frac{\partial P}{\partial x} + \frac{\mu_0 M}{\rho}\frac{\partial H}{\partial x} + \frac{\mu}{\rho(1+\lambda_2)}\frac{\partial^2 u}{\partial y^2}$$
$$+ \frac{\mu\lambda_1}{\rho(1+\lambda_2)}\left(u\frac{\partial^3 u}{\partial x\partial y^2} + v\frac{\partial^3 u}{\partial y^3} + \frac{\partial u}{\partial y}\frac{\partial^2 u}{\partial x\partial y} - \frac{\partial u}{\partial x}\frac{\partial^2 u}{\partial y^2}\right) - \frac{\nu\epsilon}{k_2}u, \tag{3.2}$$

$$u\frac{\partial T}{\partial x} + v\frac{\partial T}{\partial y} - \frac{\mu_0 K_p T}{\rho c_p}\left(u\frac{\partial H}{\partial x} + v\frac{\partial H}{\partial y}\right) = \alpha\frac{\partial^2 T}{\partial y^2}. \tag{3.3}$$

Boundary conditions are

$$u|_{y=0} = U_w(x) = Sx, \; v|_{y=0} = 0, \; T|_{y=0} = T_w = T_0 + b_1 x, \tag{3.4}$$

$$u|_{y\to\infty} \to U_e(x) = Qx, \; T|_{y\to\infty} \to T_c = T_0 + b_2 x. \tag{3.5}$$

Here S and Q are dimensionless constants. The consequential schematic of ferrofluid is shown in Figure 3.1. Here the circular lines indicate the magnetic field.
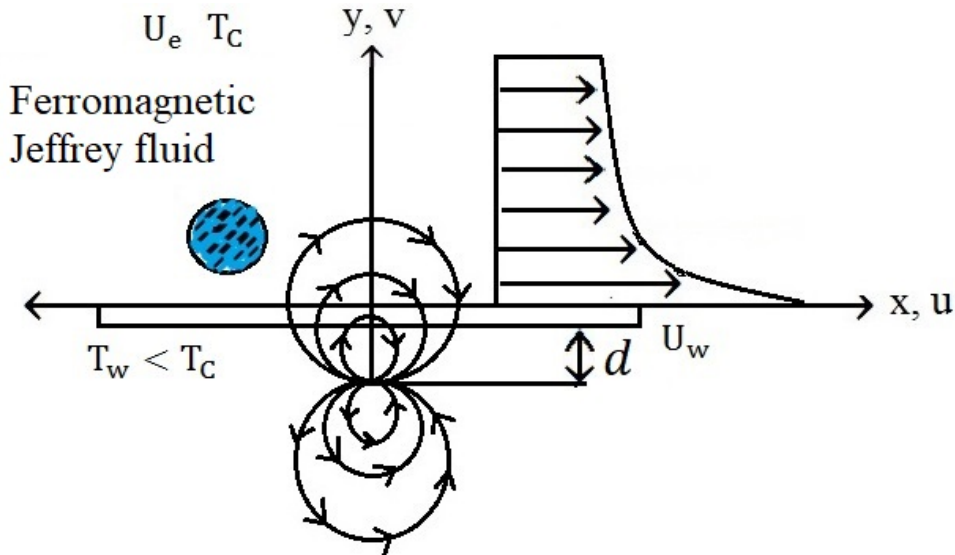
Figure 3.1: Geometery of the flow.

3.3   Solution procedure

Here we compose the dimensionless variables

$$\psi(\eta,\xi) = \eta(\frac{\mu}{\rho})f(\xi), \theta(\xi,\eta) \equiv \frac{T_c - T}{T_w - T_0} = \theta_1(\xi) + \eta^2\theta_2(\xi), \tag{3.6}$$

in which $\theta_1(\xi)$ and $\theta_2(\xi)$ exhibit dimensionless temperature, the corresponding non-dimensional coordinates are

$$\xi = y\sqrt{\frac{\rho S}{\mu}}, \quad \eta = x\sqrt{\frac{\rho S}{\mu}}. \tag{3.7}$$

The stream function is defined in this fashion that the mass equation satisfies directly, here the $\psi(\eta,\xi)$ signifies the stream function, (u,v) symbolizes the comparable components of velocity defined below

$$u = \frac{\partial\psi(\eta,\xi)}{\partial y} = Sxf'(\xi), v = -\frac{\partial\psi(\eta,\xi)}{\partial x} = -\sqrt{S\nu}f(\xi), \tag{3.8}$$

where prime expresses differentiation with respect to ξ and η. Employing the similarity transformations given in Eqs. (2.6)-2.12 and (3.6)-(3.8), Eqs. $(3.2 - 3.5)$ reduces to the system of boundary value problem

$$f''' - (\lambda_1 - 1)(f'^2 - ff'') - \beta_1(ff^{(iv)} - f''^2)$$
$$-(1 - \lambda_1)(\frac{2\beta\theta_1}{(\xi + \gamma)^4}) + P_m(R^2 - f') = 0, \tag{3.9}$$

$$\theta_1'' + Prf\theta_1' + \frac{2\lambda\beta\ f(\theta_1 - \varepsilon)}{(\xi + \gamma)^3} + 2\theta_2 - 4\lambda f'^2 = 0, \tag{3.10}$$

$$\theta_2'' - Pr(2f'\theta_2 - f\theta_2') + \frac{2\lambda\beta\ f\theta_2}{(\xi + \gamma)^3} - 4\lambda f''^2$$
$$+ \beta\lambda\ (\varepsilon - \theta_1)\left(\frac{2f'}{(\xi + \gamma)^4} + \frac{4f}{(\xi + \gamma)^5}\right) = 0, \tag{3.11}$$

$$f'(\xi) = 1, f(\xi) = 0, \theta_1(\xi) = 1 - S_1, \theta_2(\xi) = 0, \quad at\ \xi = 0, \tag{3.12}$$

$$f'(\xi) \to R, \theta_1(\xi) \to 0, \theta_2(\xi) \to 0, \quad when\ \xi \to \infty. \tag{3.13}$$

In above system of equations, the parameters β (ferrohydrodynamic interaction), β_1 (Deborah number), λ_1 signify relaxation to retardation times ratio, S_1 (thermal stratified parameter), λ (viscous dissipation), R (ratio), P_m (porosity parameter), ε (Curie temperature), and Pr (Prandtl number) are characterized as

$$R = \frac{Q}{S}, Pr = \frac{\nu}{\alpha}, \varepsilon = \frac{T_\infty}{T_w - T_0}, \beta = \frac{\gamma_1}{2\pi}\frac{\mu_0 K_p(T_w - T_0)\rho}{\mu^2}, \beta_1 = S\lambda_1,$$
$$\lambda = \frac{S\mu^2}{\rho K_p(T_w - T_0)}, P_m = \frac{\nu\epsilon}{K_2 S}, \gamma = \sqrt{\frac{S\rho d^2}{\mu}}, S_1 = \frac{b_2}{b_1}. \tag{3.14}$$

At the walls, the parameters of engineering interest, i.e., the friction drag and rate of heat transfer are

$$C_f = \frac{2\tau_w}{\rho U_w^2}, \ \tau_w = \frac{\mu}{1+\lambda_1}\frac{\partial u}{\partial y}\bigg|_{y=0} + \frac{\mu\lambda_2}{1+\lambda_1}\left(u\frac{\partial^2 u}{\partial y\partial x} + v\frac{\partial^2 u}{\partial y^2}\right)\bigg|_{y=0},$$

$$Nu_x = \frac{x}{T_w - T_0}\frac{\partial T}{\partial y}\bigg|_{y=0}.$$

(3.15)

Which after non-dimensionalization take the form

$$\frac{1}{2}Re^{1/2}C_f = \frac{1}{1+\lambda_1}(f''(0) - \beta_1(f(0)f'''(0) - f''(0)f'(0))),$$

$$Re^{-1/2}Nu_x = -(\theta_1'(0) + \eta^2\theta_2'(0)).$$

(3.16)

3.3.1 Optimal homotopy analysis method

Optimal HAM (homotopy analysis method) is employed for solution of present boundary value problem. The method is hired to demonstrate solutions for non-linear equations. The optimal HAM gives us a better flexibility to get the auxiliary linear operator and the initial guess than the conventional non-perturbable techniques. The entire interpretation can be found in [96, 97]. The linear operators and initial guesses in the present analysis is defined below

$$L_f(f) = \frac{d^3f}{d\xi^3} + \frac{d^2f}{d\xi^2}, \ \ L_{\theta_1}(\theta_1) = \frac{d^2\theta_1}{d\xi^2} - \theta_1,$$

$$L_{\theta_2}(\theta_2) = \frac{d^2\theta_2}{d\xi^2} - \theta_2.$$

(3.17)

$$f_0(\xi) = 1 - (1-\xi)R - (1-R)exp(-\xi), \ \ \theta_{1_0}(\xi) = (1-S_1)exp(-\xi),$$

$$\theta_{2_0}(\xi) = \xi exp(-\xi),$$

(3.18)

where $L_f(f)$, $L_{\theta_1}(\theta_1)$, and $L_{\theta_2}(\theta_2)$ portray the linear operators, besides $f_0(\xi)$, $\theta_{1_0}(\xi)$ and $\theta_{2_0}(\xi)$ exemplify initial guesses of f, θ_1, and θ_2.

3.3.2 Convergence analysis

The auxiliary parameters h_f, h_{θ_1}, and h_{θ_2} have a magnificent aim to stabilize the convergence of solutions. To get a convergent analytic solutions, preferred values are assigns to h_f, h_{θ_1}, and h_{θ_2}. For this reason, residual errors are observed for ferrohydrodynamic equations by implementing the expressions defined in Eqs. (2.26)-(2.28). These expressions are utilized in the evaluation of convergence for the optimal

HAM, the resulting convergence and residual errors are listed in tables 3.1 and 3.2. Figures 3.2 and 3.3 reveals the 10th and 12th order average residual square error. Δ_m^f exhibits the total square residual error, defined in Eq. (2.29).

$\frac{values\rightarrow}{order\downarrow}$	h_f	h_{θ_1}	h_{θ_2}	Δ_m^t
4	-0.981921	-0.872958	-0.09223	4.61754×10^{-8}
6	-0.01206	-0.943273	-0.02714	1.59062×10^{-11}
8	-0.05365	-0.914006	-0.06445	6.70151×10^{-15}
10	-0.04371	-0.05362	-0.01794	1.01087×10^{-18}
12	-0.03177	-0.92185	-0.06242	4.11943×10^{-22}

Table 3.1: Average residual square errors Δ_m^t.

$\frac{values\rightarrow}{order\downarrow}$	$h_f = -0.03177$	$h_{\theta_1} = -0.92185$	$h_{\theta_2} = -0.06242$
4	1.10421×10^{-9}	3.42476×10^{-7}	3.63257×10^{-6}
8	3.54190×10^{-17}	2.51890×10^{-12}	4.44569×10^{-10}
12	8.43786×10^{-20}	7.42327×10^{-16}	5.65326×10^{-14}
20	2.56190×10^{-23}	0.53438×10^{-21}	7.96546×10^{-20}

Table 3.2: Individual residual square errors for Δ_m^f, $\Delta_m^{\theta_1}$, and $\Delta_m^{\theta_2}$.
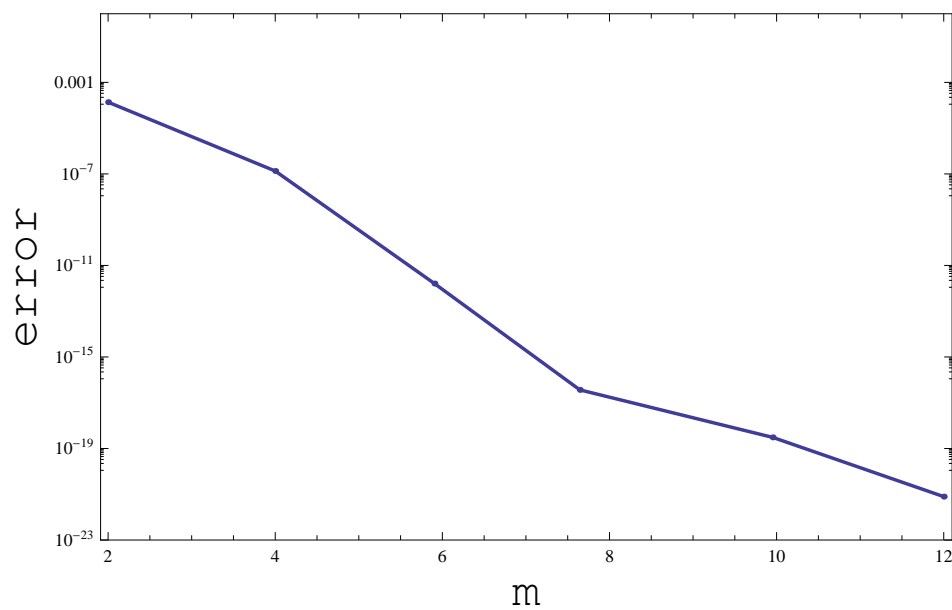
Figure 3.2: Error decay for 10th order approximation.
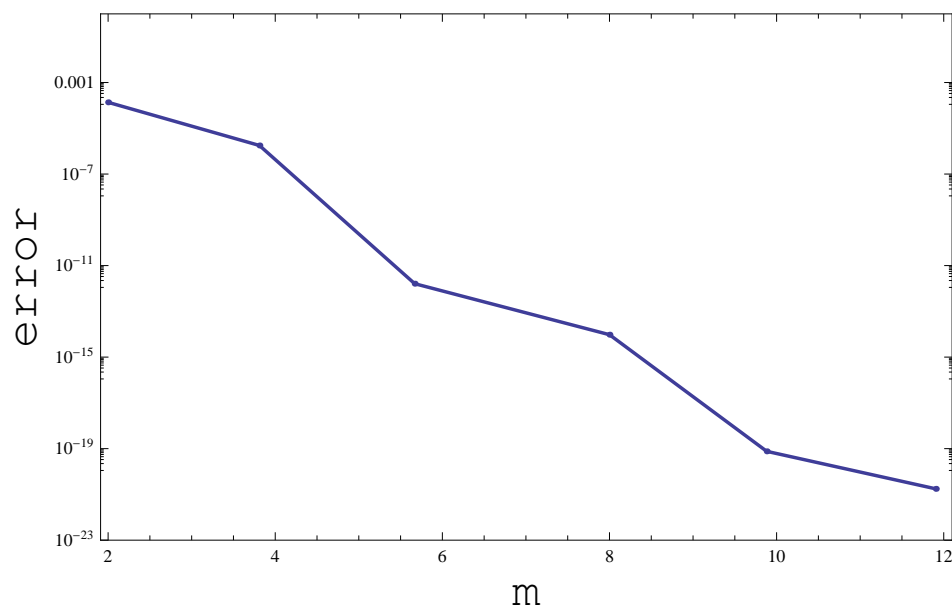
Figure 3.3: Error decay for 12th order approximation.

3.4   Discussion

Optimal HAM is implemented to get the results of the boundary value problem described in Eqs. (3.9)-(3.13). Here the influence of sundry substantial parameters on fluid flow are under discussion. The impacts of dimensionless parameters β_1 (Deborah number), λ_1, β (ferrohydrodynamic interaction), λ (viscous dissipation), S_1 (thermal stratified), R (ratio), γ (dimensionless distance from origin to center of magnetic dipole), and Pr (Prandtl number) are scrutinized. Moreover, other parameters in the flow framework are fixed. The fixed values are $\lambda = 0.1$, $\gamma = 1.0$, and $\varepsilon = 2.0$.

The impact of ferromagnetic effect on flow problem exists only in presence of β (ferrohydrodynamic interaction), ε (Curie temperature) and γ (dimensionless distance from origin to center of magnetic dipole) parameters. In Figure 3.4, velocity field reduces by the increment in β (ferrohydrodynamic interaction) parameter because of the presence of ferrite particles arises liquid viscosity. The characteristics of parameter β (ferrohydrodynamic interaction) on distribution of temperature are shown in Figure 3.5. It is observed that by varying the parameter β (ferrohydrodynamic interaction), inside the boundary layer temperature enhances. This occurs by the interaction between movements of liquid particles and an action of a magnetic field. The interaction between particles of fluid and magnetic field action diminishes the velocity of the fluid, whereas, frictional heating among fluid layers is growing which leads to arise thermal boundary layer, i.e., enhancement in heat transfer occurs because of the reduction in movements of fluid particles, which is evident in Figure 3.5.

The impacts of parameters β_1 (Deborah number) and λ_1 (ratio of relaxation to retardation times) on temperature field and axial velocity are evident in Figures 3.6−3.9. When $\lambda_1 = 0$ and $\lambda_2 = 0$, the relaxation and retardation time at surface reach its minimum value, which stipulates that the interior impacts of relaxation and retardation time in liquid are absent, because of which fluid becomes a classical Newtonian fluid. The impact of β_1 (Deborah number) on axial velocity and distribution of temperature is delineated in Figure 3.6 and 3.7. Rising Deborah number β_1 leads to enlarge the stretching rate at the surface, as a result, disturbance in particles of ferrofluid nearer the surface arises, such disturbance in particles of ferrofluid enhances the inertial forces, which enhances the axial velocity as is evident in Figure 3.6. Characteristics of β_1 (Deborah number) on the diffusion of temperature is revealed in Figure 3.7. Arising β_1 (Deborah number), temperature field is evaluated to be declines. Physically β_1 (Deborah number) is corresponding to λ_1, thus, any substance reduces its viscosity for long retardation time, which may bring about an enhancement in its movement, which subsequently debilitates lower temperature field. Further, Figures 3.8 and 3.9

depict the performance of the ratio of relaxation to retardation times parameter λ_1 on velocity and temperature fields. From Figure 3.8, it is watched that axial velocity declines for arising λ_1 (ratio of relaxation to retardation time), contrarily, temperature profile is slowly expanding with enlarging λ_1 (ratio of relaxation to retardation time) as shown in Figure 3.9. An enhancement in λ_1 infers to an enhancement in relaxation time, i.e., a perturbed system requires more time in retaining its original position. This phenomenon of relaxation times leads to arising the drag forces, which are responsible for the possible reduction in axial velocity and enhancement in temperature field.

The present study characterizes the consequence of parameter S_1 (thermal stratification) on velocity and temperature fields. Velocity and temperature fields are decreasing for greater values of the corresponding parameter thermal stratification shown in Figures 3.10 and 3.11. It is noted that the decaying temperature difference between surface and ambient of sheet is reducing the temperature field. Magnetohydrodynamic interaction parameter β is responsible for a reduction in axial velocity and heat transfer is raised by increasing parameter S_1 (thermal stratified), leads to increasing the density of fluid. As magnetohydrodynamic interaction is raised by the high density of ferrite particles moving towards the surface.

The Prandtl number Pr play a vital role in forced convective heat transfer and thermal boundary layer. The Pr (Prandtl number) measure the ratio of heat transmission and energy storage capacities of the molecules. Figure 3.12 exhibits the impact of Pr (Prandtl number) on distribution of temperature. It is designated that due to increasing Pr (Prandtl number), thermal diffusivity declines, subsequently, the thermal boundary layer thickness and temperature declines, the resultant disturbance due Prandtl number is determined in Figure 3.12.

The stretchable sheet causes change in velocity of the fluid, we thus established the ratio parameter R which designates the ratio of ambient fluid velocity to surface velocity. The parameter R has a peculiar behavior on axial velocity observed in Figure 3.13. The parameter R has contrasting behavior for $R > 1.0$ and for $R < 1.0$. Moreover, axial velocity remains constant for $R = 1.0$, means both the surface and fluid flows with same velocity. Axial velocity is rising by the increment in ratio parameter R. Whereas, the consequence of parameter P_m (porosity) on the axial velocity is demonstrated in Figure 3.14. Velocity field declines by giving variation to parameter P_m (porosity).
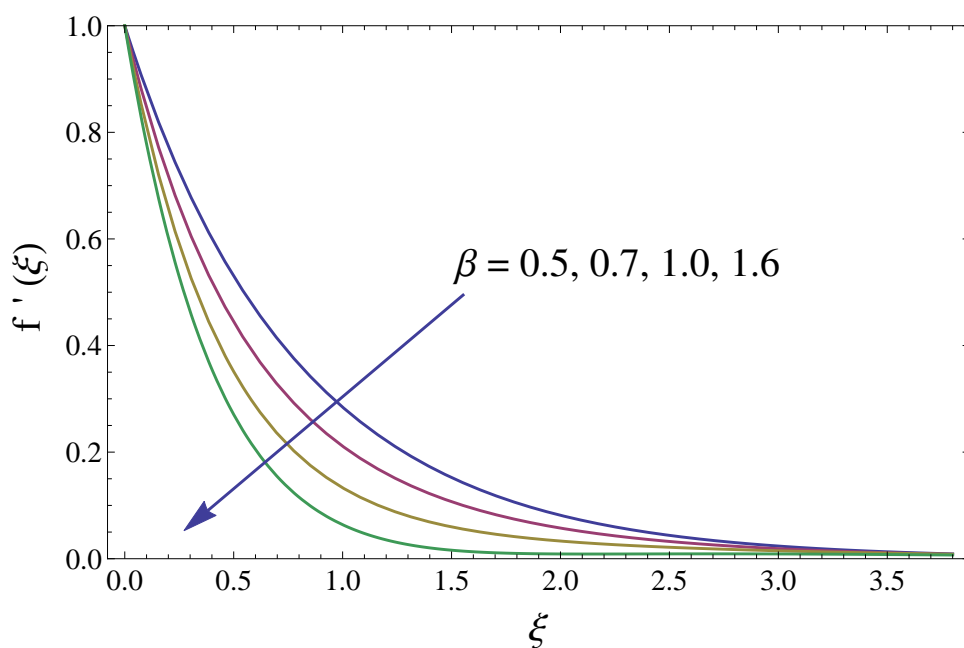
Figure 3.4: Impact of paramter β (ferrohydrodynamic interaction) on axial velocity $f'(\xi)$.
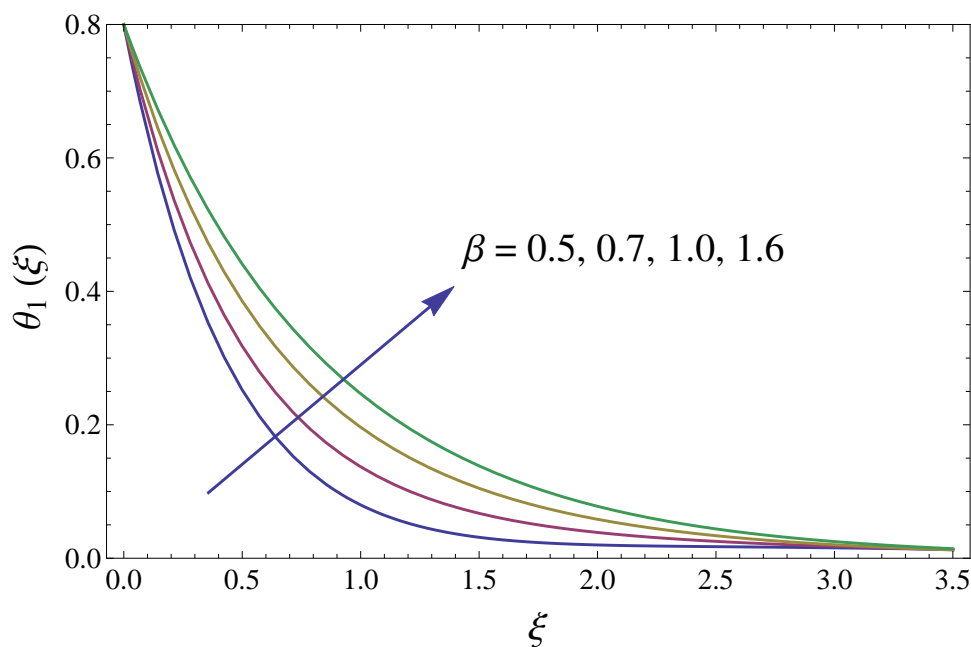
Figure 3.5: Impact of parameter β (ferrohydrodynamic interaction) on temperature field $\theta_1(\xi)$.
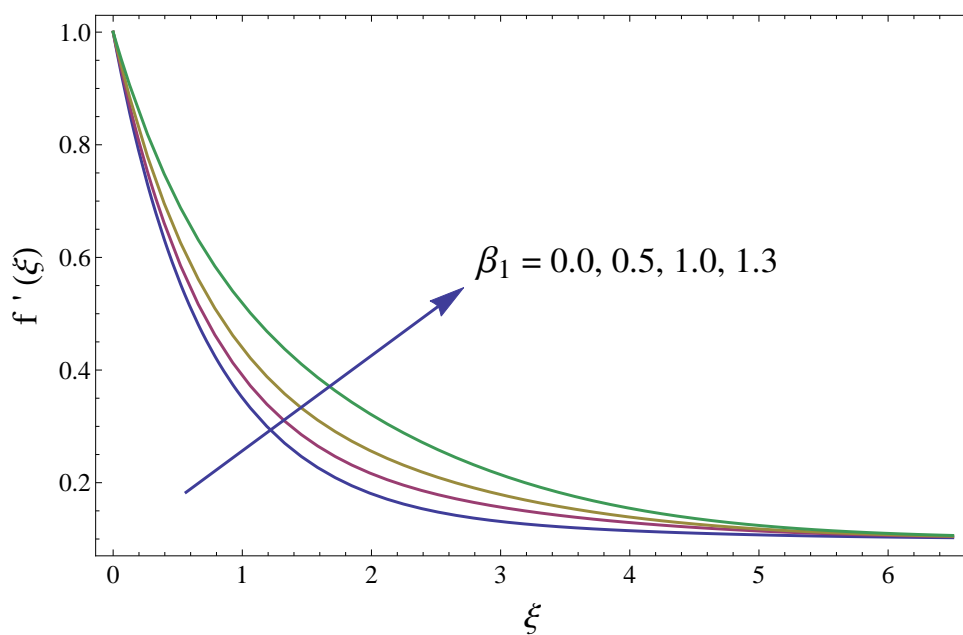
Figure 3.6: Influence of β_1 (Deborah number) on distribution of velocity $f'(\xi)$.
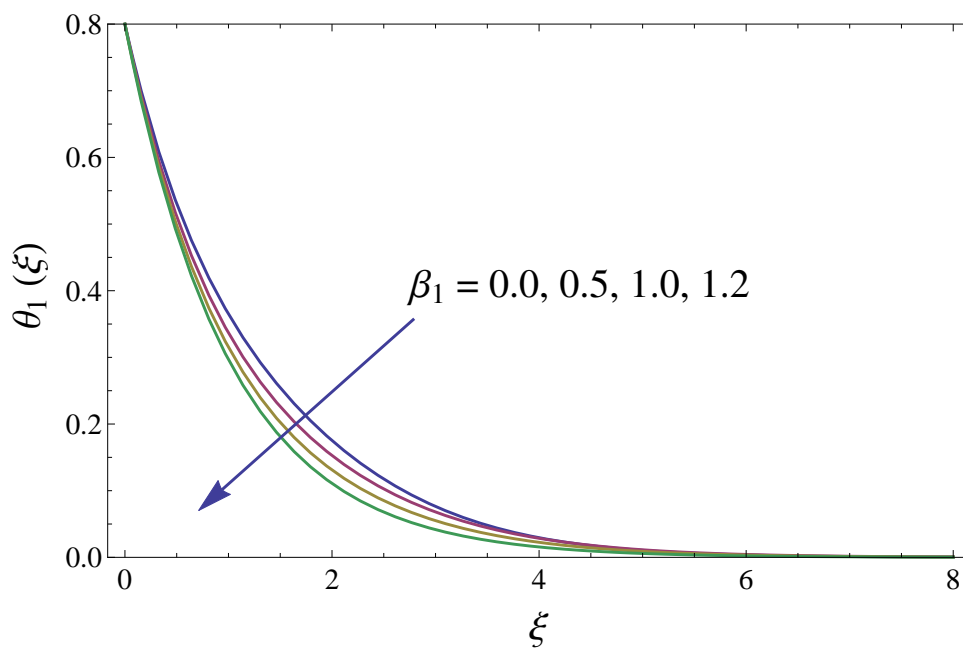
Figure 3.7: Effect of β_1 (Deborah number) on temperature distribution $\theta_1(\xi)$.
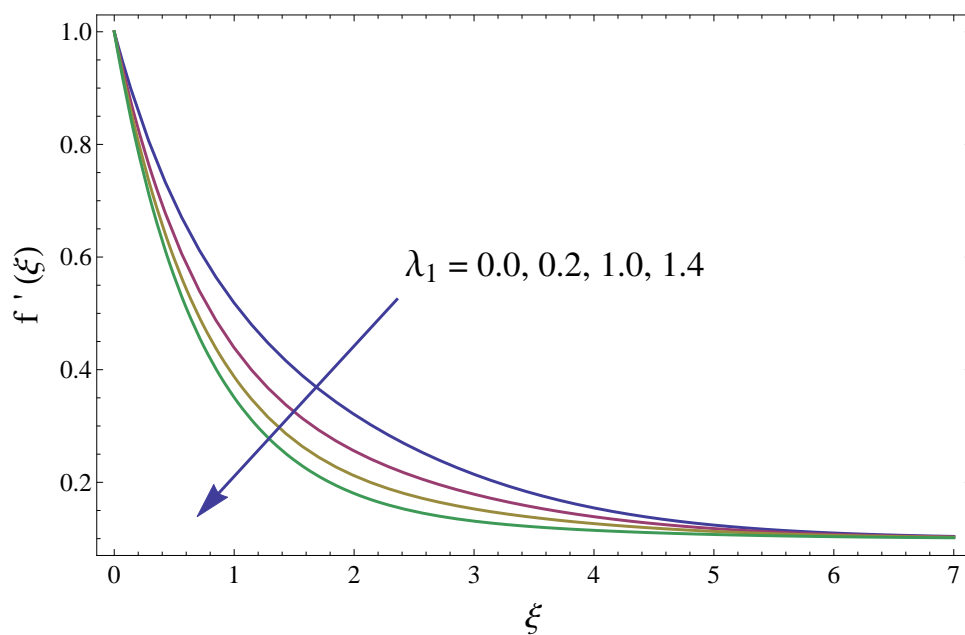
Figure 3.8: Impact of parameter λ_1 (ratio of relaxation to retardation times) on velocity field $f'(\xi)$.
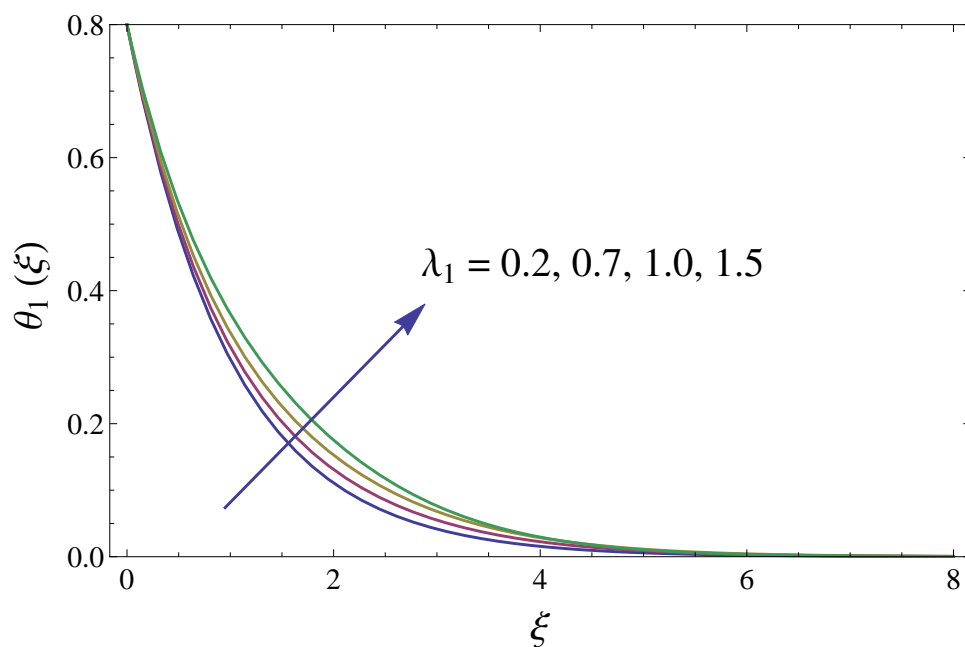
Figure 3.9: Consequence of parameter λ_1 on distribution of temperature $\theta_1(\xi)$.
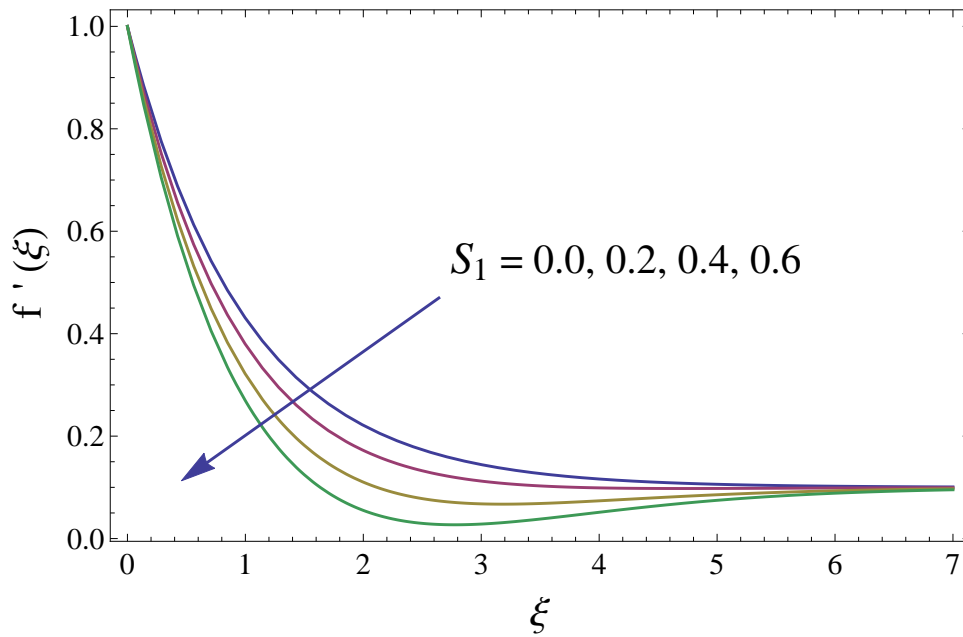
Figure 3.10: Consequence of S_1 (thermal stratified parameter) on axial velocity $f'(\xi)$.
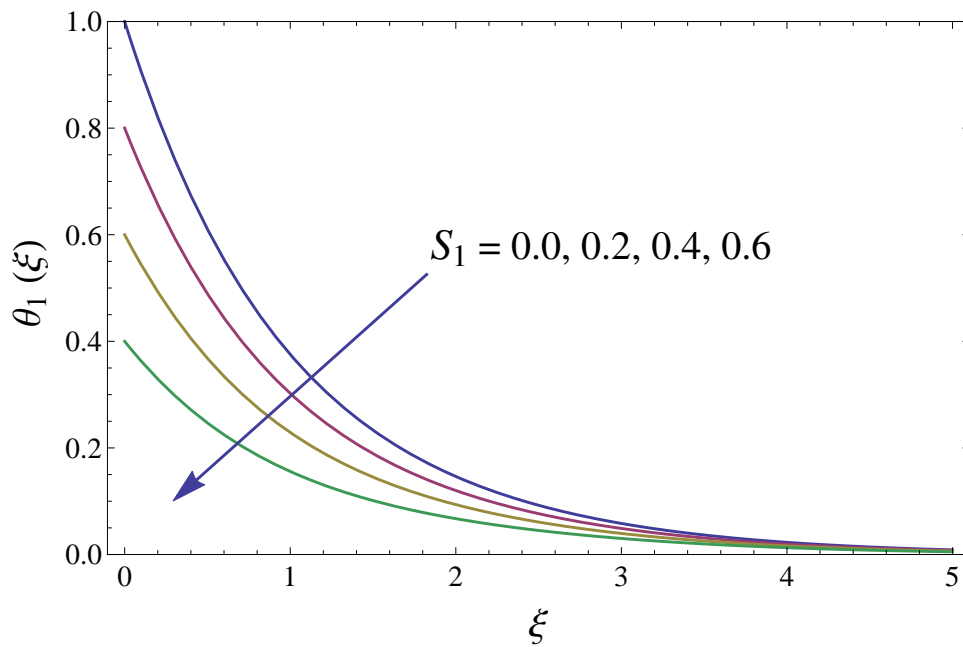
Figure 3.11: Influence of S_1 (thermal stratified paramter) on temperature field $\theta_1(\xi)$.
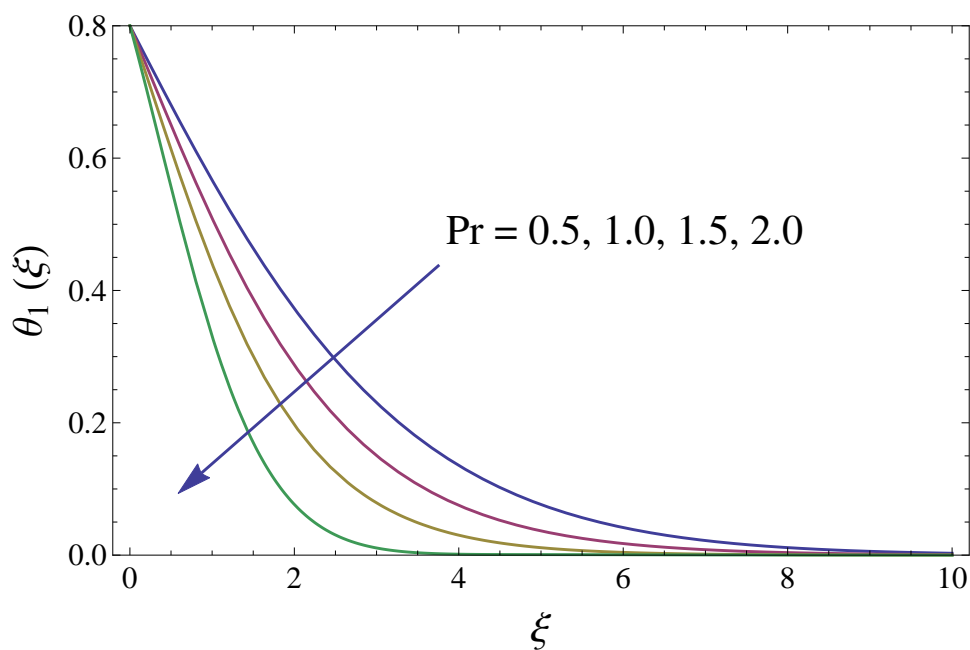
Figure 3.12: Effect of Pr (Prandtl number) on temperature field $\theta_1(\xi)$.
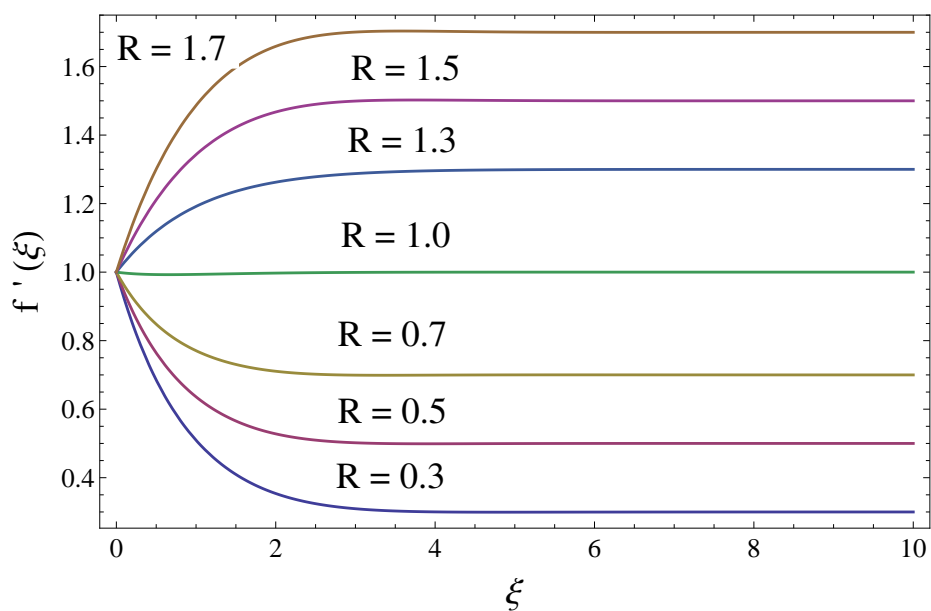
Figure 3.13: Consequence of R (ratio parameter) on velocity distribution $f'(\xi)$.
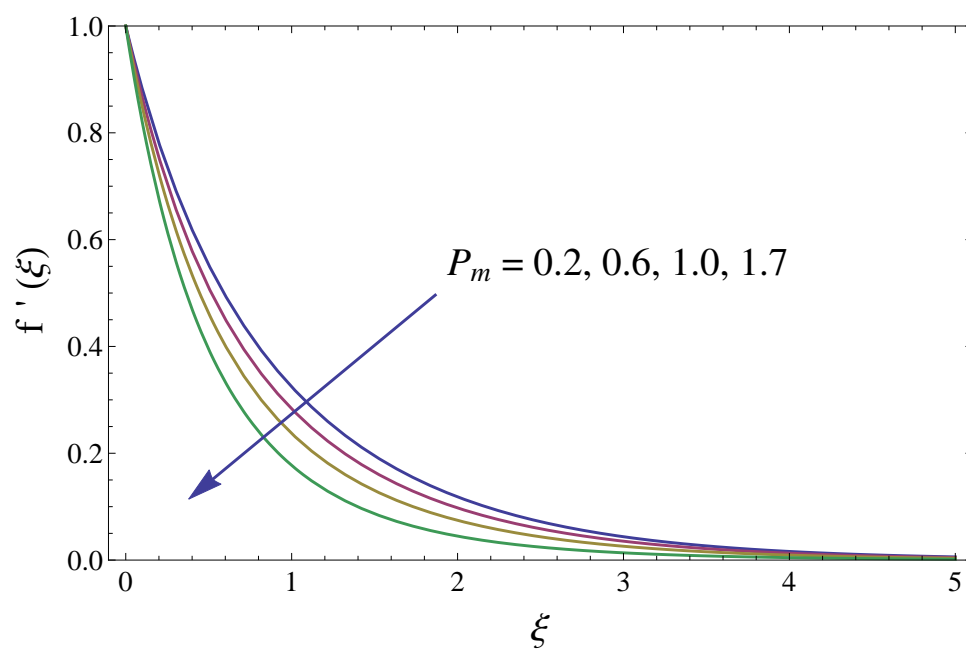
Figure 3.14: Effect of P_m (porosity paramter) on $f'(\xi)$.

3.4.1 Friction drag and local Nusselt number

Impact of sundry substantial parameters β (ferrohydrodynamic interaction), β_1 (Deborah number), λ_1 (relaxation to retardation times ratio), R (ratio parameter), S_1 (thermal stratified paramteter), and Pr (Prandtl number) are observed on friction drag and Nusselt number. The characteristics of β_1 (Deborah number) and β (ferrohydrodynamic interaction) on the friction drag are evident in Figure 3.15. The friction drag declines for giving variation to β_1 (Deborah number) along with β (ferrohydrodynamic interaction). The impacts of λ_1 (ratio of relaxation to retardation times) and R (ratio parameter) on the friction drag is characterized in Figure 3.16. The enhancement in parameter R causes an increase in friction drag. Moreover, skin friction coefficient declines because plate velocity is hindered by fluid velocity for greater values of parameter R causing an increase in axial velocity. The fluid velocity and sheet velocity are same due to stretching at $R = 0$, causing no change in the graph Figure 3.16. Moreover, impact of S_1 (thermal stratified parameter), β_1 (Deborah number), and Pr (Prandtl number) on the heat transfer at the surface is evaluated in Figure 3.17 and 3.18. Heat transfer at the surface declines when Prandtl number Pr is enhanced along β_1 (Deborah number) as depicted in Figure 3.17. While Figure 3.18 designates the impact of parameter S_1 (thermal stratified) on transfer of heat at the surface. the features of parameters Pr (Prandtl number) and S_1 (thermal stratification) via heat transfer rate are given in Figure 3.18. It is perceived that enhancement in parameter S_1 leads to enhance the heat transfer rate. Tables 3.3 and 3.4 display the comparison of Nusselt number and friction drag.

Pr	Abel et al. [95]	OHAM results $-\theta_1'(0)$	BVPh2-Midpoint $-\theta_1'(0)$
0.72	1.0885	1.088542	1.0882302
1.0	1.3333	1.333341	1.3332183
2.0	$---$	2.021082	2.0215192
3.0	$---$	2.509783	2.5097533
4.0	$---$	2.903042	2.9034172
10.0	4.7968	$---$	4.7868615

Table 3.3: Comparison of rate of heat transfer for the case when $\beta = 1.0$, $\beta_1 = 1.0$, $Pm = 1.0$, $\lambda_1 = 1.5$, $S_1 = 0.2$.

Pr	β	β_1	S_1	$\frac{1}{2}Re^{1/2}C_f$	$Re^{-1/2}Nu$
1.0	1.0	0.7	0.2	1.08721	1.28703
1.5				1.06532	2.08518
2.5				1.00532	2.34319
2.0	1.0	0.7	0.2	1.29365	2.44380
	1.4			1.45329	2.31437
	1.8			1.55430	2.31981
2.0	1.0	0.4	0.2	1.54828	0.95285
		0.8		1.32063	0.97275
		1.2		1.15042	0.98421
2.0	1.0	0.2	0.2	1.15476	0.79654
			0.4	1.16543	0.87542
			0.6	1.18043	0.96432

Table 3.4: Friction drag and local Nusselt number.
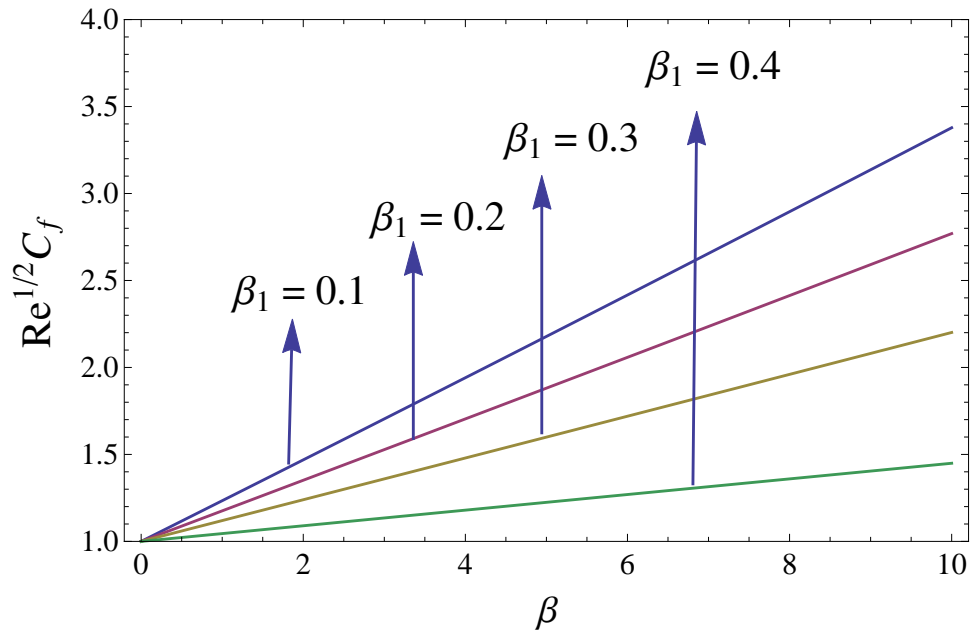
Figure 3.15: Wall shear stress versus β_1 Deborah number.
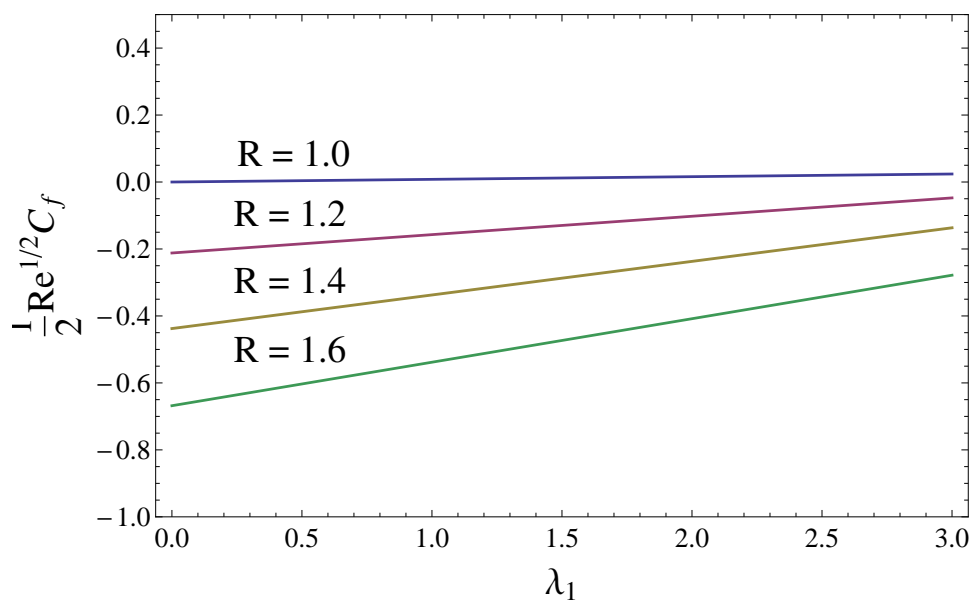
Figure 3.16: Wall shear stress versus ratio parameter R.
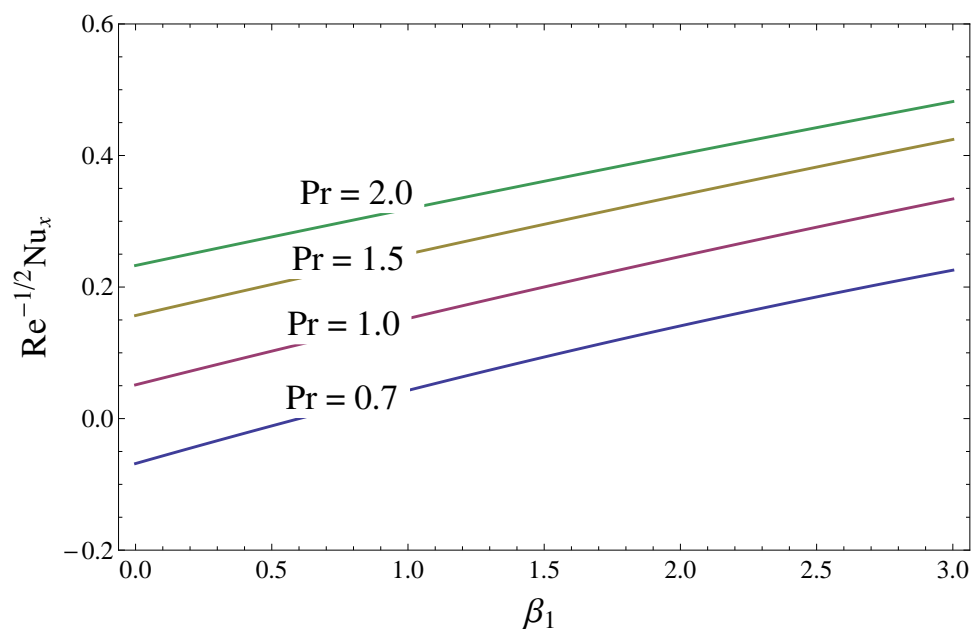
Figure 3.17: Heat transfer rate versus Prandtl number Pr.
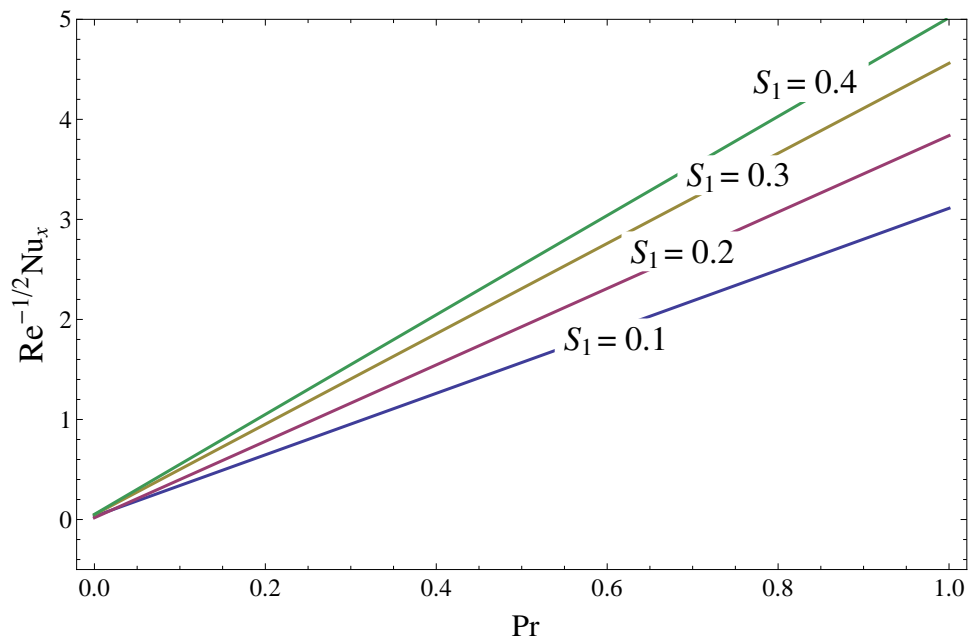
Figure 3.18: Heat transfer rate versus S_1 thermal stratified parameter.

Concluding remarks

The aspects of thermal stratification on the ferrofluid past a horizontally stretchable surface under the influence of magnetic dipole is under discussion. Bvph2-midpoint method and Optimal HAM are used to get the numerical and analytic series solution for flow problem. The consequences of a few physical parameters, for example, parameter β ferromagnetic interaction, λ_1, thermally stratified parameter S_1, Deborah number β_1, ratio parameter R, Prandtl number Pr and porosity parameter P_m on temperature and velocity fields are inspected and scrutinized graphically in point of interest. At last, Some critical perceptions in view of the present study are as per the following.

- An increase in parameter β (ferromagnetic interaction) gives rise to heat transfer thereby reducing axial velocity.

- Variation in β_1 (Deborah number) declines temperature field and enhances axial velocity.

- Axial velocity declines as we enhance the porosity parameter P_m.

- Variation in parameter R (ratio) arises axial velocity, while the wall shears stress decreases.

- λ_1 declines the axial velocity whereas increases the temperature field.

- Higher values of parameter S_1 (thermal stratification) corresponds to thinning of velocity and temperature fields. Further, the rate of heat transfer enhances for increasing values of parameter S_1.

- Pr (Prandtl number) leads to decline the temperature field.

Chapter 4

Analysis of friction drag and heat transfer in a ferrofluid

4.1 Introduction

This chapter characterized the heat transport phenomena in a second grade ferrofluid flow. The analysis is carried out in the presence of an external magnetic dipole. The investigation is disclosed by the phenomenon of stagnation point. Variable temperature at boundary and away from the surface is incorporated in the analysis. The assumptions of Newtonian heating and thermal radiation are neglected. Conservation of linear momentum and mass is utilized to model expressions for a second grade ferrohydrodynamic problem. Heat flux is evaluated by employing the Fourier's law. Optimal HAM (Homotopy Analysis Method) is demonstrated in the evaluation of influence of magneto-thermomechanical coupling and normal stress on the ferrohydrodynamic flow. The impacts of distinct parameters on temperature field and axial velocity are depicted through graphs. Numerical values and graphical results of friction drag and heat transfer rate corresponding to involuted parameters have been discussed and computed. Further, the (elasticity parameter declines the temperature field thereby enhances the axial velocity. Graphical results of several parameters on rate of heat transfer, axial velocity, friction drag, temperature field are presented.

4.2 Ferrohydrodynamic and thermal energy equations

The impacts of a steady, electrically non-conducting and an incompressible two-dimensional second grade ferrofluid over an impermeable linear stretching sheet are incorporated. By exerting a force on the sheet located at $y = 0$ introduces stretching in the sheet having velocity $U_w(x)$. The resulting stretching in the sheet is proportional to the length from origin. The velocity of stagnation point far away from wall is taken to be $U_e(x) = Qx$. Further, magnetic dipole is placed at a distance outside from the surface. The center of magnetic dipole is placed on vertical axis at a distance d below the $x-$axis. The magnetic field points of magnetic dipole are taken along positive $x-$axis. An enhancement in the strength of magnetic field driven by magnetic dipole leads to saturate the ferrofluid. The temperature $T = T_\infty$ is assumed to be fluid temperature away from the surface, where $T_\infty < T_w < T_c$, the fluid above T_c is incapable of being magnetized. $T_w = T_0 + b_1 x$ and $T_\infty = T_0 + b_2 x$ are respectively involved as the variable temperature at the surface and away from surface. The impacts of heat absorption/generation are taken to be negligibly small. Making use of boundary

layer approximations, the governing equations in a ferrofluid under boundary layer approach are

$$\frac{\partial u}{\partial x} + \frac{\partial v}{\partial y} = 0, \tag{4.1}$$

$$u\frac{\partial u}{\partial x} + v\frac{\partial u}{\partial y} = -\frac{1}{\rho}\frac{\partial P}{\partial x} + \frac{\mu_0 M}{\rho}\frac{\partial H}{\partial x} + \nu\frac{\partial^2 u}{\partial y^2}$$
$$+ \frac{\alpha_1}{\rho}\left(\frac{\partial^2 u}{\partial x \partial y}\frac{\partial u}{\partial y} + u\frac{\partial^3 u}{\partial x \partial y^2} + v\frac{\partial^3 u}{\partial y^3} - \frac{\partial u}{\partial x}\frac{\partial^2 u}{\partial y^2}\right), \tag{4.2}$$

$$u\frac{\partial T}{\partial x} + v\frac{\partial T}{\partial y} - \frac{\mu_0 K_p T}{\rho c_p}\left(u\frac{\partial H}{\partial x} + v\frac{\partial H}{\partial y}\right) = \alpha\frac{\partial^2 T}{\partial y^2}. \tag{4.3}$$

Here α_1 signifies the normal stresses moduli. The assumed admissible boundary conditions are

$$u|_{y=0} = U_w(x) = Sx, \, v|_{y=0} = 0, \, T|_{y=0} = T_w = T_0 + b_1 x, \tag{4.4}$$

$$u|_{y\to\infty} \to U_e(x) = Qx, \, T|_{y\to\infty} \to T_c = T_0 + b_2 x. \tag{4.5}$$

The physical schematic of ferrofluid is shown in Figure 4.1. Here the circular lines indicate the magnetic field.

4.3   Solution procedure

The assumed dimensionless variables are

$$\psi(\eta, \xi) = \eta(\frac{\mu}{\rho})f(\xi), \theta(\xi, \eta) \equiv \frac{T_c - T}{T_w - T_0} = \theta_1(\xi) + \eta^2\theta_2(\xi), \tag{4.6}$$

here $\theta_2(\xi)$ and $\theta_1(\xi)$ exhibit dimensionless temperature, the corresponding dimensionless coordinates are

$$\xi = y\sqrt{\frac{\rho S}{\mu}}, \eta = x\sqrt{\frac{\rho S}{\mu}}. \tag{4.7}$$

The stream function is defined in this fashion that the mass equation satisfies directly, here the $\psi(\eta, \xi)$ signifies the stream function, (u, v) symbolizes the comparable components of velocity defined below

$$u = \frac{\partial\psi(\eta, \xi)}{\partial y} = Sxf'(\xi), v = -\frac{\partial\psi(\eta, \xi)}{\partial x} = -\sqrt{S\nu}f(\xi), \tag{4.8}$$
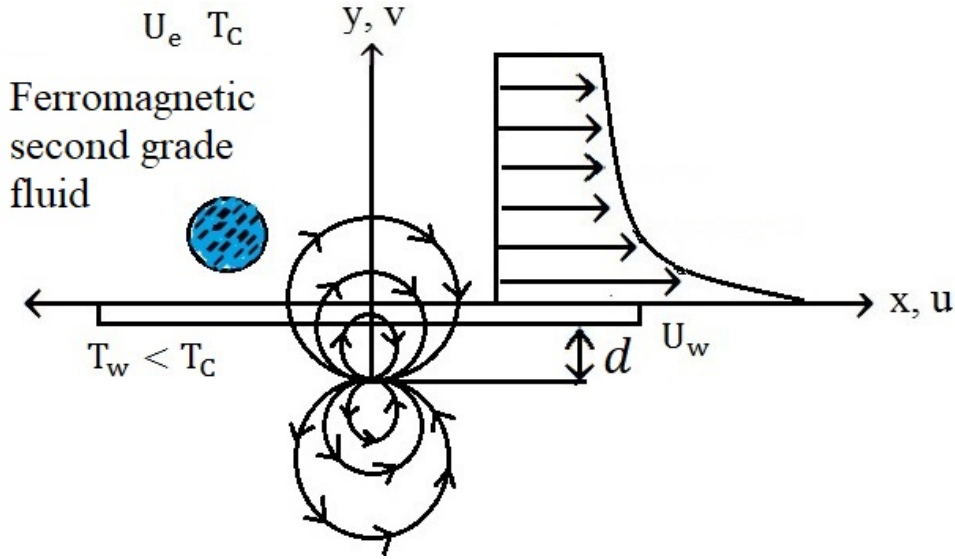
Figure 4.1: Geometery of the flow.

where prime expresses differentiation with respect to ξ and η. Employing the similarity transformations given in Eqs. (2.6)-(2.12) and (4.6) to (4.8), equations (4.2) and (4.3) along with stated boundary conditions given in Eqs. (4.4) and (4.5) reduce to the following equations

$$f''' + \delta_m(f''f''' + 2f'f'' - ff^{(iv)}) - f'^2 + ff'' - \frac{2\beta\theta_1}{(\xi+\gamma)^4} + R^2 = 0, \qquad (4.9)$$

$$\theta_1'' + Pr f\theta_1' + \frac{2\lambda\beta\ f(\theta_1 - \varepsilon)}{(\xi+\gamma)^3} + 2\theta_2 - 4\lambda f'^2 = 0, \qquad (4.10)$$

$$\theta_2'' - Pr(2f'\theta_2 - f\theta_2') + \frac{2\lambda\beta\ f\theta_2}{(\xi+\gamma)^3} - 4\lambda f''^2$$

$$+ \beta\lambda\ (\varepsilon - \theta_1)\left(\frac{2f'}{(\xi+\gamma)^4} + \frac{4f}{(\xi+\gamma)^5}\right) = 0, \qquad (4.11)$$

$$f'(\xi) = 1, f(\xi) = 0, \theta_1(\xi) = 1 - S_1, \theta_2(\xi) = 0, \quad at\ \xi = 0, \qquad (4.12)$$

$$f'(\xi) \to R, \theta_1(\xi) \to 0, \theta_2(\xi) \to 0, \quad when\ \xi \to \infty. \qquad (4.13)$$

In above system of nonlinear equations, the parameters δ_m (elasticity parameter) β (ferrohydrodynamic interaction), λ (viscous dissipation), R (ratio), S_1 (thermal

stratified parameter), ε (Curie temperature), and Pr (Prandtl number) are defined as

$$R = \frac{Q}{S}, Pr = \frac{\nu}{\alpha}, \varepsilon = \frac{T_\infty}{T_w - T_0}, \beta = \frac{\gamma_1}{2\pi} \frac{\mu_0 K_p (T_w - T_0)\rho}{\mu^2},$$
$$\lambda = \frac{S\mu^2}{\rho K_p (T_w - T_0)}, \delta_m = \frac{\alpha_1 S}{\rho \nu}, \gamma = \sqrt{\frac{S\rho d^2}{\mu}}, S_1 = \frac{b_2}{b_1}. \tag{4.14}$$

At the walls, the parameters of engineering interest, i.e, the friction drag and rate of heat transfer are

$$C_f = \frac{2\tau_w}{\rho U_w^2}, \tau_w = \mu \frac{\partial u}{\partial y}\Big|_{y=0} + \alpha_1 \left(\frac{\partial u}{\partial y} \frac{\partial u}{\partial x} + \frac{\partial^2 u}{\partial y^2} - \frac{\partial v}{\partial y} + u \frac{\partial^2 u}{\partial x \partial y} \right)\Big|_{y=0},$$
$$Nu_x = \frac{x}{T_w - T_0} \frac{\partial T}{\partial y}\Big|_{y=0}. \tag{4.15}$$

We finally, achieved the following non-dimensional equations

$$\frac{1}{2} Re^{1/2} C_f = f''(0) + \delta_m (f'((0)f''(0) - f'''(0)f(0)),$$
$$Re^{-1/2} Nu_x = -(\theta_1'(0) + \eta^2 \theta_2'(0)). \tag{4.16}$$

4.3.1 Optimal homotopy analysis method

The series solution for the present boundary value problem is deliberated via optimal HAM. The mechanism is utilized to demonstrate solutions for non-linear equations. The entire interpretation can be found in [96, 97]. In the evaluation of the problem one needs the linear operators and initial guesses which are given below

$$L_f(f) = \frac{d^3 f}{d\xi^3} + \frac{d^2 f}{d\xi^2}, L_{\theta_1}(\theta_1) = \frac{d^2 \theta_1}{d\xi^2} - \theta_1,$$
$$L_{\theta_2}(\theta_2) = \frac{d^2 \theta_2}{d\xi^2} - \theta_2. \tag{4.17}$$

$$f_0(\xi) = 1 + (\xi - 1)R - (1 - R)exp(-\xi), \theta_{1_0}(\xi) = (1 - S_1)exp(-\xi),$$
$$\theta_{2_0}(\xi) = \xi exp(-\xi), \tag{4.18}$$

where $L_f(f)$, $L_{\theta_1}(\theta_1)$, and $L_{\theta_2}(\theta_2)$ symbolizes the linear operators, furthermore, $f_0(\xi)$, $\theta_{1_0}(\xi)$ and $\theta_{2_0}(\xi)$ illustrate the initial guesses of f, θ_1, and θ_2.

4.3.2 Convergence analysis

The auxiliary/subsidiary parameters h_f, h_{θ_1}, and h_{θ_2} have remarkable intention in controlling the convergence of series solutions. To get a convergent analytic solutions,

preferred values are assigns to h_f, h_{θ_1}, and h_{θ_2}. For this reason, residual errors are observed for ferrohydrodynamic equations by implementing the expressions defined in Eqs. (2.26)-(2.28). These expressions are utilized in the evaluation of convergence for the optimal HAM, the resulting convergence and residual errors are listed in tables 4.1 and 4.2. Figures 4.2 and 4.3 reveal the average residual square error for 10th and 12th order. Δ_m^f exhibits the total square residual error, defined in Eq. (2.29).

$\frac{values\rightarrow}{order\downarrow}$	h_f	h_{θ_1}	h_{θ_2}	Δ_m^t
4	-0.914901	-0.834128	-1.09223	4.61754×10^{-8}
6	-1.01206	-0.932163	-1.0271	1.59062×10^{-11}
8	-1.05365	-0.914006	-1.0644	6.70151×10^{-15}
10	-1.00068	-0.949574	-1.03027	1.01087×10^{-18}
12	-1.03177	-0.92185	-1.06242	4.11943×10^{-22}

Table 4.1: Average residual square errors Δ_m^t.

$\frac{values\rightarrow}{order\downarrow}$	$h_f = -1.03177$	$h_{\theta_1} = -0.92185$	$h_{\theta_2} = -1.06242$
4	1.14111×10^{-9}	8.74605×10^{-10}	8.60314×10^{-8}
8	3.63587×10^{-19}	1.22724×10^{-16}	6.74969×10^{-15}
12	8.25911×10^{-24}	1.79475×10^{-20}	2.28596×10^{-18}
20	2.59611×10^{-28}	9.85676×10^{-24}	4.02086×10^{-22}

Table 4.2: Individual residual square errors for Δ_m^f, $\Delta_m^{\theta_1}$, and $\Delta_m^{\theta_2}$.
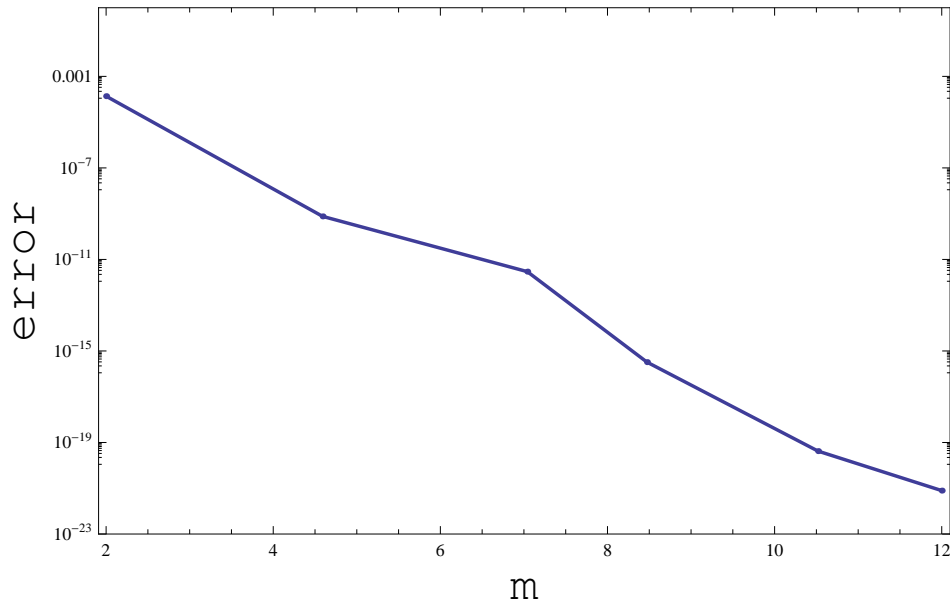
Figure 4.2: Graph for 10th order approximation.
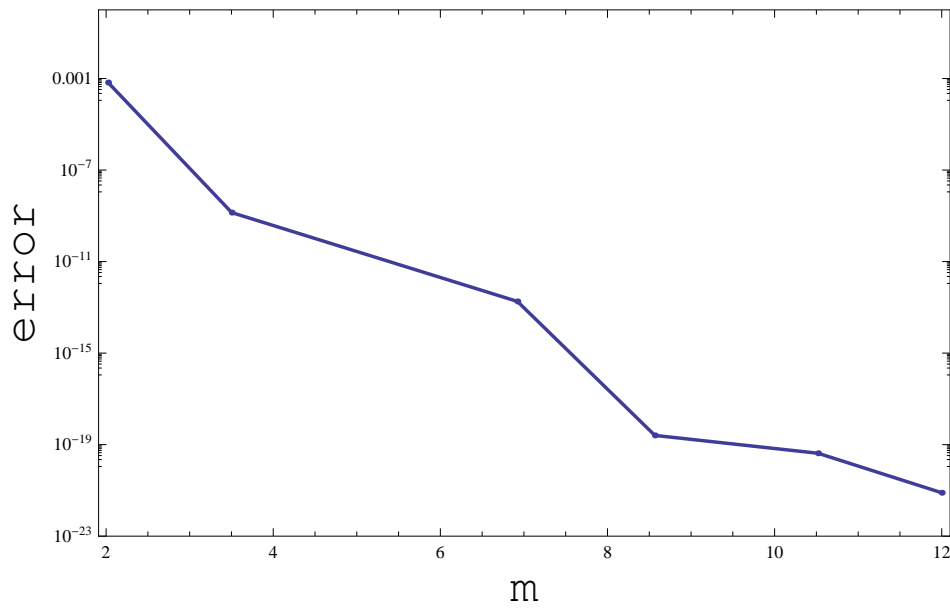
Figure 4.3: Graph for 12th order approximation.

4.4   Discussion

The analytical solutions of boundary value problem described in Eqs. 4.9-4.13 are obtained through optimal HAM. The characteristics of sundry consequential parameters on fluid flow are deliberated in this section. The impacts of dimensionless parameters δ_m (elasticity parameter), β (ferrohydrodynamic interaction), λ (viscous dissipation), S_1 (thermal stratified), R (ratio), γ (dimensionless distance from origin to center of magnetic dipole), and Pr (Prandtl number) are scrutinized. Moreover, rest of the parameters appearing in the flow framework are treated fixed. The established values of these parameters are $\lambda = 0.1$, $\gamma = 1.0$, and $\varepsilon = 2.0$. The values assigned to remaining parameters are $\beta = 1.0$; $R = 0.5$; $S_1 = 0.2$, $\delta_m = 0.5$, and $Pr = 2.0$.

The effects of elasticity or second grade parameter δ_m are evident in Figure 4.4. It is confirmed that for increasing values of parameter δ_m (elasticity), velocity profile enhances deliberately, the result indicates that axial velocity and complementary boundary layer becomes large with the improvement of δ_m, i.e., velocity boundary layer is growingly thicker. It is scrutinized that response velocity growing up by arising (increasing values of δ_m) of an elastic force of the fluid.

Meanwhile by taking $\delta_m = 0$, the forces at surface reach its least possible value, which stipulates that the interior elastic force of liquid are absent, by cause of which the fluid becomes a classical Newtonian fluid. Figure 4.5 specify that the boundary layer thickness of temperature field are increasingly thinner with an increase of elasticity parameter δ_m, which declares that thermal transmission becomes faster. Moreover, it also depicts that less time will be essential to generate the thermal boundary layer with elasticity parameter δ_m.

The impact of parameter β(ferrohydrodynamic interaction) is incorporated in Figures 4.6 and 4.7. The presence of parameters, β (ferrohydrodynamic interaction), ε (Curie temperature), and γ (dimensionless distance from magnetic dipole center to origin) are essential to stabilizing the impact of ferromagnetic effect on flow problem. The existence of particles (micro sized) of ferrite in second grade carrier fluid leads to ferromagnetic fluid, due to which viscosity of the fluid arises and as a result reduction takes place in velocity field for increasing values of parameter β (ferrohydrodynamic interaction), which is exhibited in Figure 4.6. The impacts of parameter β (ferrohydrodynamic interaction) on distribution of temperature are evident in Figure 4.7. It is noticed that giving variation to parameter β (ferrohydrodynamic interaction), causes an enhancement in temperature of the fluid inside the boundary layer. The communication between particles of fluid and action of magnetic field reduces velocity field so that arising frictional heating surrounded by fluid layers leads to thicked

thermal boundary layer i.e., the reduction in movements of particles of fluid causes improvement in heat transfer, which is displayed in Figure 4.7.

The influence of parameter S_1 (thermal stratified) on axial velocity and temperature field is characterized for the present analysis. Figures 4.8 and 4.9 designates that axial velocity and temperature field declines for the corresponding variation in thermal stratification parameter S_1. The described reduction in the distribution of temperature is due to decay in temperature difference between the surface and away from the sheet. Increase in parameter S_1 (thermal stratified) leads to increase the density of fluid layers, due to which the dense particles of ferrite move toward the surface that gives rise to magnetohydrodynamic interaction, which is responsible for a reduction in axial velocity and enhancement in heat transfer rate.

The effect of Pr (Prandtl number) in temperature equation has arisen because of ratio of momentum and thermal diffusivity. The existence of Pr (Prandtl number) in temperature equations influences their corresponding response. Its characteristics are quite opposite as compared to parameter β (ferrohydrodynamic interaction) on temperature field. Figures 4.10 and 4.11 indicate the influence of Pr (Prandtl number). The increase in axial velocity and a decline in heat transfer is noticed. Physically, thermal diffusivity reduces by enhancing the parameter Pr (Prandtl number). Reduction in thermal diffusivity is responsible for heat distributed away from the heated sheet and by the way, the temperature gradient at wall is rising. This phenomenon decreases the ability of energy that decline thermal boundary layer and arises the axial velocity.

The effects of parameter R (ratio) on axial velocity is incorporated. The parameter R indicates the ratio of ambient fluid velocity to surface velocity due to a stretchable sheet. Figure 4.12 delineates the impacts of parameter R (ratio) on axial velocity. The characteristics of R were quite different for $R > 1$ and for $R < 1$. Keep in mind that when $R > 1$, it represents the case where fluid move with high velocity as compare to surface and $R < 1$ demonstrates the case when surface move with the higher velocity as compare to fluid. Further, there is no change in axial velocity for $R = 1.0$. Improvement in axial velocity is noticed for enlarging values of ratio parameter R.
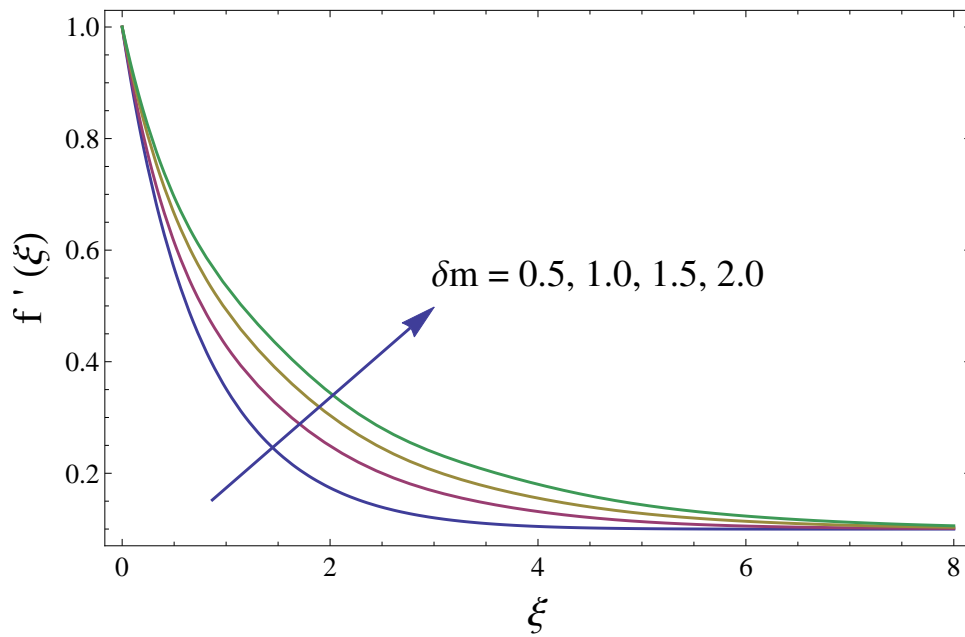
Figure 4.4: Impact of elasticity parameter (δ_m) on velocity distribution.
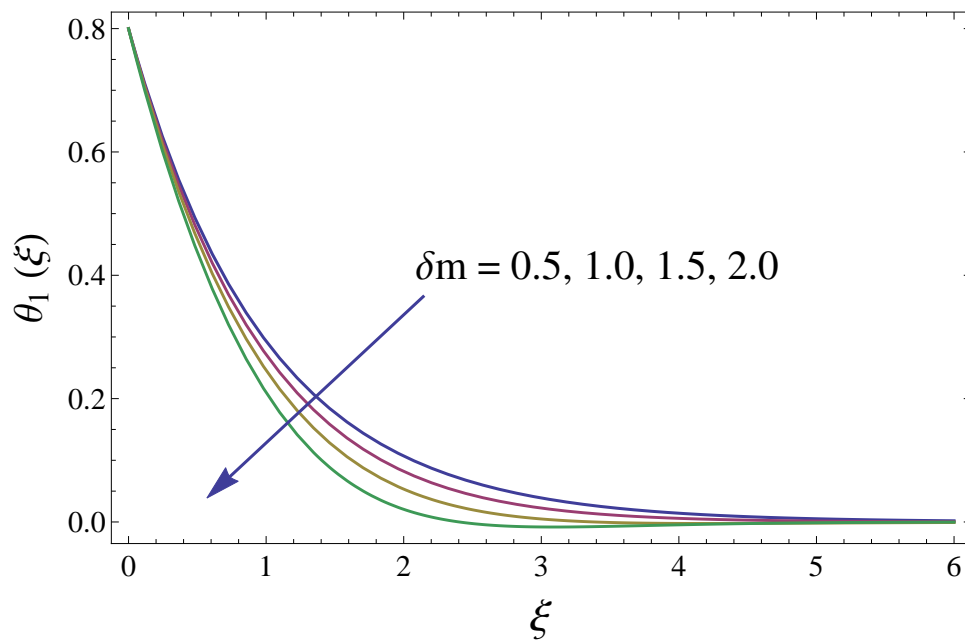
Figure 4.5: Influence of elasticity parameter (δ_m) on distribution of temperature.
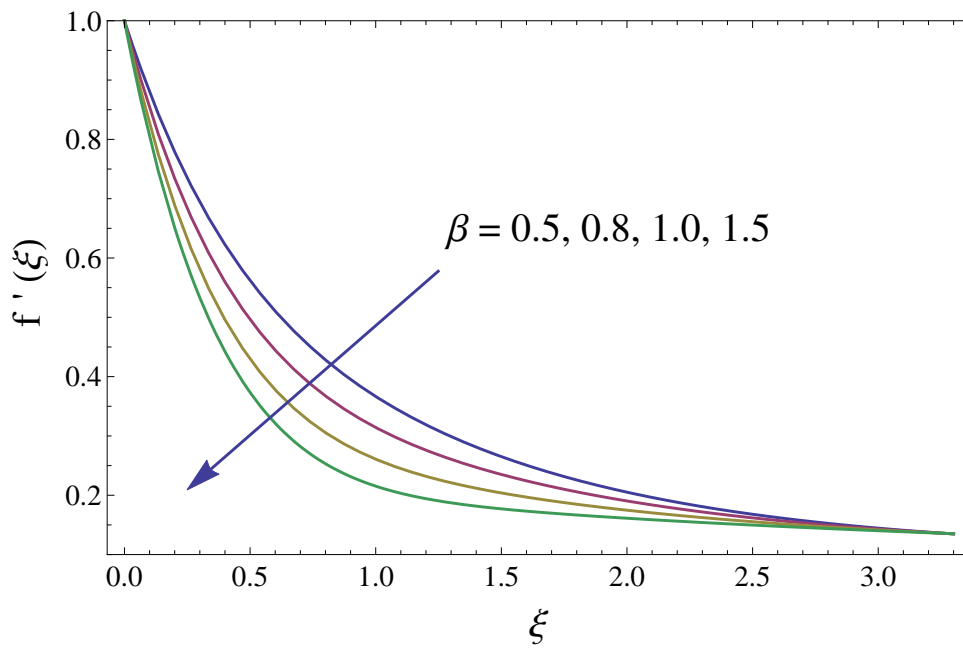
Figure 4.6: Consequence of ferrohydrodynamic interaction parameter (β) on velocity field.
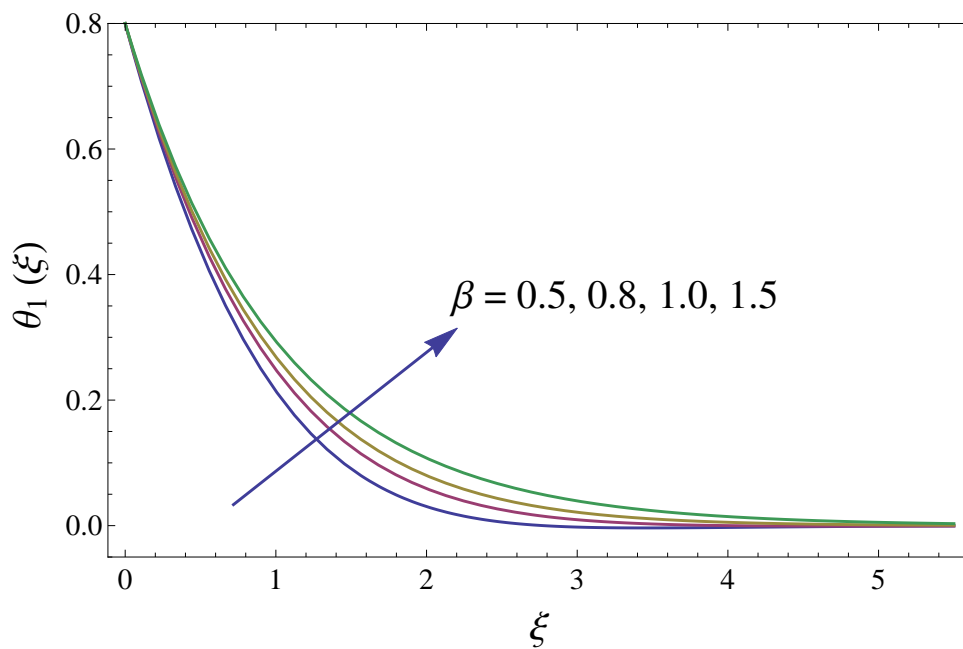
Figure 4.7: Impact of ferrohydrodynamic interaction parameter (β) on temperature field.
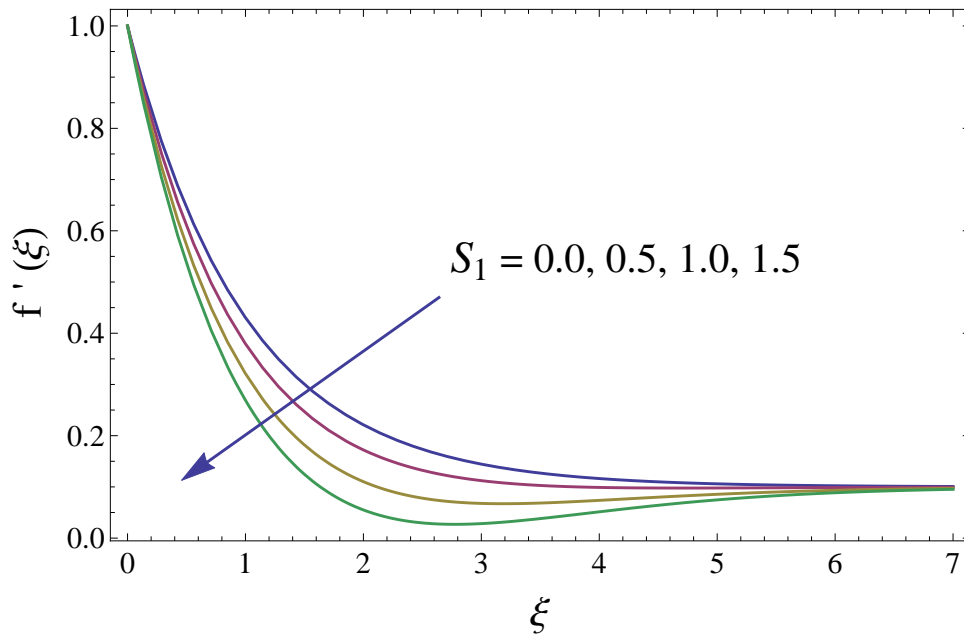
Figure 4.8: Consequence of (S_1) thermal stratified parameter on velocity field $(f'(\xi))$.
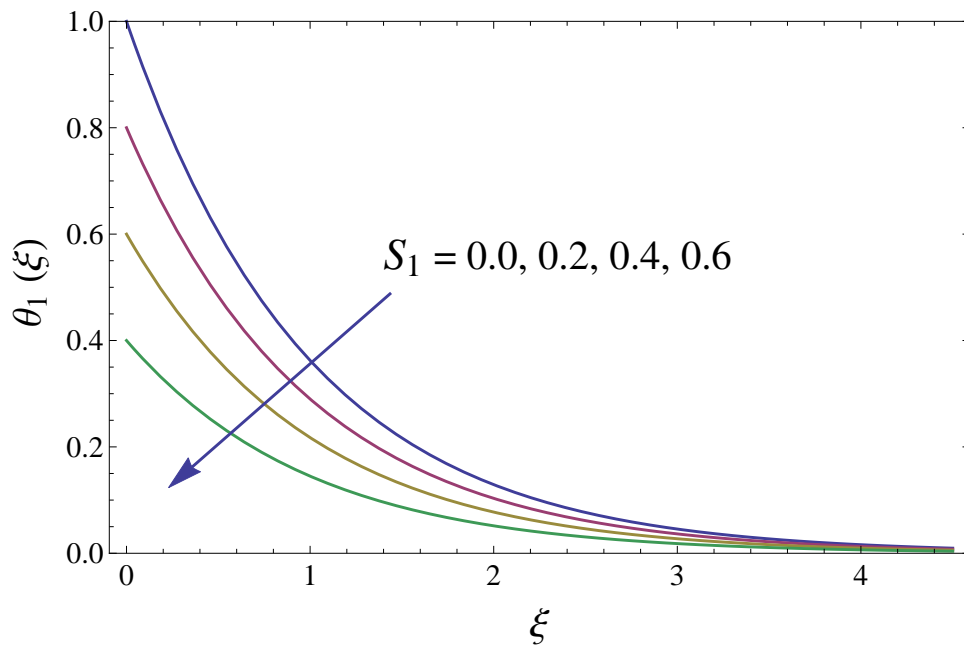
Figure 4.9: Variation of (S_1) thermal stratified parameter on temperature field $(\theta_1(\xi))$.
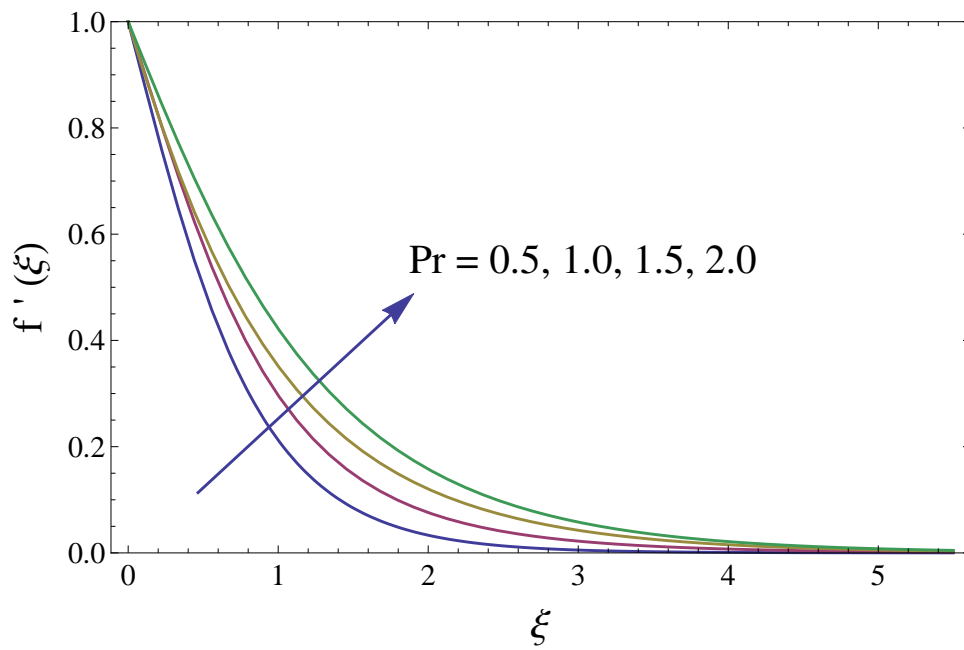
Figure 4.10: Consequence of (Pr) Prandtl number on axial velocity $(f'(\xi))$.
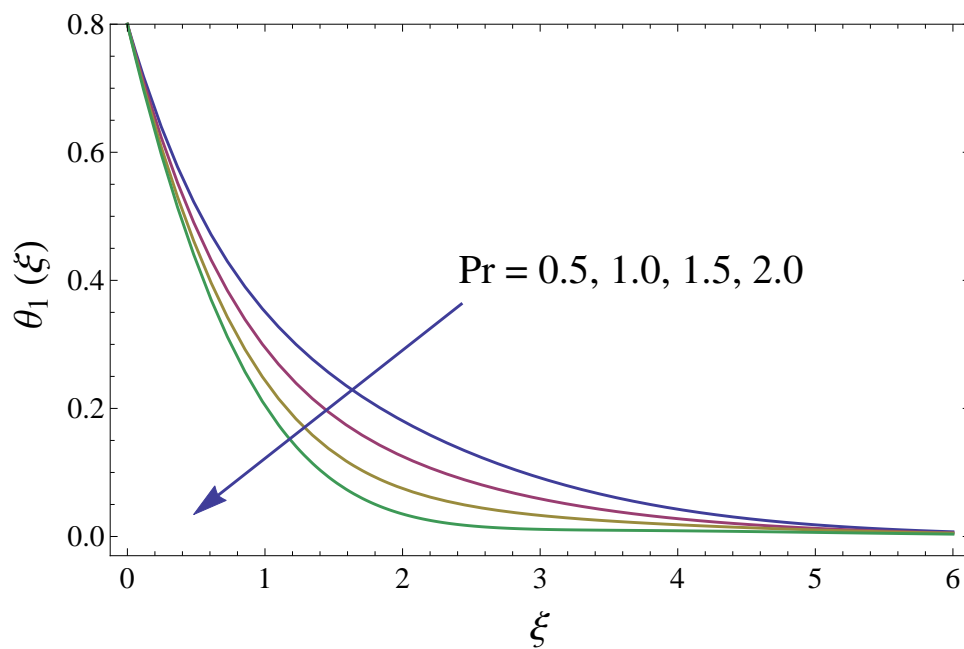
Figure 4.11: Consequence of (Pr) Prandtl number on distribution of temperature $(\theta_1(\xi))$.
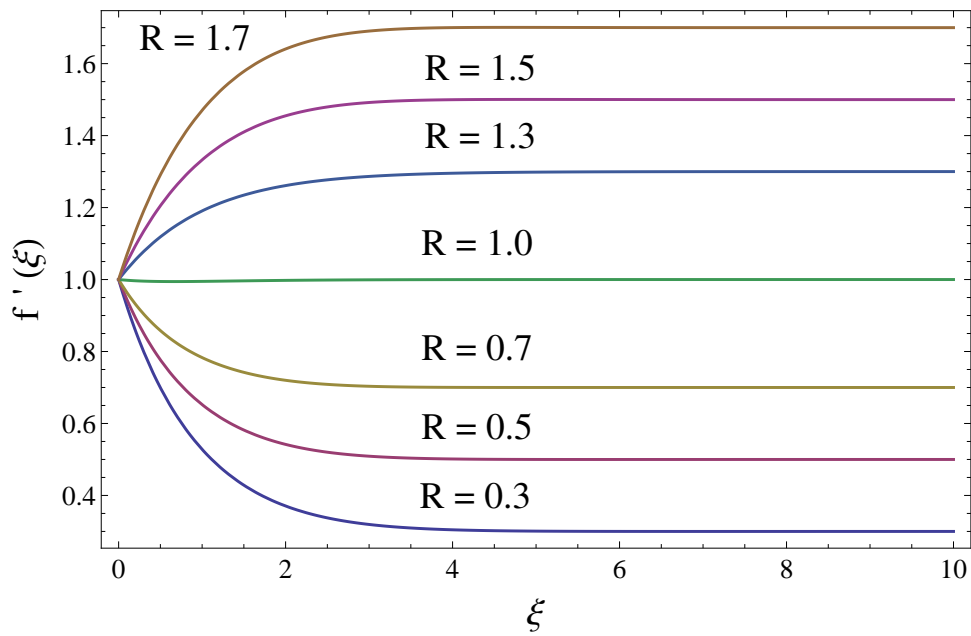
Figure 4.12: Impact of ratio parameter (R) on axial velocity $(f'(\xi))$.

4.4.1   Friction drag and local Nusselt number

Eqs. 4.15 and 4.16 describe the mathematical form for friction drag and Nusselt number. The consequence indueced by the parameter R on skin friction is characterized in Figure 4.13. The friction drag enhances for increasing values of parameter R. Figure 4.13 indicates that when $R = 0$, there is no change, it is because of the similarity between fluid velocity and sheet velocity due to stretching. Further, for higher values of parameter R, the fluid velocity dominate the plate velocity, which corresponds to enhancement in axial velocity, as a result, skin friction coefficient reduces. While Figure 4.14 designates the impact of parameter S_1 (thermal stratified) on wall shear stress. It is observed that larger stratification parameter gives rise to wall shear stress. Further, the features of parameters Pr (Prandtl number) and S_1 (thermal stratification) via heat transfer rate are given in Figures 4.15 and 4.16. It is scrutinized from Figure 4.15 that variation in parameter Pr causes a reduction in the heat transfer rate, instead of from Figure 4.16, it is perceived that enhancement in parameter S_1 leads to enhance the transfer of heat. Tables 4.3 and 4.4 display the comparison of Nusselt number along friction drag.
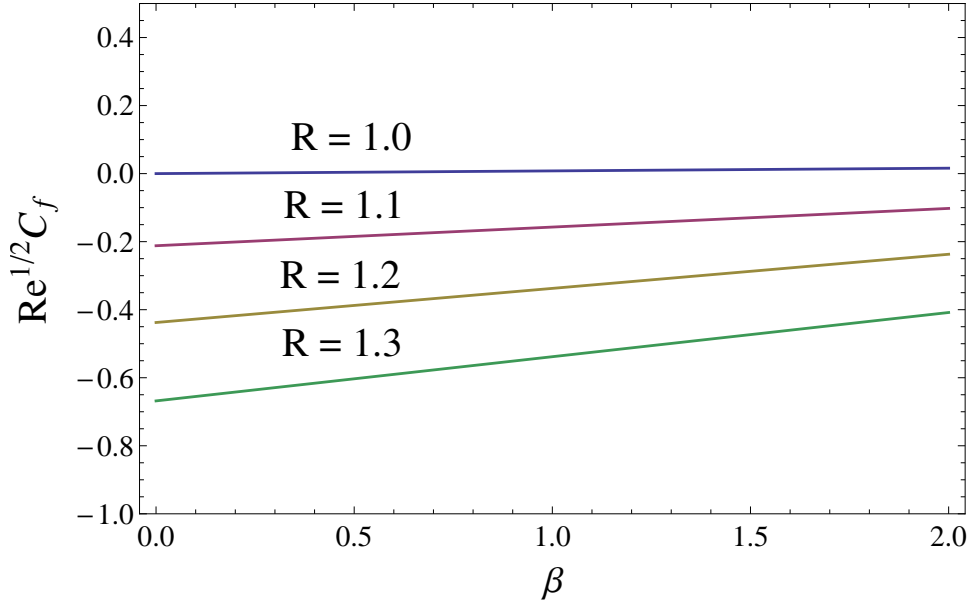
Figure 4.13: Wall shear stress versus R.
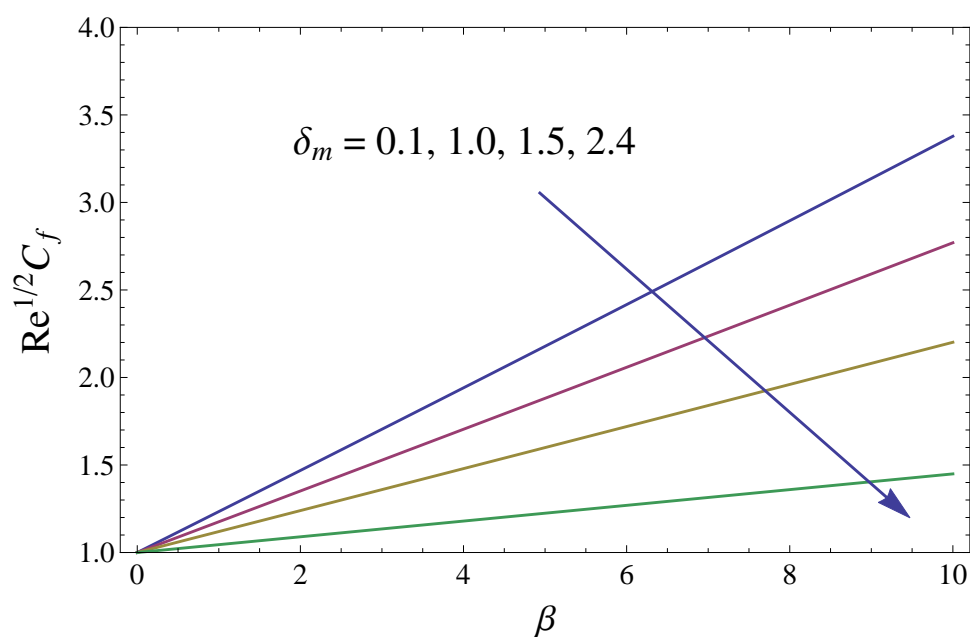
Figure 4.14: Wall shear stress versus S_1.
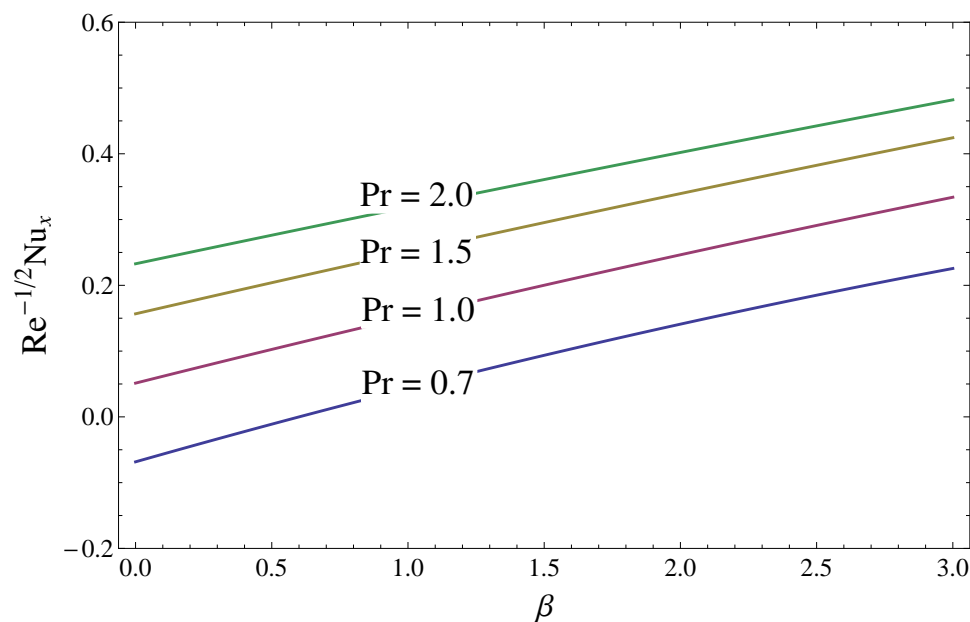
Figure 4.15: Heat transfer rate versus Pr.
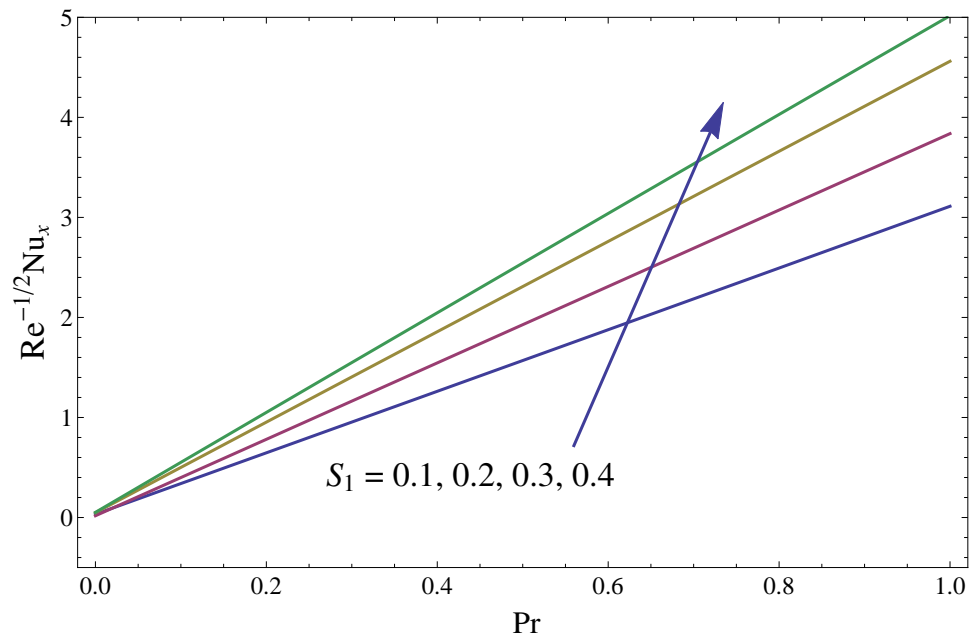
Figure 4.16: Heat transfer rate versus S_1.

Pr	Chen [93]	Abel et al. [95]	$\mathrm{Re}_x^{-1/2}\,\mathrm{Nu}_x$ (Optimal HAM)
0.72	1.0885	1.0885	1.088521
1.0	1.3333	1.3333	1.333306
2.0	2.0210	$---$	2.021092
3.0	2.5097	$---$	2.509762
4.0	$---$	$---$	2.903051
10.0	4.7968	4.7968	$---$

Table 4.3: Comparison of Nusselt number.

Pr	β	δ_m	S_1	$\mathrm{Re}_x^{1/2}\,\mathrm{C}_f$	$\mathrm{Re}_x^{-1/2}\,\mathrm{Nu}_x$
1.0	1.0	0.2	0.2	1.0590	1.2923
2.0				1.0329	2.0928
3.0				1.0289	2.3828
2.0	1.0	0.2	0.2	1.2976	2.4426
	2.0			1.5032	2.3213
	3.0			1.6121	2.3172
2.0	1.0	0.2	0.2	1.1248	0.80757
		0.4		1.0868	0.90595
		1.0		1.0263	0.99595
2.0	1.0	0.2	0.2	1.1248	0.80757
			0.4	1.15317	0.90386
			0.6	1.35607	0.99310

Table 4.4: The friction drag and Nusselt number tabulated via series solution based on optimal HAM.

Concluding remarks

The characteristics of thermal stratification on the ferromagnetic fluid over a stretchable surface along the external magnetic dipole is carried out. Optimal HAM (Homotopy Analysis Method) and Bvph2−midpoint techniques are employed in the evaluation of the influence of magneto-thermomechanical coupling on the ferrohydrodynamic flow. The key points of the flow problem are bellow.

- An increment in parameter β (ferromagnetic interaction) gives rise to heat transfer thereby reducing axial velocity.

- Higher values of parameter δ_m (elasticity), the axial velocity enhances gradually whereas the temperature field reduces.

- Variation in parameter R (ratio) results in an increment in axial velocity, while the wall shears stress decreases.

- λ_1 declines the axial velocity whereas increases the temperature field.

- Higher values of parameter S_1 (thermal stratification) corresponds to thinning of velocity and temperature fields. Further, the heat transfer rate strengthen for increasing values of parameter S_1.

- Pr (Prandtl number) leads to decline temperature field, whereas, enhances the axial velocity.

Chapter 5

Hybrid isothermal model for the ferrohydrodynamic chemically reactive species

5.1   Introduction

This chapter concentrates on the hybrid isothermal model for the chemically reactive species i.e., homogeneous-heterogeneous reactions in ferrohydrodynamic flow. The characteristics of Newtonian heating and magnetic dipole in a ferrofluid due to a stretchable surface is analyzed for three chemical species. It is presumed that the isothermal cubic autocatalator kinetic gives the homogeneous reaction and the first order kinetics gives the heterogeneous (surface) reaction. The analysis is carried out for equal diffusion coefficients of all autocatalyst and reactions. The transport equations are taken by incorporating the boundary layer assumptions. Further, the boundary value problem is clarify analytically as a consequence of BVPh2-midpoint method and optimal homotopy analysis method (optimal HAM). Characteristics of materialized parameters on the magneto-thermomechanical coupling in the flow of a chemically reactive species are investigated. Further, the heat transfer rate with friction drag are depicted for the ferrohydrodynamic chemically reactive species. Schmidt number improve the transfer of heat in the flow. The materialized parameters are described via graphs and tables.

5.2   Ferrohydrodynamic and thermal energy equations

A hybrid model for homogeneous-heterogeneous reactions are scrutinized for the incompressible ferrohydrodynamic boundary layer flow along with the isothermal cubic autocatalytic reactions, declare schematically by

$$A + C + C \quad \to \quad 3C, \quad rate = k_1 ac^2 \tag{5.1}$$

$$B + C + C \quad \to \quad 3C, \quad rate = k_1 bc^2 \tag{5.2}$$
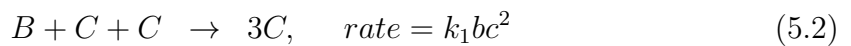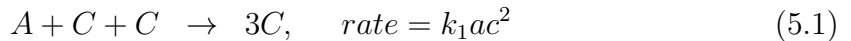
while the first order, hybrid isothermal reactions on the catalyst surface are

$$A \quad \to \quad C, \quad rate = k_s a \tag{5.3}$$

$$B \quad \to \quad C, \quad rate = k_s b \tag{5.4}$$

here a, b, and c characterizes the concentrations of chemical species A, B and C. It is presumed that the reactants A and B have constant concentration a_0 and in the external flow there is no autocatalyst C. Then the reactions given in Eqs. (5.1) and (5.2) confirms that at the outer edge of the boundary layer and in the exterior

flow the reaction rate will be zero. The heat released by the reaction is considered negligible. By exerting a force on the sheet located at $y = 0$ introduces stretching in the sheet having velocity $U_w(x)$. The flow is scrutinized in the presence of a magnetic dipole. The center of magnetic dipole is kept along vertical axis at a distance d below $x-$axis. The magnetic field points of magnetic dipole are taken along positive $x-$axis. An enhancement in the strength of magnetic field driven by magnetic dipole leads to saturate the ferrofluid. The temperature $T = T_\infty$ is assumed to be fluid temperature away from the surface, where $T_\infty < T_w < T_c$. The fluid above Curie temperature is incapable of being magnetized. The impacts of heat absorption/generation are taken to be negligibly small. Making use of boundary layer approach, the governing equations becomes

$$\frac{\partial u}{\partial x} + \frac{\partial v}{\partial y} = 0, \tag{5.5}$$

$$u\frac{\partial u}{\partial x} + v\frac{\partial u}{\partial y} = -\frac{1}{\rho}\frac{\partial P}{\partial x} + \frac{\mu_0 M}{\rho}\frac{\partial H}{\partial x} + \frac{\mu}{\rho}\frac{\partial^2 u}{\partial y^2}, \tag{5.6}$$

$$u\frac{\partial T}{\partial x} + v\frac{\partial T}{\partial y} - \frac{\mu_0 K_p T}{\rho c_p}\left(u\frac{\partial H}{\partial x} + v\frac{\partial H}{\partial y}\right) = \alpha\frac{\partial^2 T}{\partial y^2}, \tag{5.7}$$

$$u\frac{\partial a}{\partial x} + v\frac{\partial a}{\partial y} = D_A\frac{\partial^2 a}{\partial y^2} - k_1 ac^2, \tag{5.8}$$

$$u\frac{\partial b}{\partial x} + v\frac{\partial b}{\partial y} = D_B\frac{\partial^2 b}{\partial y^2} - k_1 bc^2, \tag{5.9}$$

$$u\frac{\partial c}{\partial x} + v\frac{\partial c}{\partial y} = D_C\frac{\partial^2 c}{\partial y^2} + k_1 ac^2 + k_1 bc^2. \tag{5.10}$$

Boundary conditions are

$$u|_{y=0} = U_w(x) = Sx, \, v|_{y=0} = 0, \, \left.\frac{\partial T}{\partial y}\right|_{y=0} = -h_s T,$$

$$D_A\left.\frac{\partial a}{\partial y}\right|_{y=0} = k_s a, \, D_B\left.\frac{\partial b}{\partial y}\right|_{y=0} = k_s a, \, D_C\left.\frac{\partial c}{\partial y}\right|_{y=0} = -k_s a, \tag{5.11}$$

$$u|_{y\to\infty} \to 0, \, T|_{y\to\infty} \to T_\infty = T_c, \, a|_{y\to\infty} \to a_0,$$

$$b|_{y\to\infty} \to a_0, \, c|_{y\to\infty} \to 0. \tag{5.12}$$

Here $U_w(x)$ exemplify the characteristic velocity. In the above equations, S designate dimensionless constants, and h_s identify heat transfer coefficient. The materialistic schematic of ferrofluid is delineated in Figure 5.1.
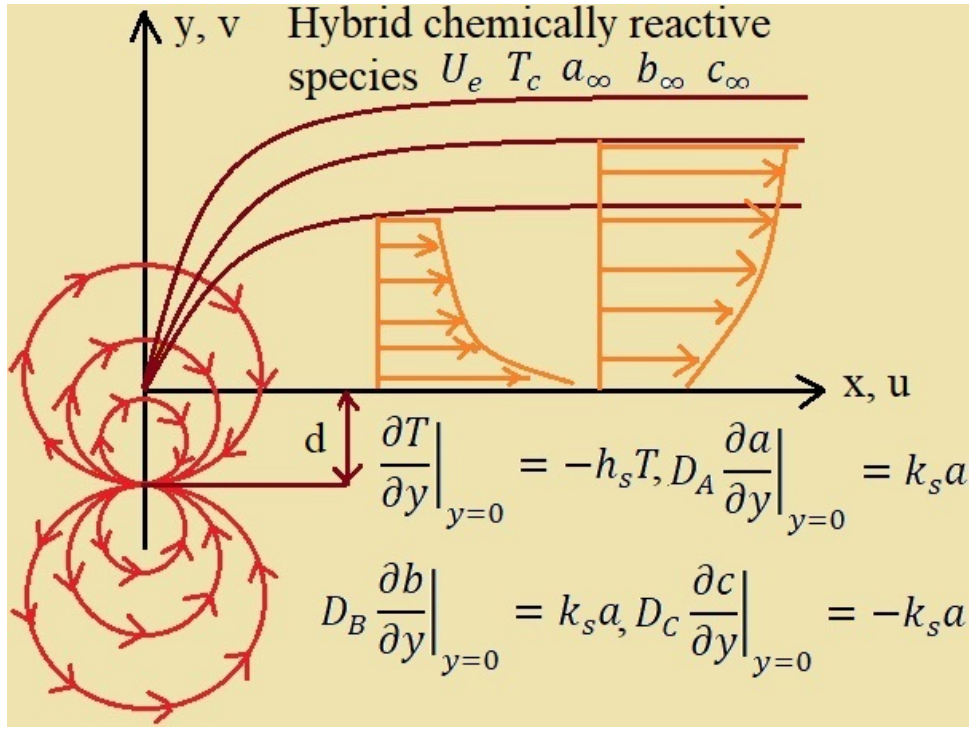
Figure 5.1: Geometery of the flow.

5.3　Solution procedure

The assumed dimensionless variables for the present analysis are

$$\psi(\eta,\xi) = \eta(\frac{\mu}{\rho})f(\xi), \quad a = a_0 g(\xi), \quad b = a_0 h(\xi),$$

$$c = a_0 j(\xi), \quad \theta(\xi,\eta) \equiv \frac{T_\infty - T}{T_c} = \theta_1(\xi) + \eta^2 \theta_2(\xi). \tag{5.13}$$

Here $\theta_2(\xi)$ and $\theta_1(\xi)$ exhibit dimensionless temperature, the corresponding dimensionless coordinates are

$$\xi = \frac{y}{l}\sqrt{Re}, \quad \eta = \frac{x}{l}\sqrt{Re}, \quad Re = \frac{Sl^2}{\nu}. \tag{5.14}$$

The stream function $\psi(\eta,\xi)$ is defined in such a way that the mass equation satisfies directly, (u,v) symbolizes the comparable components of velocity defined below

$$u = \frac{\partial\psi(\eta,\xi)}{\partial y} = Sxf'(\xi), \quad v = -\frac{\partial\psi(\eta,\xi)}{\partial x} = -\sqrt{\frac{S\mu}{\rho}}f(\xi), \tag{5.15}$$

where prime expresses differentiation with respect to ξ and η. Employing the similarity transformations given in Eqs. (2.6)-(2.12) and (4.13) to (4.15), equations $(4.6 - 4.10)$

along with stated boundary conditions given in Eq. (4.11) and (4.12) reduce to the system of coupled equations as follow

$$f''' - f'^2 + ff'' - \frac{2\beta\theta_1}{(\xi + \gamma)^4} = 0, \tag{5.16}$$

$$\theta_1'' + Prf\theta_1' + \frac{2\lambda\beta\ f(\theta_1 - \varepsilon)}{(\xi + \gamma)^3} + 2\theta_2 - 4\lambda f'^2 = 0, \tag{5.17}$$

$$\theta_2'' - Pr(2f'\theta_2 - f\theta_2') + \frac{2\lambda\beta\ f\theta_2}{(\xi + \gamma)^3} - 4\lambda f''^2$$
$$+ \beta\lambda\ (\varepsilon - \theta_1)\left(\frac{2f'}{(\xi + \gamma)^4} + \frac{4f}{(\xi + \gamma)^5}\right) = 0, \tag{5.18}$$

$$\frac{1}{Sc}g'' + fg' - K_hgj^2 = 0, \tag{5.19}$$

$$\frac{\delta_1}{Sc}h'' + fh' - K_hhj^2 = 0, \tag{5.20}$$

$$\frac{\delta_2}{Sc}j'' + fj' + K_hj^2(g + h) = 0. \tag{5.21}$$

$$f'(\xi) = 1, f(\xi) = 0, \theta_1'(\xi) = -\delta_h(1 + \theta_1(\xi)), \theta_2(\xi) = 0,$$
$$g'(\xi) = K_sg(0), \delta_1h'(\xi) = K_sg(0), \delta_2j'(\xi) = K_sg(0),\ at\ \xi = 0, \tag{5.22}$$

$$f'(\xi) \to 0, \theta_1(\xi) \to 0, \theta_2(\xi) \to 0, g(\xi) \to 1, h(\xi) \to 1, j(\xi) \to 0,\ when\ \xi \to \infty. \tag{5.23}$$

In above boundary value problem, the dimensionless materialized parameters are β (ferrohydrodynamic interaction), K_h and K_s (strengths of homogeneous and heterogeneous reactions respectively), λ (viscous dissipation), ε (Curie temperature), δ_1 and δ_2 (ratio of diffusion coefficients), δ_h (Conjugate parameter due to Newtonian heating), Sc (Schmidt number), Pr (Prandtl number), and γ (dimensionless distance) are described as

$$\delta_1 = \frac{D_B}{D_A}, Pr = \frac{\nu}{\alpha}, \beta = \frac{\gamma_1}{2\pi}\frac{\mu_0K_pT_c\rho}{\mu^2}, K_s = \frac{k_sl}{D_A\sqrt{Re}}, \varepsilon = \frac{T_\infty}{T_c},$$
$$K_h = \frac{k_1a_0^2l}{S}, \delta_h = lh_s\sqrt{\frac{\mu}{\rho lS}}, \lambda = \frac{S\mu^2}{\rho K_pT_c}, \gamma = \sqrt{\frac{S\rho d^2}{\mu}}, \delta_2 = \frac{D_C}{D_A}. \tag{5.24}$$

The chemically reactive species A, B and C are considered to be of the same size, due to this assumption the diffusions species coefficients D_A, D_B, and D_C, are equivalent i.e., $\delta_1 = \delta_2 = 1$, at that point we have

$$g(\xi) + j(\xi) = 1, \quad h(\xi) + j(\xi) = 1, \tag{5.25}$$

Through Eqs. $(26 - 28)$, we obtain the following equation

$$\frac{1}{Sc}g'' + fg' - 2K_h g(1-g)^2 = 0, \tag{5.26}$$

with corresponding boundary conditions

$$g'(\xi) = K_s g(\xi), \quad at \ \xi = 0, g(\xi) \to 1, \quad as \ \xi \to \infty. \tag{5.27}$$

At the walls, the parameters of engineering interest, i.e., the friction drag and rate of heat transfer are

$$C_f = \frac{2\tau_w}{\rho U_w^2}, \quad \tau_w = \mu \frac{\partial u}{\partial y}\bigg|_{y=0}, \quad Nu_x = \frac{xq_w}{kT_c}, \quad q_w = k\frac{\partial T}{\partial y}\bigg|_{y=0}. \tag{5.28}$$

In above physical parameters of engineering interest, τ_w and q_w are respectively symbolizes the wall shear stress and heat flux, we finally achieved the following non-dimensional equations

$$\frac{Re^{1/2}}{2}C_f = f''(0), \quad Re^{-1/2}Nu_x = -\delta_h\left(1 + \frac{1}{\theta_1(0) + \eta^2\theta_2(0)}\right). \tag{5.29}$$

5.3.1 Optimal homotopy analysis method

The present system of equations are solved by utilizing the optimal HAM and BVPh2-midpoint method. This technique is free of large/small physical parameters. Optimal HAM [96,97] is different from all other previous procedures, it gives the convergence of series solution in a simple way. In the present analysis, optimal HAM is proposed to depict the solution of the problem. The corresponding linear operators and initial guesses are

$$L_f(f) = \frac{d^3 f}{d\xi^3} + \frac{d^2 f}{d\xi^2}, \quad L_{\theta_1}(\theta_1) = \frac{d^2\theta_1}{d\xi^2} - \theta_1,$$

$$L_{\theta_2}(\theta_2) = \frac{d^2\theta_2}{d\xi^2} - \theta_2, \quad L_g(g) = \frac{d^2 g}{d\xi^2} - g, \tag{5.30}$$

$$f_0(\xi) = 1 - exp(-\xi), \quad \theta_{1_0}(\xi) = \frac{\delta_h}{1 - \delta_h}exp(-\xi),$$

$$\theta_{2_0}(\xi) = \xi exp(-\xi), \quad g_0(\xi) = 1 - \frac{K_s}{1 + K_s}exp(-\xi), \tag{5.31}$$

where $L_f(f)$, $L_{\theta_1}(\theta_1)$, $L_{\theta_2}(\theta_2)$, and $L_g(g)$ characterizes the linear operators, and $f_0(\xi)$, $\theta_{1_0}(\xi)$, $\theta_{2_0}(\xi)$, and $g_0(\xi)$ illustrate initial guesses of f, θ_1, θ_2, and g.

5.3.2   Convergence analysis

The physical parameters h_f, h_{θ_1}, h_{θ_2}, and h_g have leading motivation to stabilize the convergence of resulting series solutions. Specified values are assigned to the auxiliary parameters for getting the convergence. In this direction residual errors are obtained for the ferrohydrodynamic equations by implementing the expressions defined in Eqs. (2.26)-(2.28). These expressions are utilized in the evaluation of convergence for the optimal HAM, the resulting convergence and residual errors are listed in tables 6.1 and 6.2. Figure 6.2 reveals the average square residual error for 12th order, Δ_m^t exhibits the total square residual error, defined in Eq. (2.29).
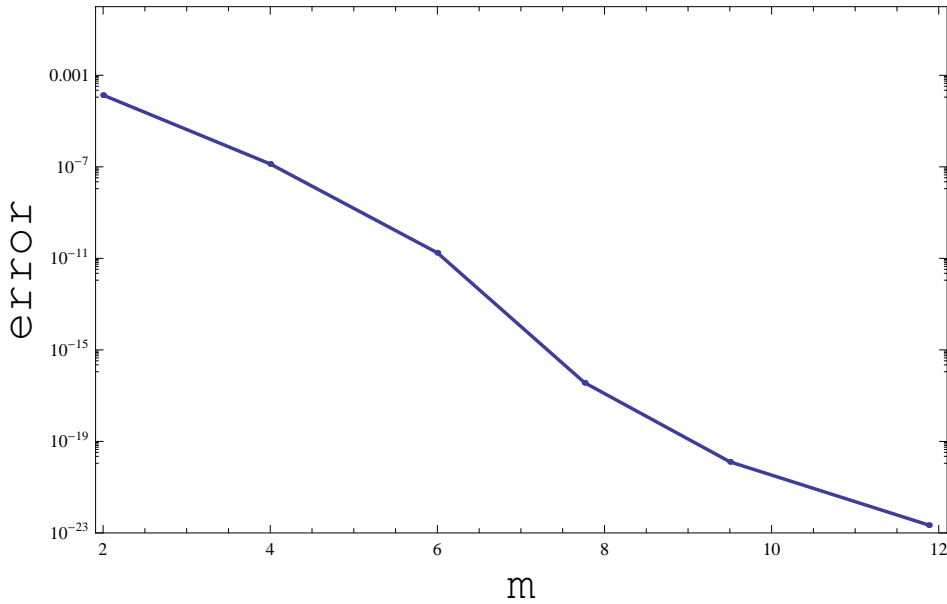
Figure 5.2: Graph for 12th order approximation.

$\frac{values\rightarrow}{order\downarrow}$	h_f	h_{θ_1}	h_{θ_2}	h_g	Δ_m^t
2	-0.72310	-0.49908	-0.53911	-0.29031	0.0000319
4	-0.75990	-0.47140	-0.60330	-0.27190	5.52044×10^{-9}
6	-0.79021	-0.49021	-0.65424	-0.29309	3.51899×10^{-13}
8	-0.87209	-0.63802	-0.67814	-0.46602	4.31766×10^{-17}
10	-0.890226	-0.68310	-0.82031	-0.47031	7.35281×10^{-22}

Table 5.1: Average residual square errors Δ_m^t.

$\frac{values \rightarrow}{order \downarrow}$	$h_f = -0.890226$	$h_{\theta_1} = -0.68310$	$h_{\theta_2} = -0.82031$	$h_g = -0.47031$
8	2.42896×10^{-20}	4.72109×10^{-14}	0.40051×10^{-11}	7.44109×10^{-5}
10	4.11809×10^{-23}	6.33801×10^{-17}	2.49221×10^{-16}	3.50809×10^{-10}
12	5.77199×10^{-29}	3.50921×10^{-20}	6.99216×10^{-19}	1.72097×10^{-14}
20	0.99731×10^{-30}	0.66214×10^{-24}	8.30921×10^{-25}	9.00912×10^{-23}

Table 5.2: Individual residual square errors for Δ_m^f, $\Delta_m^{\theta_1}$, $\Delta_m^{\theta_2}$, and Δ_m^g.

5.4　Discussion

This section concerns the interpretation of materialized parameter on the hybrid chemically reactive species in the viscous ferromagnetic fluid. The characteristics of physical parameters δ_h (Conjugate parameter due to Newtonian heating), β (ferrohydrodynamic interaction), K_h and K_s (strengths of homogeneous and heterogeneous reactions respectively), λ (viscous dissipation), Sc (Schmidt number), δ_c (Curie temperature), Pr (Prandtl number) and γ (dimensionless distance) are on the hybrid chemically reactive species are incorporated. The boundary value problem is analyzed via BVPh2-midpoint method and optimal HAM.

The effect of parameter δ_h (conjugate parameter due to Newtonian heating) on axial velocity and temperature field are exhibited in Figures 5.3 and 5.4. It is portrayed from Figure 5.3 that δ_h (conjugate parameter due to Newtonian heating) decline the axial velocity of fluid. Arising δ_h produces enhancement in heat transfer coefficient, as a result, the resistance between fluid layers enhances, which produces reduction in distribution of velocity. The influence of parameter δ_h (conjugate parameter due to Newtonian heating) on distribution of temperature is interpreted in Figure 5.4. It's obvious that distribution of temperature in hybrid chemically reactive species shows increasing impact by increasing the parameter δ_h. The physical interpretation is that an increment in δ_h leads to rise the heat transfer coefficient h_s, subsequently, the temperature field strengthen. Further, the characteristics of δ_h (conjugate parameter due to Newtonian heating) on concentration field is evident in Figure 5.5. It seems from Figure 5.5 that concentration field declines for larger valves of δ_h. Indeed, Figure 5.5 reveals an increase in conjugate parameter that leads to decelerates the rate of diffusion of hybrid chemical species, as a result, the concentration field reduces thereby enhancing the thickness of concentration boundary layer.

The presence of parameters β (ferrohydrodynamic interaction), γ (dimensionless distance), and ε (Curie temperature) assure the characteristic of magnetic dipole on

the hybrid chemically reactive species. Figures $5.6 - 5.8$ designates the characteristics of ferrohydrodynamic interaction parameter on the axial velocity and temperature field. The axial velocity of hybrid chemically reactive species declines for ferrohydrodynamic parameter evident in Figure 5.6. As β has a direct relation with viscosity in a linear way, thus by enhancing β the hybrid chemically reactive species develop the viscous effect of fluid, subsequently, the velocity field diminish. Further, the enhancement in viscosity leads to arising friction between fluid layers, such enhancement in friction are responsible for the increment in temperature field evident in Figure 5.7. On the other hand, ferrohydrodynamic parameter declines the concentration profile depicted in Figure 5.8. The physical interpretation is that, an increment in β results in the enhancement of viscosity of the hybrid chemically reactive species along the diffusion coefficient, which arise the friction between fluid layers, subsequently, the diffusion of the chemical species reduces.

The characteristics of parameters Sc (Schmidt number), K_h (strength of homogeneous reaction), and K_s (strength of heterogeneous reaction) on the concentration field are determined in Figures $5.9 - 5.11$. The consequence of K_h on the concentration field is evident in Figure 5.9. Concentration field declines for K_h (strength of homogeneous reaction). Whereas, larger values of K_s (strength of heterogeneous reaction) declines the distribution of concentration as evident in Figure 5.10. The concentration boundary layer thickness arise for higher values of K_h and K_s. The physical interpretation is that an enhancement in K_h and K_s leads to reduce the diffusion coefficients of hybrid chemically reactive species, as a result, the concentration field reduces, whereas, their concentration boundary layer thickness enhances. The impacts of Sc (Schmidt number) on distribution of concentration is characterized in Figure 5.11. The higher values of Sc (Schmidt number) improves the concentration field exhibited in Figure 5.11, whereas, the concentration boundary layer decline for Sc (Schmidt number). Physically, as Sc (Schmidt number) is proportional to momentum and mass diffusivity ratio in a linear way, thus $Sc > 1.0$ means that momentum diffusivity is greater than mass diffusivity, $Sc = 1.0$ means that momentum diffusivity is equal to mass diffusivity, and $Sc < 1.0$ means that mass diffusivity is greater than momentum diffusivity. In all these mentioned cases the concentration field arises whereas, the concentration boundary layer thickness reduces.

The influence of Curie temperature on the concentration field is evident in Figure 5.12. The temperature field and its corresponding thermal boundary layer thickness arises for Curie temperature ε portrayed in Figure 5.12. Larger values of Curie temperature leads to higher ambient temperature, appropriately, the temperature field

enhances. As the Curie temperature is different for different particles, thus when Curie temperature parameter is arises it means the fluid have higher ability of absorbing heat, therefore enhancement is observed in Figure 5.12.
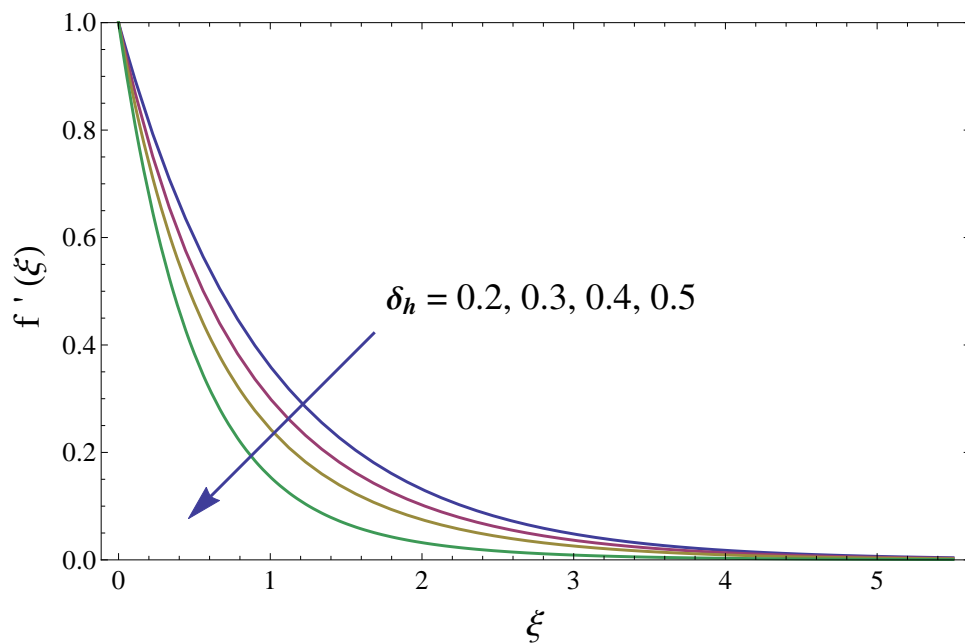
Figure 5.3: The consequence of parameter δ_h (conjugate) on axial velocity.
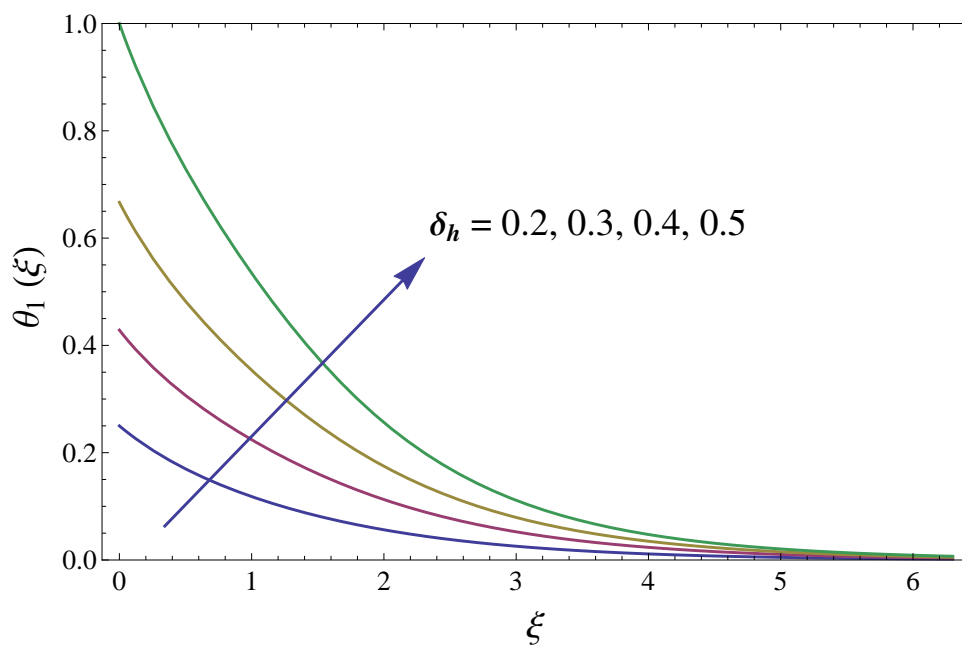
Figure 5.4: The consequence of parameter δ_h (conjugate) on temperature field.
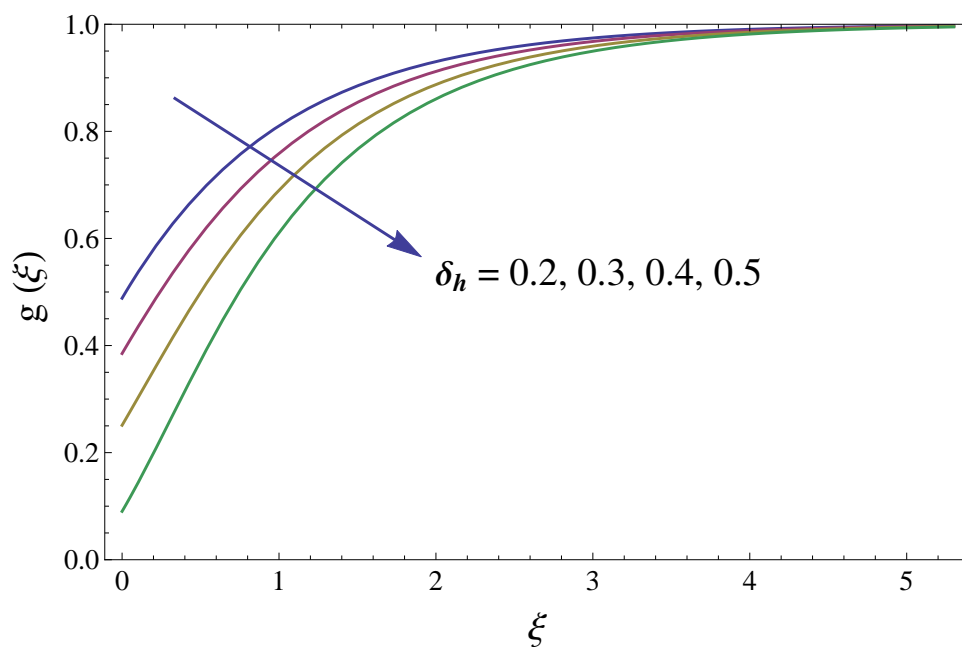
Figure 5.5: The effect of parameter δ_h (conjugate) on concentration field.
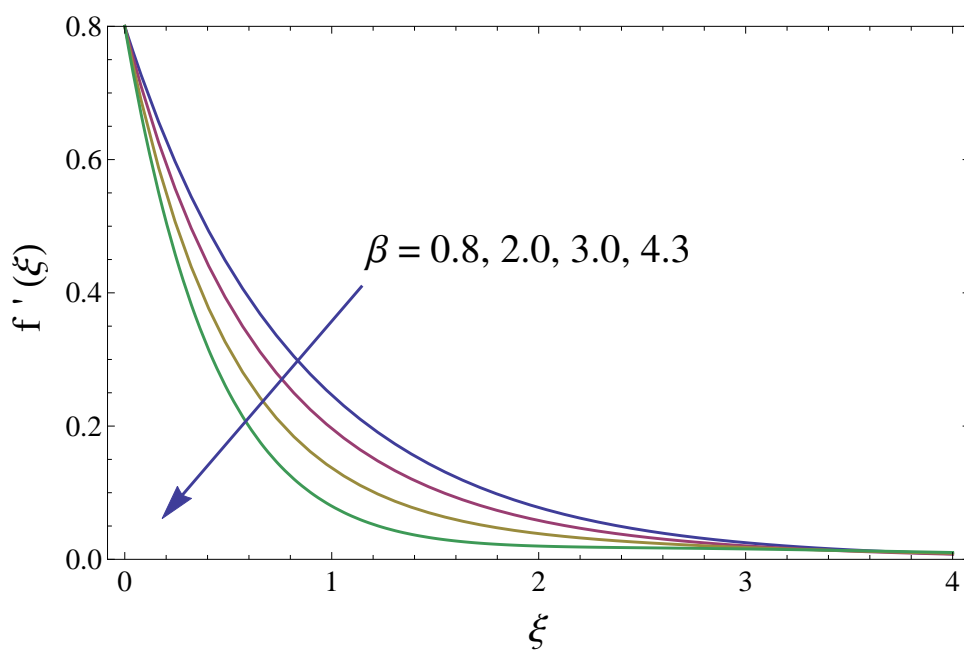
Figure 5.6: The consequence of parameter β (ferrohydrodynamic interaction) on velocity field.
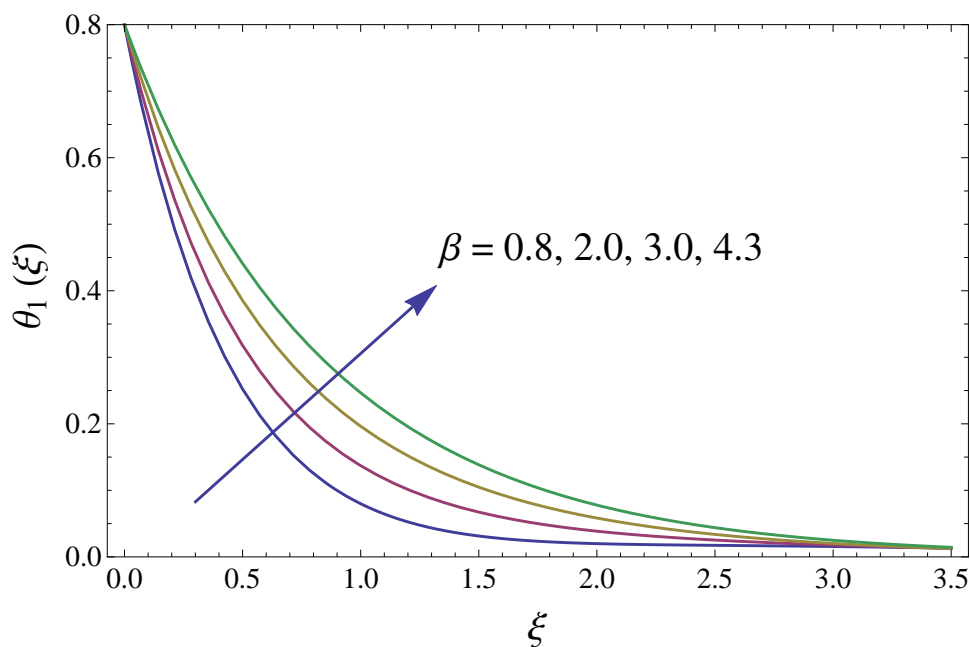
Figure 5.7: The effect of parameter β (ferrohydrodynamic interaction) on temperature field.
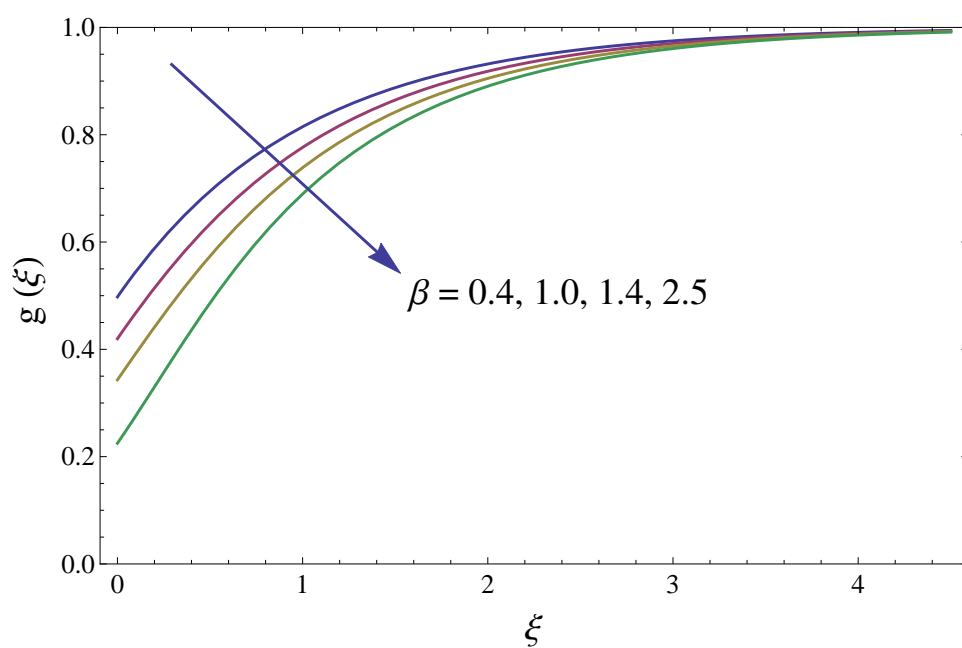
Figure 5.8: The consequence of parameter β (ferrohydrodynamic interaction) on concentration field.
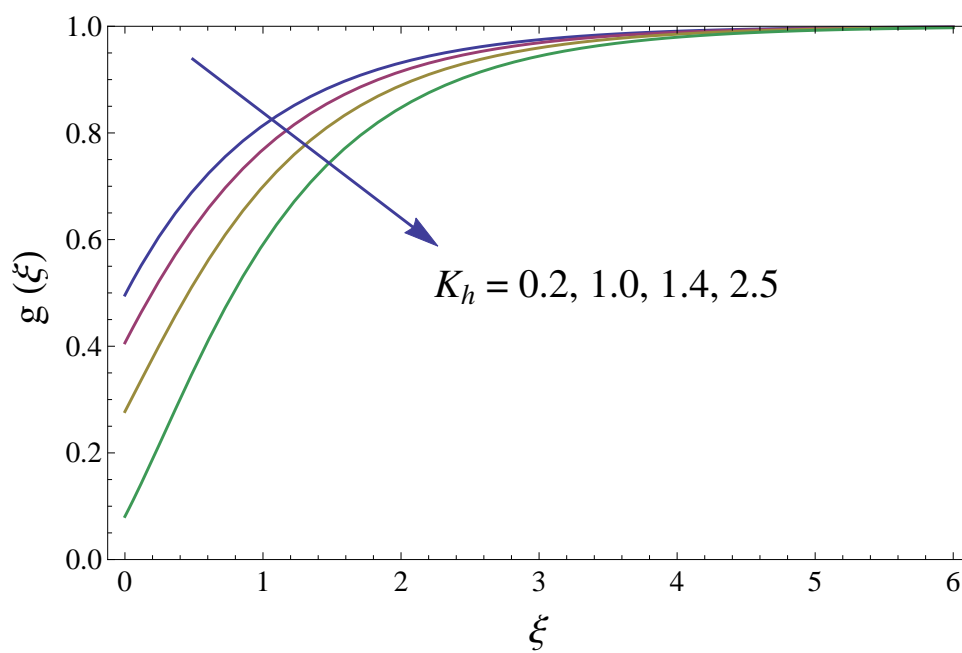
Figure 5.9: Effect of K_h (strength of homogeneous reaction) on $g(\xi)$.
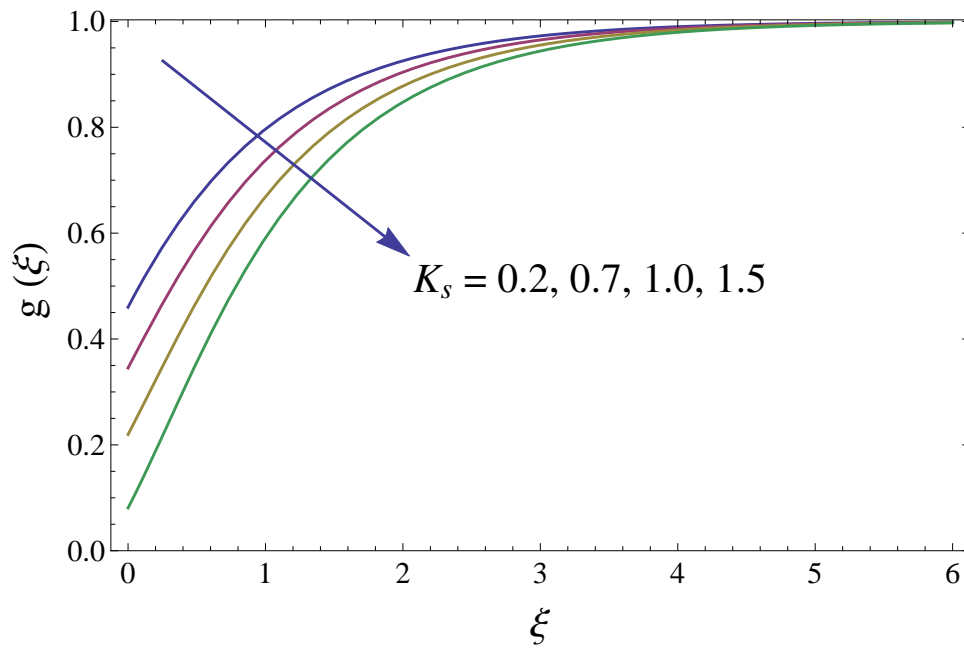
Figure 5.10: Consequence of K_s (strength of heterogeneous reaction) on $g(\xi)$.
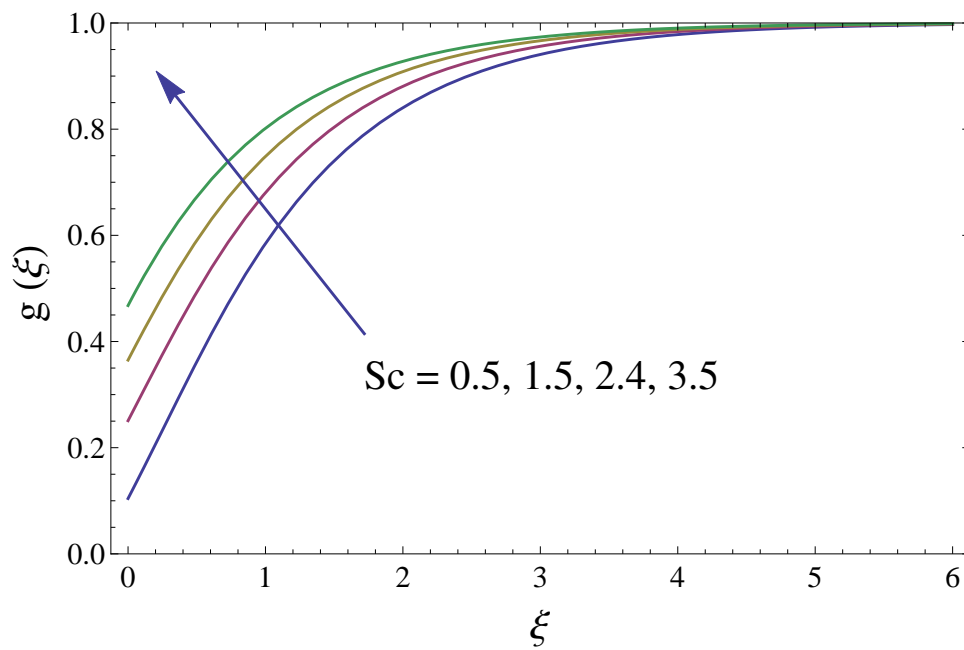
Figure 5.11: Influence of Sc (Schmidt number) on concentration field $g(\xi)$.
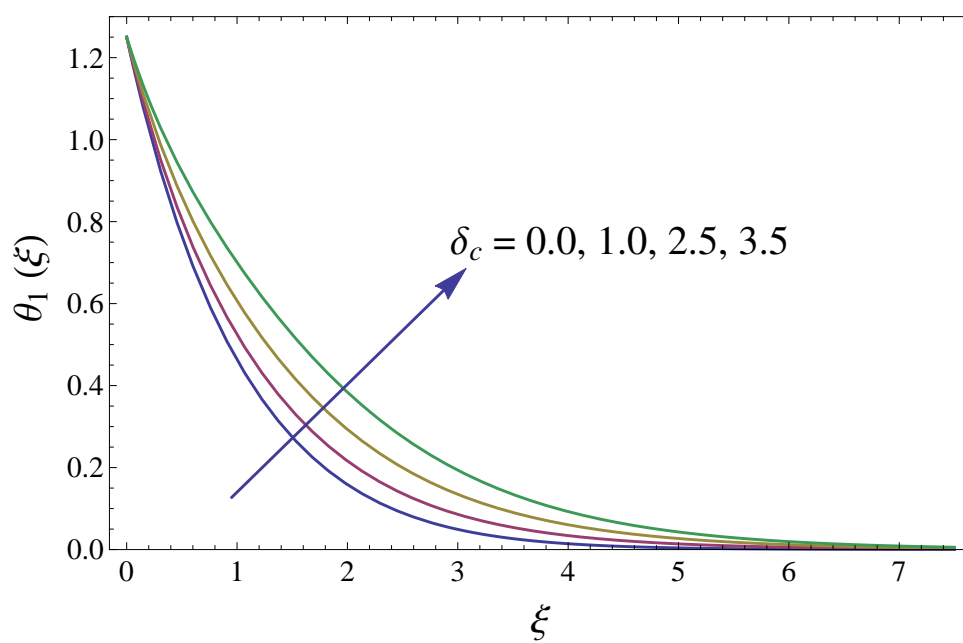
Figure 5.12: Impact of δ_c (Curie temperature) on temperature field.

5.4.1   Physical parameters of engineering interest

This section concerns the results of physical parameters of engineering interest. These materialized parameters are given in Eqs. (5.28) and (5.29). The aim of this section is to scrutinize the impacts of three different chemical species on the rate of heat transfer and friction drag, which are useful in the advanced technological processes. The friction drag via δ_c (conjugate parameter due to Newtonian heating) for different values β (ferrohydodynamic parameter) is portrayed in Figure 5.13. It is observed that the ferrohydrodynamic interaction parameter enhance the friction drag of the hybrid chemically reactive species. On the other hand, the friction drag declines for the Sc (Schmidt number) shown in Figure 5.14. Further, the impacts of conjugate parameter δ_c on the heat transfer rate via β (ferrohydrodynamic) in the flow of a hybrid chemically reactive species is depicted in Figure 5.15. It is characterized that heat transfer rate enhances for conjugate parameter δ_c. Whereas, An enhancement in rate of heat transfer via Pr (Prandtl number) and conjugate parameter δ_c are designated in Figure 5.16. The physical parameters of engineering interest and its impacts on the present flow problem is depicted in Tables 5.3 and 5.4.
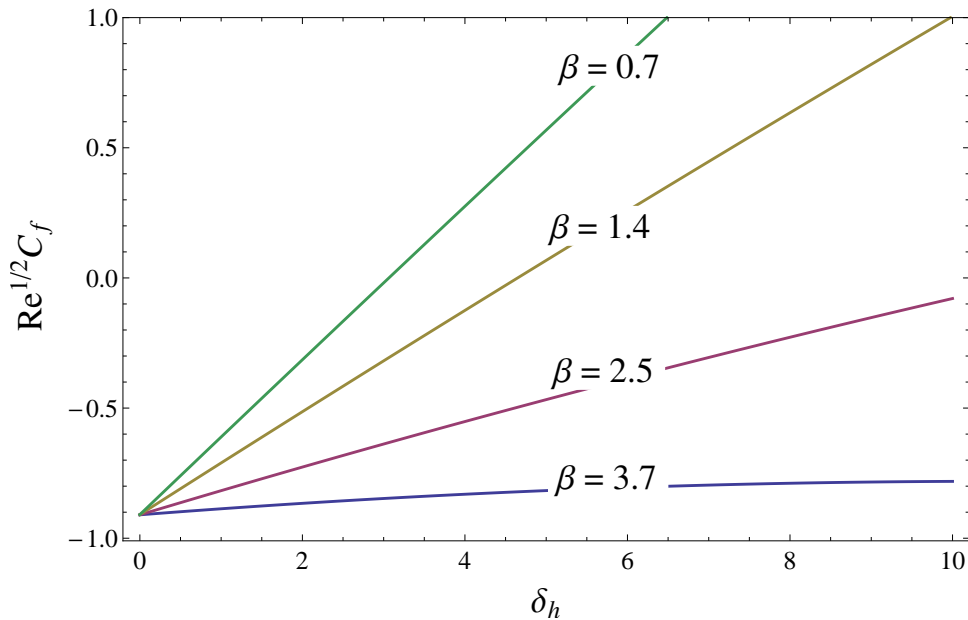
Figure 5.13: Friction drag via δ_h.
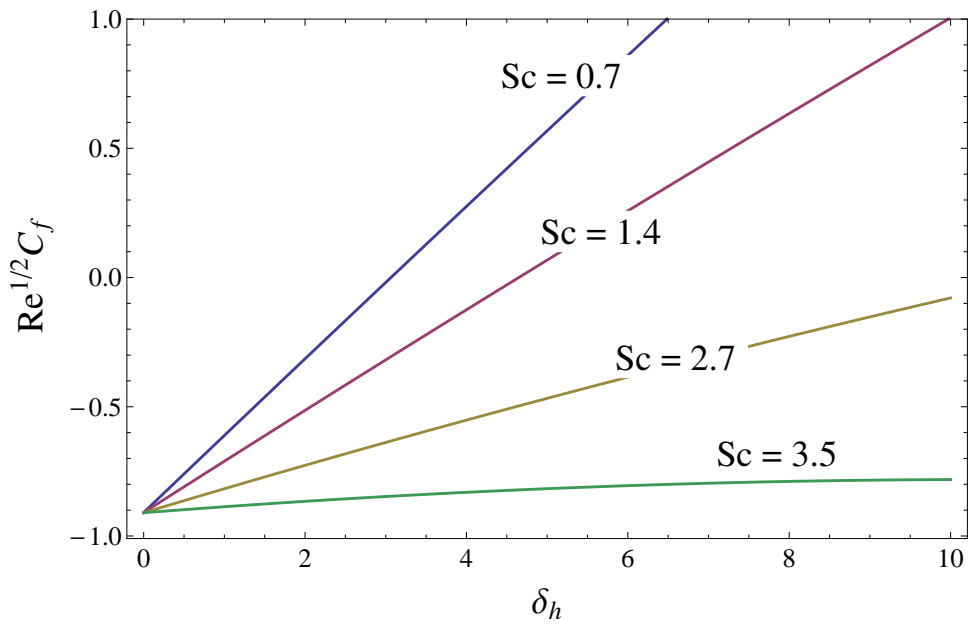
Figure 5.14: Wall shear stress versus δ_h.
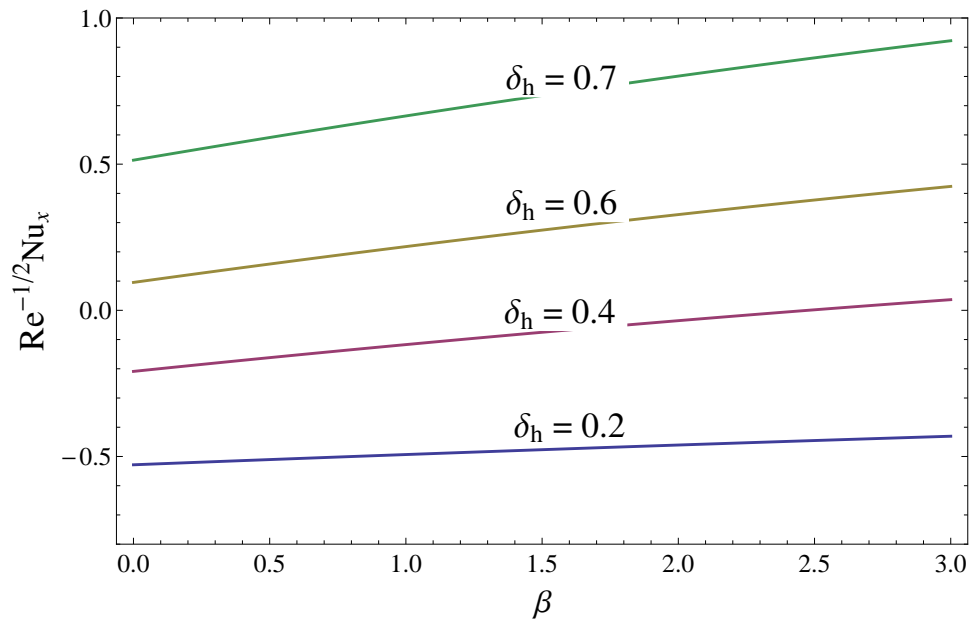
Figure 5.15: Heat transfer rate via β (ferrohydrodynamic interaction parameter).
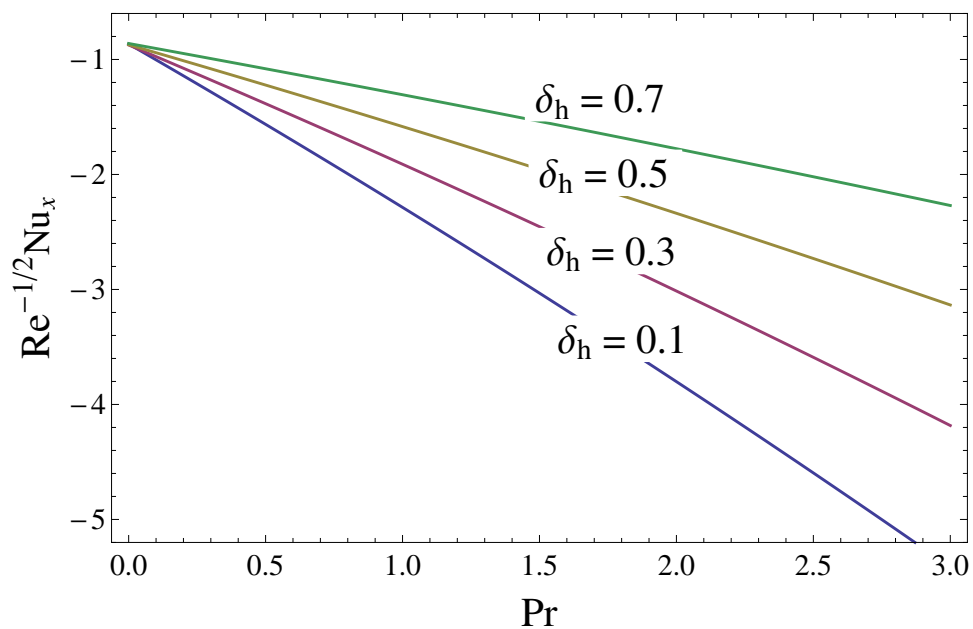
Figure 5.16: Heat transfer rate via Pr (Prandtl number).

Pr	Chen et al. [93]	$\text{Re}_x^{-1/2}\,\text{Nu}_x$ (Optimal HAM)	$\text{Re}_x^{-1/2}\,\text{Nu}_x$ (BVPh2-Midpoint)
0.74	$---$	0.482091	0.4820967
1.0	0.5184	0.513491	0.5134405
1.3	0.6246	0.598403	0.5984381
1.9	0.6870	0.631318	0.6313702
4.0	$---$	0.889504	0.8895382
10.0	$---$	$---$	1.8002127

Table 5.3: Comparison of Nusselt number.

Pr	Sc	β	λ_1	$\mathrm{Re}_x^{1/2}\,\mathrm{C}_f$ (Optimal HAM)	$\mathrm{Re}_x^{1/2}\,\mathrm{C}_f$ (BVPh2-Midpoint)
3.0	1.2	1.5	0.3	1.48031	1.480322
3.5				1.46416	1.464137
4.5				1.30295	1.302969
3.0	1.2	1.5	0.3	1.48031	1.480322
	1.5			1.30052	1.300951
	2.0			1.21052	1.210570
3.0	1.2	1.5	0.3	1.48031	1.480322
		1.8		1.49372	1.493739
		2.0		1.65091	1.650963
3.0	1.2	1.5	0.3	1.48031	1.480322
			0.5	1.34271	1.342738
			0.7	0.50641	0.506447

Table 5.4: Friction drag for distinct values of Pr, β, Sc, and δ_h are classified and compared by means of analytic solution based on optimal HAM and BVPh2-midpoint method.

Concluding remarks

The present work concentrates on the heat transfer rate and friction drag in a hybrid chemically reactive species. The analysis is carried out for three different chemical species. Mass flux is evaluated by Fick's law. The phenomena of Newtonian heating and magnetic dipole are further considered. The main points of the analysis are following.

- The conjugate parameter enhances the temperature field thereby declines the axial velocity and concentration field.

- The axial velocity and concentration field of hybrid chemically reactive species decline for ferrohydrodynamic parameter, thereby enhances the temperature filed.

- The strength of homogeneous reaction K_h results in the reduction of concentration field.

- The heterogeneous reaction strength K_s declines the concentration field.

- The Schmidt number improves the concentration field.

- The friction drag via conjugate parameter δ_h are depicted.

- The heat transfer rate via ferrohydrodynamic and Prandtl number are scrutinized.

Chapter 6

Ferrite nanoparticles $MnZnFe_2O_4$, Fe_3O_4 and $NiZnFe_2O_4$ in flow of ferromagnetic nanofluid

6.1   Introduction

The intention of present chapter is to theoretically exhibit the practicability of the concept of ferromagnetic nanoparticles with Fe$_3$O$_4$ (magnetite ferrite), NiZnFe$_2$O$_4$ (nickel zinc ferrite), and MnZnFe$_2$O$_4$ (manganese zinc ferrite) as ferrites nanoparticles and C$_2$H$_6$O$_2$ (ethylene glycol) as a base fluid. The analysis centralizes on depicting the heat transport phenomenon in the ferromagnetic nanofluids. A comparison has been made for different ferrites nanoparticles in the analysis of axial velocity, temperature field, wall shear stress, and heat transfer rate. The constitutive equations for velocity and temperature are given under the boundary layer assumptions. In the wake of utilizing appropriate similarity variables, the final form of the boundary value problem is clarified as a consequence of the BVPh2-midpoint technique and analytically with optimal homotopy analysis method (optimal HAM). The physical emerging parameters are portrayed by virtue of graphs.

6.2   Ferrohydrodynamic and thermal energy equations

Consider an electrically non-conducting, incompressible, steady, and laminar viscous boundary layer flow of a ferromagnetic NiZnFe$_2$O$_4$-C$_2$H$_6$O$_2$, MnZnFe$_2$O$_4$-C$_2$H$_6$O$_2$, and Fe$_3$O$_4$-C$_2$H$_6$O$_2$ nanofluids over a continuously stretching sheet. The effect of the magnetic dipole is taken in this pattern that its center exactly lies on the $y-$axis distant d from the $x-$axis. The nanofluid flow is induced, in behalf of stretching of the surface. The temperatures at the stretching sheet and ambient fluid are $T = T_w$ and $T = T_\infty$. The magnetic field points of the magnetic dipole are applied in positive $x-$direction. The schematic system for the flow evaluation is delineated in Figure 6.1. To make ferrofluid saturate, the magnetic dipole improves the magnetic field by significant strength. The Curie temperature T_c is presumed to be greater than wall temperature T_w, while, the temperature $T = T_\infty$ is supposed to be fluid temperature, where $T_\infty < T_w < T_c$. The fluid above Curie temperature is inadequate of magnetization. The nanoparticles along base fluid are in thermal equilibrium is hypothesized. Taking into consideration the assumptions suggested above, employing the boundary layer approximation, the equation of ferrohydrodynamic and energy

$$\frac{\partial u}{\partial x} + \frac{\partial v}{\partial y} = 0, \tag{6.1}$$

$$\rho_{nf}\left(u\frac{\partial u}{\partial x}+v\frac{\partial u}{\partial y}\right)=-\frac{\partial P}{\partial x}+M\mu_0\frac{\partial H}{\partial x}+\mu_{nf}\frac{\partial^2 u}{\partial y^2}, \tag{6.2}$$

$$(\rho c_p)_{nf}\left(u\frac{\partial T}{\partial x}+v\frac{\partial T}{\partial y}\right)-\mu_0 K_p T\left(u\frac{\partial H}{\partial x}+v\frac{\partial H}{\partial y}\right)=k_{nf}\frac{\partial^2 T}{\partial y^2}. \tag{6.3}$$

Here μ_{nf} signify the dynamic viscosity of nanofluid, ρ_{nf} displays for nanofluid density, $(\rho c_p)_{nf}$ represents the specific heat, whereas k_{nf} exemplify thermal conductivity, the assumed admissible boundary conditions are

$$u|_{y=0}=U_w(x)=Sx,\, v|_{y=0}=0,\, T|_{y=0}=T_w, \tag{6.4}$$

$$u|_{y\to\infty}\to 0,\, T|_{y\to\infty}\to T_c. \tag{6.5}$$

In Eqs. (6.4) and (6.5) the temperature condition recommended at $y=0$ and $y\to\infty$ describe the wall and Curie temperature at the boundaries, T_∞ signify temperature of ambient fluid.

6.3   Thermo-physical properties of $\mathbf{NiZnFe_2O_4}$-$\mathbf{C_2H_6O_2}$, $\mathbf{MnZnFe_2O_4}$-$\mathbf{C_2H_6O_2}$, and $\mathbf{Fe_2O_4}$-$\mathbf{C_2H_6O_2}$

Expressions for μ_{nf} (dynamic viscosity), $(\rho c_p)_{nf}$ (specific heat or heat capacitance), ρ_{nf} (effective dynamic density), and k_{nf} (thermal conductivity) are stated for the nanofluid as

$$\begin{aligned} \frac{\mu_{nf}}{\mu_f}&=\frac{1}{(1-\varphi)^{25/10}};\rho_{nf}=\varphi\rho_s+\rho_f(1-\varphi)\\ (\rho c_p)_{nf}&=(\rho c_p)_s\varphi+(\rho c_p)_f(1-\varphi),\\ \frac{k_{nf}}{k_f}&=\frac{(2k_f+k_s)-2\varphi(k_f-k_s)}{(2k_f+k_s)+\varphi(k_f-k_s)}. \end{aligned} \tag{6.6}$$

Eq. (6.6) shows the general expressions used to compute the specific heat, density, dynamic viscosity, and thermal conductivity for nanofluids. Thermo-physical properties of ferrite nanoparticles are tabulated in table 6.1.

	$\rho(\text{kg/m}^3)$	$C_p(\text{J/kgK})$	$k(\text{W/mK})$	Pr
Ethylene glycol C$_2$H$_6$O$_2$	1116.6	2382	0.249	204
Nickel zinc ferrite NiZnFe$_2$O$_4$	4800	710	6.3	—
Manganese zinc ferrite MnZnFe$_2$O$_4$	4700	1050	3.9	—
Magnetite ferrite Fe$_3$O$_4$	5180	670	9.7	—

Table 6.1: Thermo-physical properties of manganese zinc ferrite, ethylene glycol, Nickel zinc ferrite, and magnetite ferrite.
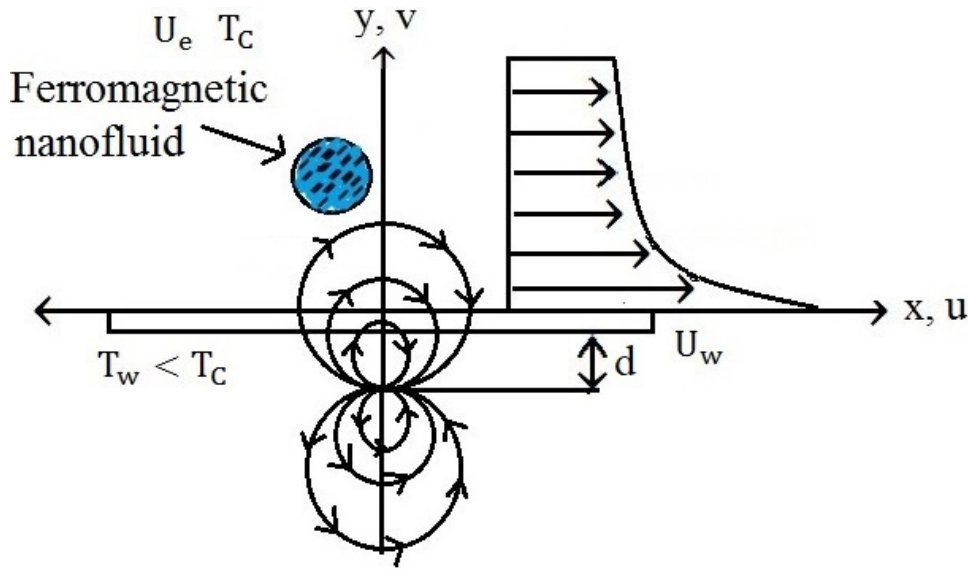
Figure 6.1: Geometery of the flow.

6.4   Solution procedure

The assumed dimensionless variables are

$$\psi(\eta, \xi) = \eta(\frac{\mu_f}{\rho_f})f(\xi), \quad \theta(\xi, \eta) \equiv \frac{T_c - T}{T_w - T_c} = \theta_1(\xi) + \eta^2\theta_2(\xi). \tag{6.7}$$

Where $\theta_2(\xi)$ and $\theta_1(\xi)$ exhibit dimensionless temperature, the corresponding dimensionless coordinates are

$$\xi = y\sqrt{\frac{\rho_f S}{\mu_f}}, \quad \eta = x\sqrt{\frac{\rho_f S}{\mu_f}}. \tag{6.8}$$

The stream function is interpreted in this fashion that the mass equation satisfies directly, here the $\psi(\eta, \xi)$ signifies the stream function, (u, v) symbolizes the comparable

components of velocity defined below

$$u = \frac{\partial \psi(\eta, \xi)}{\partial y} = Sxf'(\xi), \quad v = -\frac{\partial \psi(\eta, \xi)}{\partial x} = -\sqrt{\frac{S\mu_f}{\rho_f}}f(\xi), \tag{6.9}$$

where prime expresses differentiation with respect to ξ and η. Employing the similarity transformations given in Eqs. (2.6)-(2.12) and (6.7) to (6.9), Eqs. (6.2) and (6.3) along Eqs. (6.4) and (6.5) reduce to the system of boundary value problem

$$\frac{1}{(1-\varphi)^{25/10}(1-\varphi+\varphi\frac{\rho_s}{\rho_f})}f''' - f'^2 + ff'' - \frac{2\beta\theta_1}{(1-\varphi+\varphi\frac{\rho_s}{\rho_f})(\xi+\gamma)^4} = 0, \tag{6.10}$$

$$\frac{k_{nf}/k_f}{(1-\varphi+\varphi\frac{(\rho c_p)_s}{(\rho c_p)_f})}\theta_1'' + Prf\theta_1' + \frac{2\lambda\beta\ f(\theta_1-\varepsilon)}{(\xi+\gamma)^3} + 2\theta_2 - 4\lambda f'^2 = 0, \tag{6.11}$$

$$\frac{k_{nf}/k_f}{(1-\varphi+\varphi\frac{(\rho c_p)_s}{(\rho c_p)_f})}\theta_2'' - Pr(2f'\theta_2 - f\theta_2') + \frac{2\lambda\beta\ f\theta_2}{(\xi+\gamma)^3} - 4\lambda f''^2$$

$$+ 2\beta\lambda\ (\varepsilon - \theta_1)\left(\frac{f'}{(\xi+\gamma)^4} + \frac{2f}{(\xi+\gamma)^5}\right) = 0, \tag{6.12}$$

$$f(\xi) = 0, f'(\xi) = 1, \theta_1(\xi) = 1, \theta_2(\xi) = 0, \quad at\ \xi = 0, \tag{6.13}$$

$$f'(\xi) \to 0, \theta_1(\xi) \to 0, \theta_2(\xi) \to 0, \quad when\ \xi \to \infty. \tag{6.14}$$

In above system of nonlinear equations, the parameters β (ferrohydrodynamic interaction), λ (viscous dissipation), Pr (Prandtl number), and ε (Curie temperature) are defined as

$$\varepsilon = \frac{T_c}{T_w - T_c}, \beta = \frac{\gamma_1}{2\pi}\frac{\mu_0 K_p(T_w - T_c)\rho}{\mu^2},$$

$$Pr = \frac{\nu}{\alpha}, \lambda = \frac{S\mu^2}{\rho K_p(T_w - T_c)}, \gamma = \sqrt{\frac{S\rho d^2}{\mu}}. \tag{6.15}$$

At the walls, the parameters of engineering interest, i.e., the friction drag and rate of transfer of heat are

$$C_f = \frac{2\tau_w}{\rho U_w^2}, \quad \tau_w = \mu\frac{\partial u}{\partial y}\Big|_{y=0},$$

$$Nu_x = \frac{x}{T_w - T_c}\frac{\partial T}{\partial y}\Big|_{y=0}. \tag{6.16}$$

We finally achieved the following dimensionless equations for friction drag and Nusselt number, i.e., local surface heat flux

$$\frac{1}{2}Re^{1/2}C_f = \frac{1}{(1-\varphi)^{-25/10}}f''(0),$$

$$Re^{-1/2}Nu_x = -\frac{k_{nf}}{k_f}(\theta_1'(0) + \eta^2\theta_2'(0)). \tag{6.17}$$

where $Re_x = \frac{xU_w(x)}{\nu_f} = \frac{Sx^2}{\nu_f}$ signify local Reynolds number depends upon the surface stretching velocity $U_w(x)$, $\frac{1}{2}Re^{1/2}C_f$ describes the friction drag, and $Re_x^{-1/2}Nu_x$ symbolizes the local Nusselt number.

6.4.1   Optimal homotopy analysis method

The optimal HAM and BVPh2−Midpoint method (Maple) are implemented in the current problem for series solution of equations (6.10), (6.11) and (6.12) along the permitted boundary conditions defined in Eqs. (6.13) and (6.14). These techniques are utilized to get the solutions for highly non-linear equations. The optimal HAM [96,97] gives better results compared with perturbation techniques and other conventional investigative techniques. Firstly, the optimal HAM gives us a remarkable flexibility to pick the equation type of linear sub-problems. Secondly, the optimal HAM works regardless of the possibility that there do not exist any large/small consequential parameters in determining equations and boundary/initial conditions. Particularly, unlike perturbation and alternative analytic techniques, the optimal HAM gives us an advantageous approach to insure the convergence of solution by presenting the supposed convergence control parameter into the series solution. In evaluation of problem, one needs the linear operators and initial guesses which are given below for the under discussion problem.

$$L_f(f) = \frac{d^3 f}{d\xi^3} + \frac{d^2 f}{d\xi^2}, L_{\theta_1}(\theta_1) = \frac{d^2\theta_1}{d\xi^2} - \theta_1,$$
$$L_{\theta_2}(\theta_2) = \frac{d^2\theta_2}{d\xi^2} - \theta_2. \tag{6.18}$$

$$f_0(\xi) = 1 - exp(-\xi), \theta_{1_0}(\xi) = exp(-\xi),$$
$$\theta_{2_0}(\xi) = \xi exp(-\xi), \tag{6.19}$$

where $L_f(f)$, $L_{\theta_1}(\theta_1)$, and $L_{\theta_2}(\theta_2)$ symbolizes the linear operators, while $f_0(\xi)$, $\theta_{1_0}(\xi)$ and $\theta_{2_0}(\xi)$ illustrate initial guesses of f, θ_1, and θ_2.

6.4.2   Convergence analysis of optimal HAM solution

The auxiliary parameters h_f, h_{θ_1}, and h_{θ_2} have a leading purpose in controlling the convergence of the solution. To get a convergent analytic solutions, preferred values are assigns to h_f, h_{θ_1}, and h_{θ_2}. For this reason, residual errors are observed for

ferrohydrodynamic equations by implementing the expressions defined in Eqs. (2.26)-(2.28). These expressions are utilized in the evaluation of convergence for the optimal HAM, the resulting convergence and residual errors are listed in tables 7.2 and 7.3. Figure 7.2 reveals the average square residual error for 10th order. Δ_m^f exhibits the total square residual error, defined in Eq. (2.29).

$\frac{values\rightarrow}{order\downarrow}$	h_f	h_{θ_1}	h_{θ_2}	Δ_m^t
4	-0.77901	-0.52131	-1.00021	0.009324
6	-0.93260	-0.71010	-1.00871	5.32150×10^{-7}
8	-0.99832	-0.88031	-1.09215	0.49321×10^{-13}
10	-1.00131	-0.90043	-1.10032	4.27210×10^{-17}
12	-1.04319	-0.98317	-1.20921	2.73090×10^{-22}

Table 6.2: Average residual square errors Δ_m^t.

$\frac{values\rightarrow}{order\downarrow}$	$h_f = -1.03177$	$h_{\theta_1} = -0.92185$	$h_{\theta_2} = -1.06242$
8	7.70010×10^{-23}	2.42890×10^{-17}	3.54290×10^{-14}
10	1.42103×10^{-25}	4.42879×10^{-20}	7.64431×10^{-15}
12	5.19034×10^{-27}	7.54900×10^{-23}	1.80052×10^{-18}
20	8.32298×10^{-29}	0.87231×10^{-25}	6.53180×10^{-23}

Table 6.3: Individual residual square errors for Δ_m^f, $\Delta_m^{\theta_1}$, and $\Delta_m^{\theta_2}$.
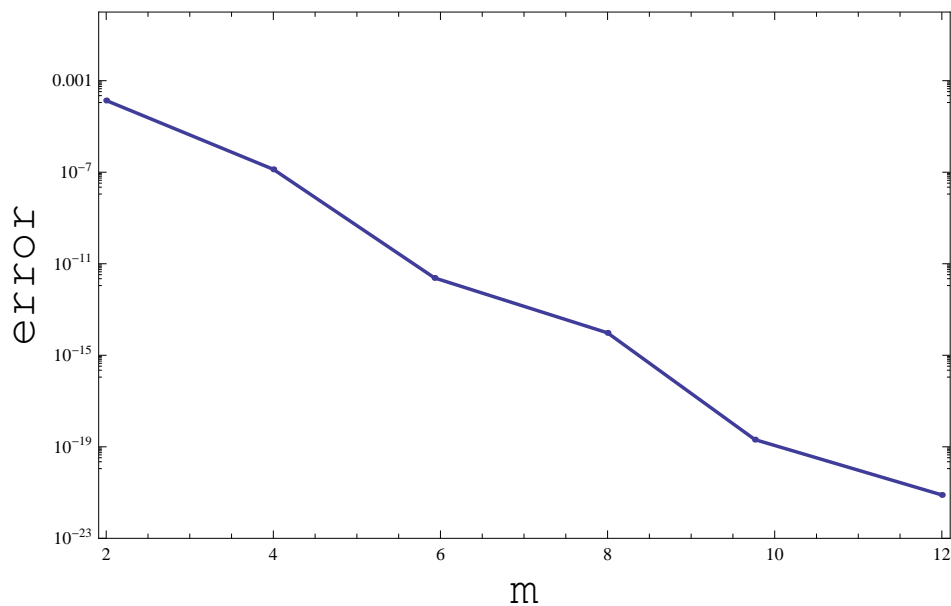
Figure 6.2: Graph for 10th order approximation.

6.5 Discussion

The boundary value problem is determined numerically and analytically via the BVPh2-Midpoint method and optimal (HAM) respectively. This section contains the consequential interpretation of sundry parameters on the flow field. The impacts of dimensionless submerging parameters β (ferrohydrodynamic interaction), λ (viscous dissipation), φ (solid volume fraction), and Pr are evaluated. Moreover, the rest of the materialized parameters in the flow problem are considered as fixed. The established values of these parameters are $\gamma = 1.0$, $\lambda = 0.01$, $\varepsilon = 2.0$. The accuracy of the present optimal HAM and BVPh2$-$midpoint method is confirmed by comparing $Re^{-1/2}Nu_x$ with Rashidi et al. [94] tabulated in table 7.4. The results characterized in table 7.4 are agreed with the present analysis. The ferromagnetic NiZnFe$_2$O$_4$-C$_2$H$_6$O$_2$, MnZnFe$_2$O$_4$-C$_2$H$_6$O$_2$, and Fe$_3$O$_4$-C$_2$H$_6$O$_2$ nanofluids flow with and without nanoparticles are investigated. To realize an obvious insight of present analysis, the results are explored for the friction drag, axial velocity, Nusselt number, and temperature field graphically.

  The impacts of parameter φ on velocity distribution and temperature field of ferromagnetic NiZnFe$_2$O$_4$-C$_2$H$_6$O$_2$, MnZnFe$_2$O$_4$-C$_2$H$_6$O$_2$, and Fe$_3$O$_4$-C$_2$H$_6$O$_2$ nanofluids are evident in Figures 6.3 and 6.4. It is depicted from Figure 6.3 that axial velocity of existing fluid decreases with parameter φ (solid volume fraction of nanofluid).

The axial velocity reduces away from the wall. In fact, enhancement in parameter φ (solid volume fraction of nanofluid) concentrates the ferromagnetic fluid which consequently produces friction to the liquid motion that leads to deteriorate the axial velocity in the presence and absence of magnetic dipole. The presence of the magnetic dipole diminishes the fluid motion compared with the case when magnetic dipole is removed. This means that the magnetic dipole is particularly important in reducing the movements of fluid particles. Further, it is also clear from Figure 6.3 that Fe_3O_4 (magnetite ferrite) particles are more magnetized compared with $NiZnFe_2O_4$ (nickel zinc ferrite) and $MnZnFe_2O_4$ (manganese zinc ferrite) nanoparticles. The more the magnetization, the more the resistance produced by the magnetic dipole to the fluid particles. As a result, Figure 6.3 depicts that Fe_3O_4-$C_2H_6O_2$ ferromagnetic nanofluids have low velocity compared with ferromagnetic $NiZnFe_2O_4$-$C_2H_6O_2$ and $MnZnFe_2O_4$-$C_2H_6O_2$ nanofluids. The impact of parameter φ (solid volume fraction) on temperature field of ferromagnetic $NiZnFe_2O_4$-$C_2H_6O_2$, $MnZnFe_2O_4$-$C_2H_6O_2$, and Fe_3O_4-$C_2H_6O_2$ nanofluids in the presence and absence of magnetic dipole is revealed in Figure 6.4. It is recognized that temperature field of Fe_3O_4-$C_2H_6O_2$ is higher than $NiZnFe_2O_4$-$C_2H_6O_2$ and $MnZnFe_2O_4$-$C_2H_6O_2$ nanofluids in the presence and absence of the magnetic dipole. The physical interpretation is that the thermal conductivity of Fe_3O_4 (magnetite ferrite) nanoparticles is higher than $NiZnFe_2O_4$ (nickel zinc ferrite) and $MnZnFe_2O_4$ (manganese zinc ferrite) nanoparticles. Moreover, the presence of the magnetic dipole makes the temperature field higher if compared to the case when the magnetic dipole is removed. This is by virtue of fact that the magnetic dipole yields more resistance to the Fe_3O_4 (magnetite ferrite) nanoparticles compared with $NiZnFe_2O_4$ (nickel zinc ferrite) and $MnZnFe_2O_4$ (manganese zinc ferrite) nanoparticles, that leads to enhance the temperature field.

The influence of parameter (ferrohydrodynamic interaction) is delineated in Figures 6.5 and 6.6. The existence of parameters γ (dimensionless distance), ε (Curie temperature), and β (ferrohydrodynamic interaction) is essential to hold the impact of ferromagnetic effect on the boundary layer flow. The existence of Fe_3O_4 (magnetite ferrite), $NiZnFe_2O_4$ (nickel zinc ferrite) and $MnZnFe_2O_4$ (manganese zinc ferrite) nanoparticles in a viscous carrier fluid corresponds to ferromagnetic nanofluid, because of which viscosity of liquid enhances and correspondingly the axial velocity reduces for enlarging values of parameter β (ferrohydrodynamic interaction), which is depicted in Figure 6.5. The impact of β (ferrohydrodynamic interaction) on axial velocity is carried out with and without the magnetic dipole. It is recognized that existence of the magnetic dipole reduces the axial velocity rapidly compared to the

case when the magnetic dipole is removed. This is by cause of the fact that magnetic dipole attracts the nanoparticles Fe_3O_4 (magnetite ferrite), $NiZnFe_2O_4$ (nickel zinc ferrite) and $MnZnFe_2O_4$ (manganese zinc ferrite) that coincide to strengthen the viscosity of the nanofluid inside the boundary layer and as a result the axial velocity slows down. The highest velocity is observed for the $C_2H_6O_2$ (ethylene glycol, when $\varphi = 0$) and the lowest axial velocity is observed for the Fe_3O_4-$C_2H_6O_2$ (magnetite ferrite-ethylene glycol, when $\varphi = 0.2$) nanofluids as it is evident in Figure 6.5. Impact of β (ferrohydrodynamic interaction) on the temperature profile is exhibited in Figure 6.6. It is evident that improvement in parameter β (ferrohydrodynamic interaction) lead to enhance the temperature of nanofluid in both cases, i.e., with and without magnetic dipole. This is because of the interaction between an action of a magnetic field and movements of Fe_3O_4 (magnetite ferrite), $NiZnFe_2O_4$ (nickel zinc ferrite) and $MnZnFe_2O_4$ (manganese zinc ferrite) nanoparticles. The interaction between magnetic field action and Fe_3O_4 (magnetite ferrite), $NiZnFe_2O_4$ (nickel zinc ferrite) and $MnZnFe_2O_4$ (manganese zinc ferrite) nanoparticles thinning the axial velocity thereby enhancing heating due to friction among fluid layers, that cause to raise the thermal boundary layer, i.e., the devaluation in movements of Fe_3O_4 (magnetite ferrite), $NiZnFe_2O_4$ (nickel zinc ferrite) and $MnZnFe_2O_4$ (manganese zinc ferrite) nanoparticles contribute in the enhancement of the temperature field.

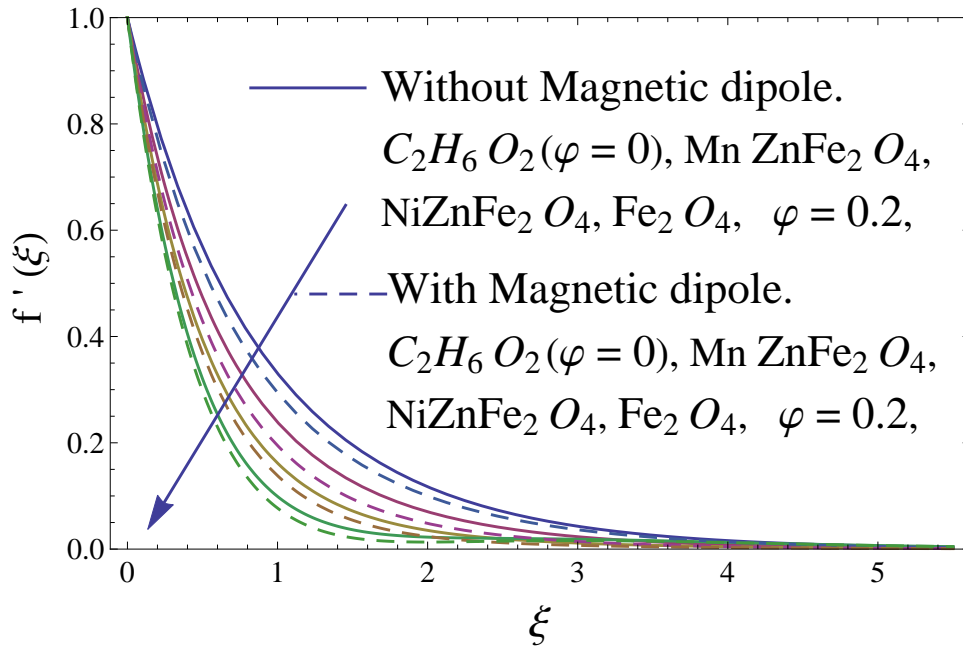Figure 6.3: Comparitive analysis of solid volume fraction φ on axial velocity.
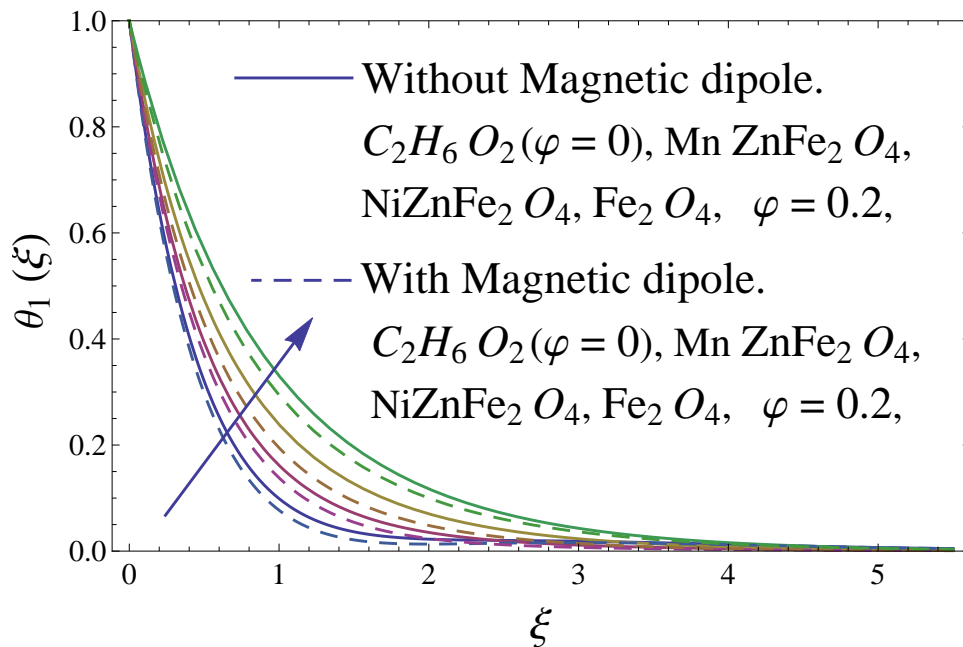

Figure 6.4: Comparitive analysis of solid volume fraction φ on distribution of temperature.
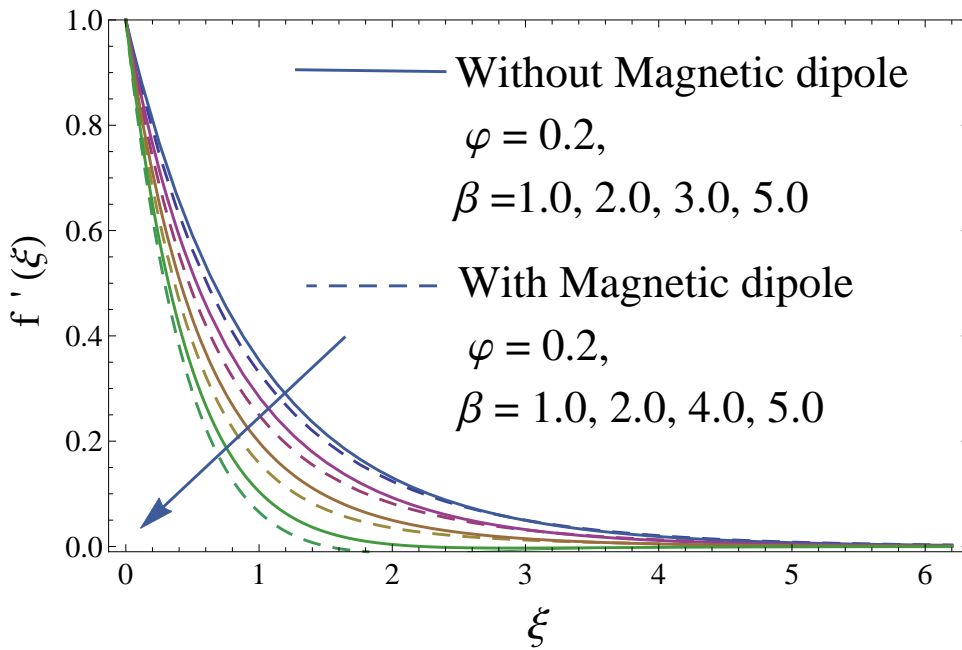
Figure 6.5: Comparitive analysis of parameter β (ferrohydrodynamic interaction) on axial velocity.
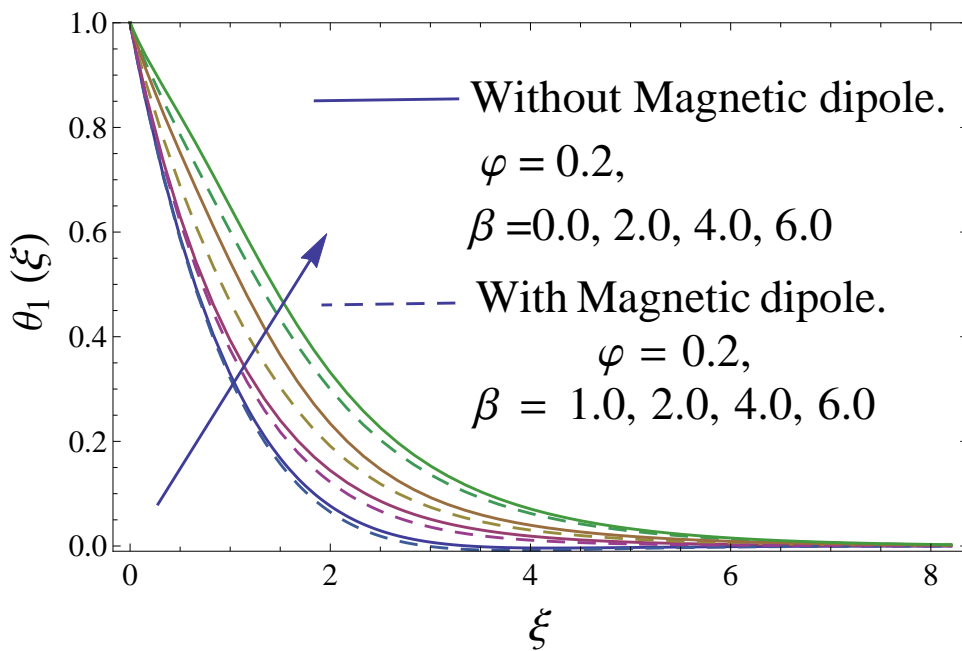

Figure 6.6: Comparitive analysis of parameter β (ferrohydrodynamic interaction) on distribution of temperature.

6.5.1   Parameters of engineering interest

The expressions for friction drag and rate of heat transfer are expressed in Eqs.
(6.16) and (6.17). The impact of parameter φ (solid volume fraction) on wall shear
stress of the ferromagnetic $C_2H_6O_2$-$NiZnFe_2O_4$ (ethylene glycol-nickel zinc ferrite),
$MnZnFe_2O_4$-$C_2H_6O_2$ (manganese zinc ferrite-ethylene glycol) and $C_2H_6O_2$-Fe_3O_4 (ethy-
lene glycol-magnetite ferrite) nanofluids in both cases, i.e., with and without the
magnetic dipole are displayed in Figure 6.7. Reduction is incorporated in the wall
shear stress in presence of the magnetic dipole compared to the case when the mag-
netic dipole is removed. Since we know that the magnetic dipole attracts the Fe_3O_4
(magnetite ferrite), $NiZnFe_2O_4$ (nickel zinc ferrite) and $MnZnFe_2O_4$ (manganese zinc
ferrite) nanoparticles, this results in the enhancement of the viscosity of the nanofluid
inside the boundary layer and yet the wall shear stress increases. The lowest friction
drag is depicted for the $C_2H_6O_2$ (ethylene glycol, when $\varphi = 0$) and the highest friction
drag is observed for the Fe_3O_4-$C_2H_6O_2$ (magnetite ferrite-ethylene glycol, when $\varphi =$
0.2) nanofluids as it is evident in Figure 6.7 and 6.8.

Moreover, φ (solid volume fraction) on wall shear stress of the ferromagnetic
$C_2H_6O_2$-$NiZnFe_2O_4$ (ethylene glycol-nickel zinc ferrite), $MnZnFe_2O_4$-$C_2H_6O_2$ (man-
ganese zinc ferrite-ethylene glycol) and $C_2H_6O_2$-Fe_3O_4 (ethylene glycol-magnetite fer-
rite) nanofluids via heat transfer rate are analyzed in Figures 6.9 and 6.10. It is
scrutinized from Figure 6.9 that the heat transfer rate enhances for ferromagnetic
$C_2H_6O_2$-$NiZnFe_2O_4$ (ethylene glycol-nickel zinc ferrite), $MnZnFe_2O_4$-$C_2H_6O_2$ (man-
ganese zinc ferrite-ethylene glycol) and $C_2H_6O_2$-Fe_3O_4 (ethylene glycol-magnetite fer-
rite) nanofluids in the presence and absence of magnetic dipole. The fast improvement
in rate of heat transfer is perceived along magnetic dipole, instead, from Figure 6.10,
it is evident that an increase in heat transfer rate is depicted for the respective ferro-
magnetic nanofluids. Comparison of the Nusselt number is delineated in Table 6.4.

Pr	Rashidi et al. [94]	$Re_x^{-1/2}$ Nu_x (Optimal HAM)	$Re_x^{-1/2}$ Nu_x (BVPh2-Midpoint)
1.0	1.000000	1.000000	1.000000
3.0	1.923682	1.923690	1.923672
4.0	– – –	2.003170	2.003162
5.0	– – –	2.329810	2.329871
8.0	– – –	– – –	2.541990

Table 6.4: Comparison of Nusselt number.
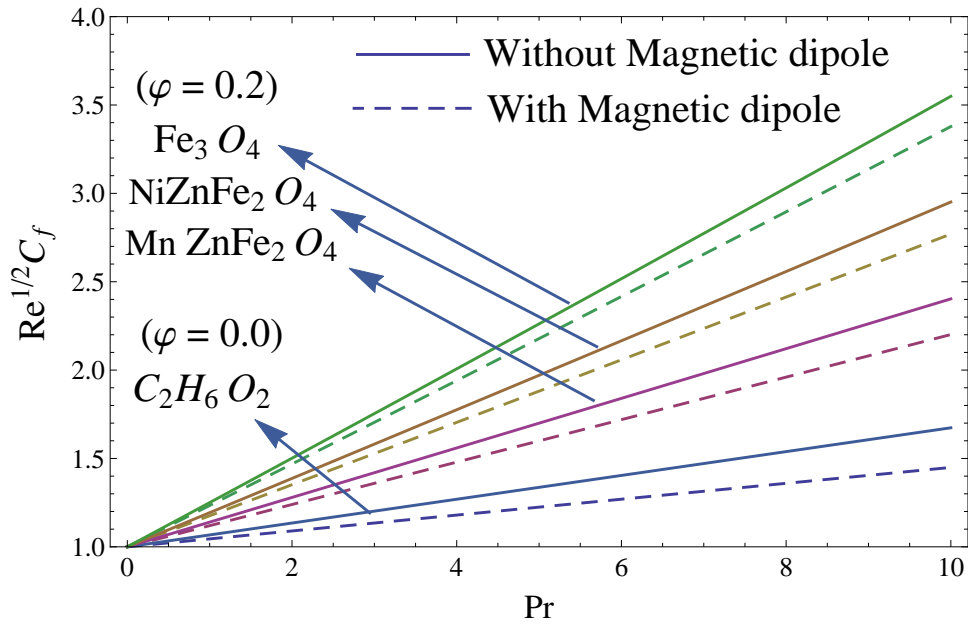
Figure 6.7: Wall shear stress versus Pr.
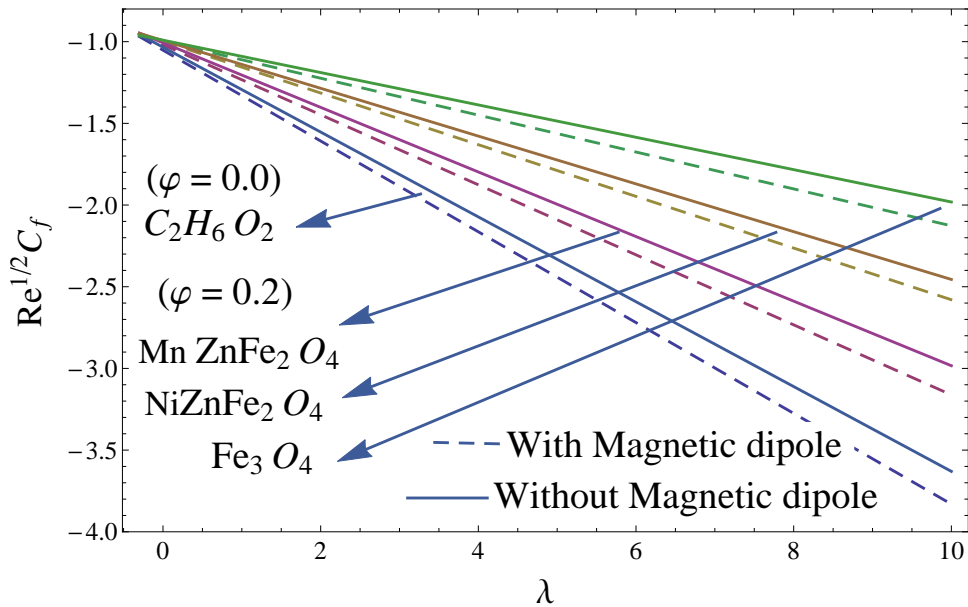
Figure 6.8: Wall shear stress versus λ.
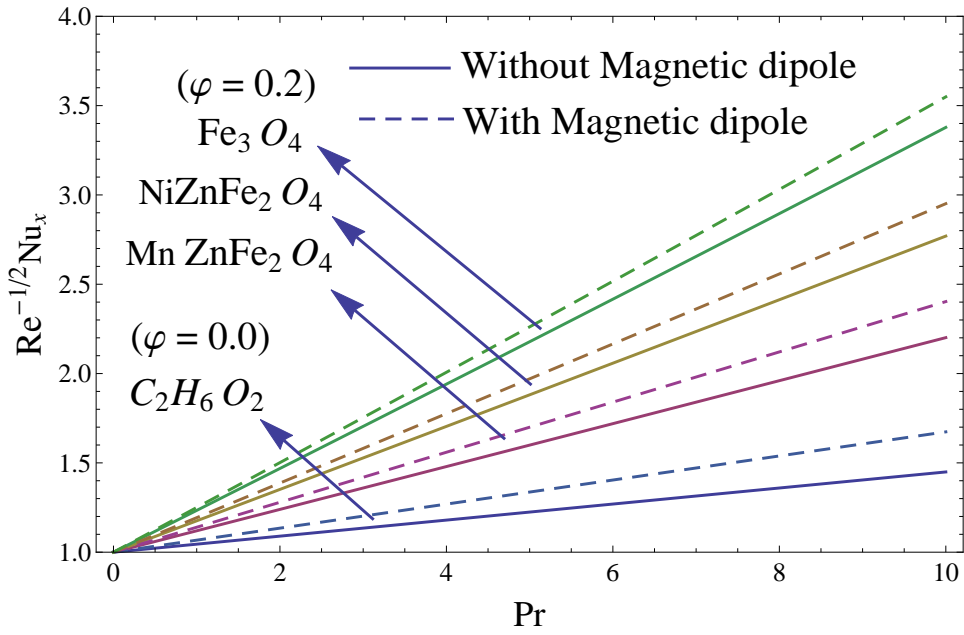
Figure 6.9: Heat transfer rate versus Pr.
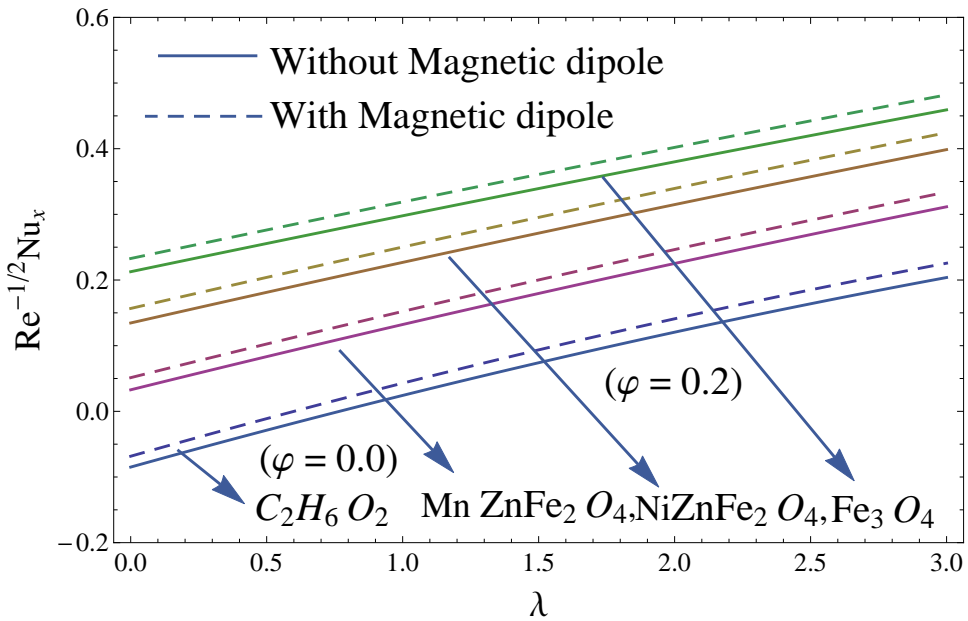
Figure 6.10: Heat transfer rate versus λ.

Concluding remarks

The purpose of this article is to theoretically exhibit the practicability concept of ferromagnetic nanofluids with nickel zinc ferrite (NiZnFe$_2$O$_4$), magnetite ferrite (Fe$_3$O$_4$), and manganese zinc ferrite (MnZnFe$_2$O$_4$) as ferrites nanoparticles and ethylene glycol (C$_2$H$_6$O$_2$) as a base fluid. Heat transfer is depicted in the resulting ferromagnetic nanofluids. The boundary value problem is interpreted numerically and analytically as a consequence of the BVPh2-midpoint method and optimal HAM respectively. The key points of the flow problem are bellow.

- Enlargement in φ (solid volume fraction) consequences in the reduction of axial velocity and enhances the temperature field in the presence of the magnetic dipole.

- Axial velocity reduces and the temperature field enhances swiftly for increasing values of β (ferromagnetic interaction), when the magnetic dipole is present.

- The wall shear stress of the ferromagnetic NiZnFe$_2$O$_4$-C$_2$H$_6$O$_2$, MnZnFe$_2$O$_4$-C$_2$H$_6$O$_2$, and Fe$_3$O$_4$-C$_2$H$_6$O$_2$ nanofluids reduces in the presence and absence of magnetic dipole.

- The fast reduction in the heat transfer rate is observed in the presence of the magnetic dipole.

Chapter 7

Impacts of ferrite nanoparticles in viscous ferromagnetic nanofluid

7.1 Introduction

This chapter conducts the theoretical examination to demonstrate the heat transfer of six distinct ferromagnetic $C_2H_6O_2$-$MnZnFe_2O_4$ (ethylene glycol-manganese zinc ferrite), $NiZnFe_2O_4$-$C_2H_6O_2$ (nickel zinc ferrite-ethylene glycol), $C_2H_6O_2$-Fe_3O_4 (ethylene glycol-magnetite ferrite), H_2O-$NiZnFe_2O_4$ (water-nickel zinc ferrite), H_2O-$MnZnFe_2O_4$ (water-manganese zinc ferrite), and Fe_3O_4-H_2O (magnetite ferrite-water) nanofluids. Heat transport phenomenon in the flow of ferromagnetic nanofluid is characterized. A comparison has been made for different ferrites nanoparticles in the analysis of axial velocity, temperature field, heat transfer rate, and wall shear stress. The constitutive equations for velocity and temperature are taken under the boundary layer assumptions. In the wake of utilizing appropriate similarity variables, the final form of boundary value problem is clarified numerically with BVPh2-midpoint method and analytically with optimal homotopy analysis method (optimal HAM). The physical emerging parameters are portrayed.

7.2 Ferrohydrodynamic and thermal energy equations

Consider an electrically non-conducting, steady, incompressible and laminar viscous boundary layer flow of a ferromagnetic $C_2H_6O_2$-$MnZnFe_2O_4$ (ethylene glycol-manganese zinc ferrite), $NiZnFe_2O_4$-$C_2H_6O_2$ (nickel zinc ferrite-ethylene glycol), $C_2H_6O_2$-Fe_3O_4 (ethylene glycol-magnetite ferrite), H_2O-$NiZnFe_2O_4$ (water-nickel zinc ferrite), H_2O-$MnZnFe_2O_4$ (water-manganese zinc ferrite), and Fe_3O_4-H_2O (magnetite ferrite-water) nanofluids along a continuously stretching surface. Magnetic dipole is taken in this fashion that its center exactly lies on the $y-$axis below $x-$axis at a distance d. The flow is caused in behalf of stretching of sheet. The surface stretched along velocity $U_w = Sx$ (S is a dimensionless constant) and $T = T_w$ and $T = T_\infty$ symbolizes the respective temperature at the stretching sheet and ambient fluid. The magnetic field points of magnetic dipole are applied in positive $x-$direction. To make ferrofluid saturate, the magnetic dipole improve the magnetic field of significant strength. The fluid above Curie temperature T_c is incapable of magnetization. The temperature $T = T_\infty$ is supposed to be temperature of the fluid, where $T_\infty < T_w < T_c$. It is presumed that the nanoparticles and base fluids are in thermal equilibrium. The thermophysical properties of $C_2H_6O_2$-$MnZnFe_2O_4$ (ethylene glycol-manganese zinc ferrite), $NiZnFe_2O_4$-$C_2H_6O_2$ (nickel zinc ferrite-ethylene glycol), $C_2H_6O_2$-Fe_3O_4

(ethylene glycol-magnetite ferrite), H_2O-$NiZnFe_2O_4$ (water-nickel zinc ferrite), H_2O-$MnZnFe_2O_4$ (water-manganese zinc ferrite), and Fe_3O_4-H_2O (magnetite ferrite-water) nanofluids are taken in table 7.1. Utilizing these assumptions into account, employing the boundary layer approximation, the equations in a ferrohydrodynamic and thermal energy

$$\frac{\partial u}{\partial x} + \frac{\partial v}{\partial y} = 0, \tag{7.1}$$

$$\rho_{nf}\left(u\frac{\partial u}{\partial x} + v\frac{\partial u}{\partial y}\right) = -\frac{\partial P}{\partial x} + \mu_0 M\frac{\partial H}{\partial x} + \mu_{nf}\frac{\partial^2 u}{\partial y^2} - \frac{\mu_{nf}\epsilon}{K_1}u, \tag{7.2}$$

$$(\rho c_p)_{nf}\left(u\frac{\partial T}{\partial x} + v\frac{\partial T}{\partial y}\right) - \mu_0 K_p T\left(u\frac{\partial H}{\partial x} + v\frac{\partial H}{\partial y}\right) = k_{nf}\frac{\partial^2 T}{\partial y^2}. \tag{7.3}$$

The admissible boundary conditions are

$$u|_{y=0} = U_w(x) = Sx, \, v|_{y=0} = 0, \, \frac{\partial T}{\partial y}\bigg|_{y=0} = -h_c T, \tag{7.4}$$

$$u|_{y\to\infty} \to 0, \, T|_{y\to\infty} \to T_c. \tag{7.5}$$

In Eq. (7.4), the condition recommended at $y = 0$ for temperature speaks to the effects Newtonian heating, h_c signify heat transfer coefficient.

7.3   Thermo-physical properties of $MnZnFe_2O_4$-$C_2H_6O_2$, $NiZnFe_2O_4$-$C_2H_6O_2$, Fe_3O_4-$C_2H_6O_2$, $MnZnFe_2O_4$-H_2O, $NiZnFe_2O_4$-H_2O, and Fe_3O_4-H_2O

Expressions for μ_{nf} (dynamic viscosity), $(\rho c_p)_{nf}$ (specific heat or heat capacitance), ρ_{nf} (effective dynamic density), and k_{nf} (thermal conductivity) are stated for the nanofluid in Eq. (6.6). Thermo-physical properties of ferrite nanoparticles are tabulated in table 7.1. The schematic system for the flow evaluation is delineated in Figure 7.1.

	ρ(Kg/m^3)	C_p(J/KgK)	k(W/mK)	Pr
Ethylene glycol C$_2$H$_6$O$_2$	1116.6	2382	0.249	204
Water H$_2$O	998.3	4182	0.60	6.96
Nickel zinc ferrite NiZnFe$_2$O$_4$	4800	710	6.3	—
Manganese zinc ferrite MnZnFe$_2$O$_4$	4700	1050	3.9	—
Magnetite ferrite Fe$_3$O$_4$	5180	670	9.7	—

Table 7.1: Thermo-physical properties of H$_2$O, C$_2$H$_6$O$_2$, MnZnFe$_2$O$_4$, NiZnFe$_2$O$_4$,and Fe$_3$O$_4$.
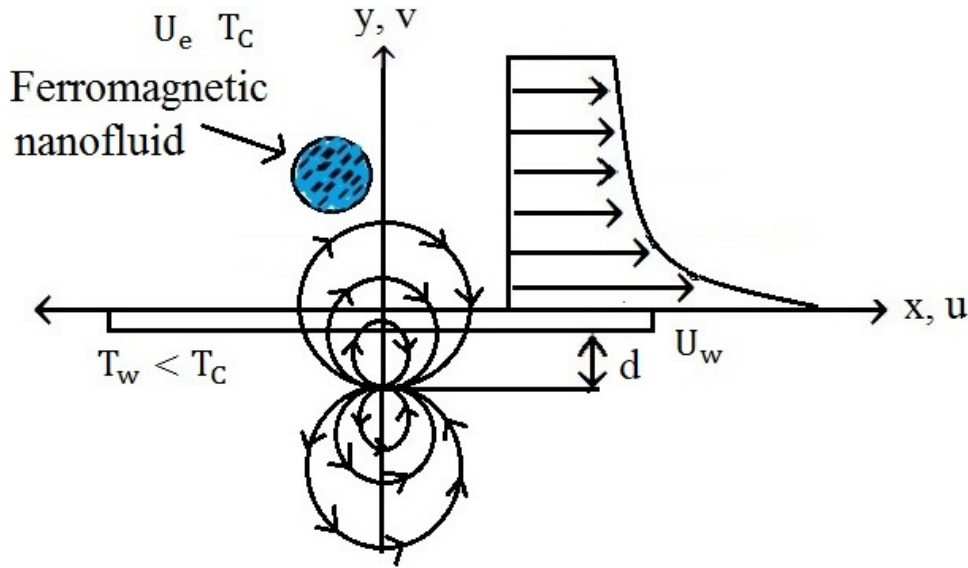
Figure 7.1: Geometery of the flow.

7.4 Solution procedure

The assumed dimensionless variables are

$$\psi(\eta, \xi) = \eta(\frac{\mu_f}{\rho_f})f(\xi), \quad \theta(\xi, \eta) \equiv \frac{T_c - T}{T_w - T_c} = \theta_1(\xi) + \eta^2\theta_2(\xi). \tag{7.6}$$

Where $\theta_2(\xi)$ and $\theta_1(\xi)$ exhibit dimensionless temperature, the corresponding dimensionless coordinates are

$$\xi = y\sqrt{\frac{\rho_f S}{\mu_f}}, \quad \eta = x\sqrt{\frac{\rho_f S}{\mu_f}}. \tag{7.7}$$

The stream function is defined in this fashion that the mass equation satisfies directly, here the $\psi(\eta, \xi)$ signifies the stream function, (u, v) symbolizes the comparable

components of velocity defined below

$$u = \frac{\partial \psi(\eta, \xi)}{\partial y} = Sx f'(\xi), \quad v = -\frac{\partial \psi(\eta, \xi)}{\partial x} = -\sqrt{\frac{S\mu_f}{\rho_f}} f(\xi), \tag{7.8}$$

where prime expresses differentiation corresponding to ξ and η. Employing the similarity transformations given in Eqs. (2.6)-(2.12) and (7.6) to (7.8), Eqs. (7.2) and (7.3) along Eqs. (7.4) and (7.5) reduces to the system of boundary value problem

$$\frac{(1-\varphi)^{-25/10}}{(1-\varphi+\varphi\frac{\rho_s}{\rho_f})} f''' - f'^2 + f f'' - \frac{2\beta\theta_1}{(1-\varphi+\varphi\frac{\rho_s}{\rho_f})(\xi+\gamma)^4} - \frac{P_m}{(1-\varphi+\varphi\frac{\rho_s}{\rho_f})} f' = 0, \tag{7.9}$$

$$\frac{k_{nf}/k_f}{(1-\varphi+\varphi\frac{(\rho c_p)_s}{(\rho c_p)_f})}\theta_1'' + Pr f\theta_1' + \frac{2\lambda\beta\ f(\theta_1-\varepsilon)}{(\xi+\gamma)^3} + 2\theta_2 - 4\lambda f'^2 = 0, \tag{7.10}$$

$$\frac{k_{nf}/k_f}{(1-\varphi+\varphi\frac{(\rho c_p)_s}{(\rho c_p)_f})}\theta_2'' - Pr(2f'\theta_2 - f\theta_2') + \frac{2\lambda\beta\ f\theta_2}{(\xi+\gamma)^3}$$

$$- 4\lambda f''^2 - \lambda\beta\ (\theta_1-\varepsilon)\left(\frac{2f'}{(\xi+\gamma)^4} + \frac{4f}{(\xi+\gamma)^5}\right) = 0, \tag{7.11}$$

$$f(\xi) = 0, f'(\xi) = 1, \theta_1'(\xi) = -\delta_h(1+\theta_1(0)), \theta_2(\xi) = 0, \quad at\ \xi = 0, \tag{7.12}$$

$$f'(\xi) \to 0, \theta_1(\xi) \to 0, \theta_2(\xi) \to 0, \quad when\ \xi \to \infty. \tag{7.13}$$

In above system of nonlinear equations, the parameters λ (viscous dissipation), δ_h (the conjugate parameter of Newtonian heating), β (ferrohydrodynamic interaction), P_m (porosity parameter), Pr (Prandtl number), and ε (Curie temperature) are defined as

$$\varepsilon = \frac{T_c}{T_w - T_c}, \delta_h = h_c\sqrt{\frac{\nu_f}{S^2}}, \beta = \frac{\gamma_1}{2\pi}\frac{\mu_0 K_p(T_w - T_c)\rho_f}{\mu_f^2},$$

$$Pr = \frac{\nu_f}{\alpha_f}, P_m = \frac{\nu_f\epsilon}{K_1 S}, \lambda = \frac{S\mu_f^2}{\rho_f K_p(T_w - T_c)}, \gamma = \sqrt{\frac{S\rho_f d^2}{\mu_f}}. \tag{7.14}$$

At the walls, the parameters of engineering interest, i.e., the friction drag and rate of heat transfer are

$$C_f = \frac{2\tau_w}{\rho U_w^2}, \quad \tau_w = \mu_{nf}\frac{\partial u}{\partial y}\Big|_{y=0},$$

$$Nu_x = \frac{xk_{nf}}{k_f(T_w - T_c)}\frac{\partial T}{\partial y}\Big|_{y=0}, \tag{7.15}$$

We finally achieved the following dimensionless equations for friction drag and Nusselt number, i.e. local surface heat flux

$$
\frac{1}{2}Re^{1/2}C_f = \frac{1}{(1-\varphi)^{25/10}}f''(0),
$$

$$
Re^{-1/2}Nu_x = -\delta_h \frac{k_{nf}}{k_f}\left(1 + \frac{1}{\theta_1(0) + \eta^2\theta_2(0)}\right). \tag{7.16}
$$

$\frac{1}{2}Re^{1/2}C_f$ signify the friction drag and $Re^{-1/2}Nu_x$ exemplify the heat transfer rate, in which $Re_x = \frac{xU_w(x)}{\nu_f} = \frac{Sx^2}{\nu_f}$ signify local Reynolds number depends upon the surface stretching velocity $U_w(x)$.

7.4.1   Optimal homotopy analysis method

BVPh2-midpoint method (Maple) and optimal HAM (Mathematica 9.0) are implemented in current analysis for the solution of equation. These techniques are utilized to get the solutions for highly non-linear equations. The optimal HAM utilizes the homotopy/auxiliary parameter to depict that a nonlinear system of differential equations may be divided into a set of linear system of differential equations that can be solved analytically. Moreover, the optimal HAM [96, 97] gives better results compared with perturbation techniques and other conventional investigative techniques. Firstly, the optimal HAM gives us a remarkable flexibility to pick the equation type of linear sub-problems. Secondly, the optimal HAM works regardless of the possibility that there do not exist any large/small auxiliary parameters in determining equations and boundary/initial conditions. Particularly, unlike perturbation and other analytic techniques, the optimal HAM gives us an advantageous approach to guarantee the convergence of solution by presenting the supposed physical parameter into the series solution. In evaluation of the problem, one needs the linear operators and initial guesses which are given below for the under discussion problem.

$$
L_f(f) = \frac{d^3f}{d\xi^3} + \frac{d^2f}{d\xi^2}, \quad L_{\theta_1}(\theta_1) = \frac{d^2\theta_1}{d\xi^2} - \theta_1,
$$

$$
L_{\theta_2}(\theta_2) = \frac{d^2\theta_2}{d\xi^2} - \theta_2, \tag{7.17}
$$

$$
f_0(\xi) = 1 - exp(-\xi), \quad \theta_{1_0}(\xi) = \frac{\delta_h}{1-\delta_h}exp(-\xi),
$$

$$
\theta_{2_0}(\xi) = \xi exp(-\xi), \tag{7.18}
$$

where $L_f(f)$, $L_{\theta_1}(\theta_1)$, and $L_{\theta_2}(\theta_2)$ symbolizes the linear operators, while $f_0(\xi)$, $\theta_{1_0}(\xi)$ and $\theta_{2_0}(\xi)$ illustrates initial guesses of f, θ_1, and θ_2.

7.4.2   Convergence analysis of optimal HAM solution

The auxiliary parameters h_f, h_{θ_1}, and h_{θ_2} have a leading purpose in controlling the convergence of the solution. To get a convergent analytic solutions, preferred values are assigns to h_f, h_{θ_1}, and h_{θ_2}. For this reason, residual errors are observed for ferrohydrodynamic equations by implementing the expressions defined in Eqs. (2.26)-(2.28). These expressions are utilized in the evaluation of convergence for the optimal HAM, the resulting convergence and residual errors are listed in tables 7.2 and 7.3. Figure 7.2 reveals the average square residual error for 12th order. Δ_m^f exhibits the total square residual error, defined in Eq. (2.29).

$\frac{values \rightarrow}{order \downarrow}$	h_f	h_{θ_1}	h_{θ_2}	Δ_m^t
4	-0.40025	-0.42903	-0.97231	0.009324
6	-0.44380	-0.49902	-0.98331	2.5489×10^{-4}
8	-0.54992	-0.49930	-0.99005	1.09211×10^{-10}
10	-0.60321	-0.54173	-0.92152	3.62310×10^{-15}
12	-0.76119	-0.76497	-1.10921	7.16290×10^{-21}

Table 7.2: Average residual square errors Δ_m^t.

$\frac{values \rightarrow}{order \downarrow}$	$h_f = -0.76119$	$h_{\theta_1} = -0.76497$	$h_{\theta_2} = -1.10921$
8	2.54891×10^{-20}	3.44370×10^{-10}	9.54570×10^{-10}
10	6.43670×10^{-22}	1.45219×10^{-16}	0.64881×10^{-14}
12	0.32671×10^{-25}	8.33670×10^{-20}	6.45672×10^{-18}
20	2.34589×10^{-26}	1.54891×10^{-25}	2.43370×10^{-23}

Table 7.3: Individual residual square errors for Δ_m^f, $\Delta_m^{\theta_1}$, and $\Delta_m^{\theta_2}$.
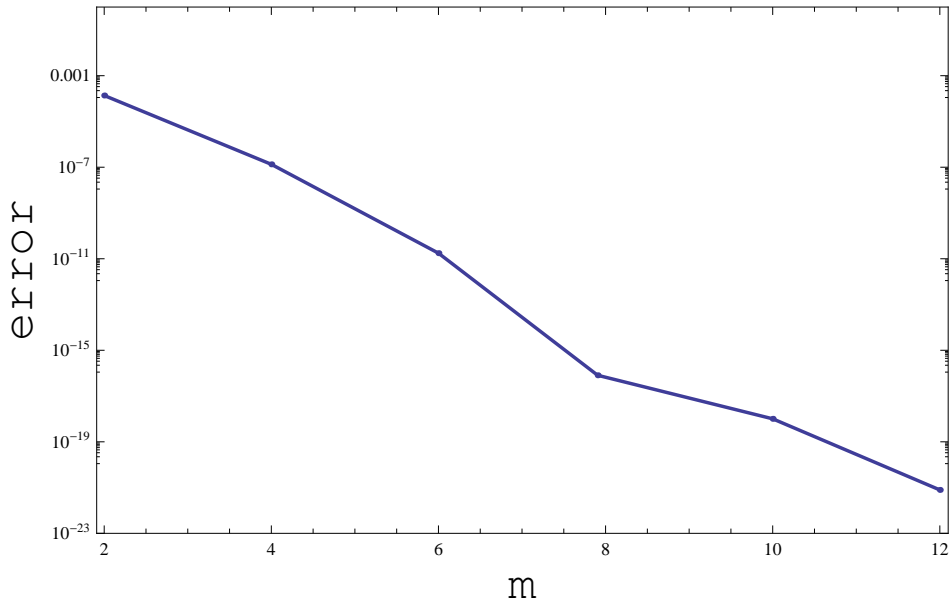
Figure 7.2: Graph for 12th order approximation.

7.5 Discussion

The substantial clarification of sundry parameters on the flow field is scrutinized in this section. The consequence of dimensionless emerging parameters β (ferrohydrodynamic interaction), δ_h (conjugate parameter due to Newtonian heating), φ (solid volume fraction), λ (viscous dissipation), P_m (porosity parameter), and Pr (Prandtl number) are analyzed. Moreover, the rest of the materialized parameters in the flow problem are considered as fixed. The fixed values of these parameters are $\lambda = 0.01$, $\varepsilon = 2.0$, $\gamma = 1.0$. The boundary value problem is solved numerically and analytically via BVPh2-midpoint method and optimal HAM respectively. The accuracy of the present optimal HAM and BVPh2-midpoint method is tested by comparing $\theta_1'(0)$ with those of Rashidi et al. [94] tabulated in table 8.4. The results achieved for current problem agrees. The flow of a ferromagnetic $NiZnFe_2O_4$-$C_2H_6O_2$, $NiZnFe_2O_4$-H_2O, $MnZnFe_2O_4$-$C_2H_6O_2$, $MnZnFe_2O_4$-H_2O, Fe_3O_4-$C_2H_6O_2$, and Fe_3O_4-H_2O nanofluids with nanoparticles are scrutinized. In contemplation of an obvious insight into the existing flow problem, the conclusion are determined for the axial velocity, temperature field, friction drag, and Nusselt number graphically. The analysis is implemented in the presence of magnetic dipole.

The influence of parameter φ (solid volume fraction) of the ferromagnetic $NiZnFe_2O_4$-$C_2H_6O_2$, $NiZnFe_2O_4$-H_2O, $MnZnFe_2O_4$-$C_2H_6O_2$, $MnZnFe_2O_4$-H_2O, Fe_3O_4-$C_2H_6O_2$,

and Fe_3O_4-H_2O nanofluids are depicted in Figures 7.3 and 7.4 on the dimensionless axial velocity and temperature field. It is evident from Figure 7.3 that the axial velocity of the respective nanofluids declines along improvement in parameter φ. The axial velocity reduces away from surface. In fact, improvement in parameter φ (solid volume fraction) causes to concentrates the ferromagnetic fluid which consequently produces resistance to the moments of liquid particles that leads to decline the axial velocity for both the base fluids, i.e., H_2O and $C_2H_6O_2$ (water and ethylene glycol). The presence of magnetic dipole provides attraction to the ferrites nanoparticles due to which the axial velocity of the ferromagnetic nanofluids slows down. It means that magnetic dipole plays a vital role in reducing the movements of fluid particles. Further, Figure 7.3 depicts that Fe_3O_4 (magnetite ferrite) nanoparticles are more magnetized as compared to $NiZnFe_2O_4$ (nickel zinc ferrite) and $MnZnFe_2O_4$ (manganese zinc ferrite) nanoparticles. The more magnetization, the more will be resistance produced by the magnetic dipole to the fluid particles, as a result, it is depicted that Fe_3O_4-$C_2H_6O_2$ and Fe_2O_4-H_2O ferromagnetic nanofluids have low velocity as compared to the ferromagnetic $NiZnFe_2O_4$-$C_2H_6O_2$, $NiZnFe_2O_4$-H_2O, $MnZnFe_2O_4-C_2H_6O_2$, and $MnZnFe_2O_4$-H_2O nanofluids. The characteristics of parameter φ (solid volume fraction) on temperature field of the ferromagnetic $NiZnFe_2O_4$-$C_2H_6O_2$, $NiZnFe_2O_4$-H_2O, $MnZnFe_2O_4$-$C_2H_6O_2$, $MnZnFe_2O_4$-H_2O, $Fe_3O_4-C_2H_6O_2$, and $Fe_3O_4-H_2O$ nanofluids in presence of magnetic dipole are delineated in Figure 7.4. It is illustrated that temperature field of $Fe_3O_4-C_2H_6O_2$ and Fe_3O_4-H_2O is higher than $NiZnFe_2O_4$-$C_2H_6O_2$, $NiZnFe_2O_4$-H_2O, $MnZnFe_2O_4-C_2H_6O_2$, and $MnZnFe_2O_4$-H_2O nanofluids in presence of magnetic dipole. In fact, thermal conductivity of Fe_3O_4 (magnetite ferrite) nanoparticles is higher than the thermal conductivity of $NiZnFe_2O_4$ (nickel zinc ferrite) and $MnZnFe_2O_4$ (manganese zinc ferrite) nanoparticles. Moreover, the presence of magnetic dipole makes higher the temperature field until the temperature of the fluid reach to the Curie temperature T_c of the fluid. In fact, magnetic dipole produces more resistance to the Fe_3O_4 (magnetite ferrite) nanoparticles as compared to $NiZnFe_2O_4$ (nickel zinc ferrite) and $MnZnFe_2O_4$ (manganese zinc ferrite) nanoparticles, which improve the temperature field. If the temperature of the ferrite nanoparticles is higher than the Curie temperature T_c then these ferrite nanoparticles lose their magnetization and there will be no attraction for ferrite nanoparticles whose temperature is higher than the Curie temperature T_c.

The impact of parameter β (ferrohydrodynamic interaction) is displayed in Figures 7.5 and 7.6. The existence of parameters γ (dimensionless distance from origin to center of magnetic dipole), ε (Curie temperature), and β (ferrohydrodynamic interaction)

is necessary to hold the impact of ferromagnetic effect on the boundary layer flow. The presence of Fe_3O_4 (magnetite ferrite), $NiZnFe_2O_4$ (nickel zinc ferrite), and $MnZnFe_2O_4$ (manganese zinc ferrite) nanoparticles in a viscous carrier fluid corresponds to ferromagnetic nanofluid, because of which viscosity enhances and subsequently the axial velocity reduces for enlarging values of parameter β (ferrohydrodynamic interaction) as shown in Figure 7.5. The consequence of β (ferrohydrodynamic interaction) on axial velocity is carried out for the ferromagnetic $NiZnFe_2O_4$-$C_2H_6O_2$, $NiZnFe_2O_4$-H_2O, $MnZnFe_2O_4$-$C_2H_6O_2$, $MnZnFe_2O_4$-H_2O, Fe_3O_4-$C_2H_6O_2$, and Fe_3O_4-H_2O nanofluids. It is noticed that the exitance of magnetic dipole makes a rapid reduction in the axial velocity of the ferromagnetic nanofluids when water is used as base fluid. The physical interpretation is that the magnetic dipole attracts the ferrite Fe_3O_4 (magnetite ferrite), $NiZnFe_2O_4$ (nickel zinc ferrite) and $MnZnFe_2O_4$ (manganese zinc ferrite) nanoparticles which result in the enhancement of the viscosity of the nanofluid inside the boundary layer and as a result, the axial velocity slows down. The highest velocity is observed for the $C_2H_6O_2$ (ethylene glycol, when $\varphi = 0$) and H_2O (water, when $\varphi = 0$), whereas the lowest axial velocity is observed for the $Fe_3O_4 - C_2H_6O_2$ (magnetite ferrite-ethylene glycol, when $\varphi = 0.15$) and $Fe_3O_4 - H_2O$ (magnetite ferrite-water, when $\varphi = 0.15$) nanofluids as evident in Figure 7.5. Behavior of parameter β (ferrohydrodynamic interaction) on distribution of temperature is revealed in Figure 7.6. It is depicted that the larger values of parameter β (ferrohydrodynamic interaction) improve the temperature of the nanofluid in presence of the magnetic dipole. It is because of the interaction between an action of a magnetic field and movements of Fe_3O_4 (magnetite ferrite), $NiZnFe_2O_4$ (nickel zinc ferrite) and $MnZnFe_2O_4$ (manganese zinc ferrite) nanoparticles. The interaction between magnetic field action and Fe_3O_4 (magnetite ferrite), $NiZnFe_2O_4$ (nickel zinc ferrite) and $MnZnFe_2O_4$ (manganese zinc ferrite) nanoparticles thinning the axial velocity thereby enhancing frictional heating among liquid layers, that improve thermal boundary layer, i.e., the reduction in movements of Fe_3O_4 (magnetite ferrite), $MnZnFe_2O_4$ (manganese zinc ferrite), $NiZnFe_2O_4$ (nickel zinc ferrite) nanoparticles results in the enhancement of distribution of temperature.

The behavior of parameter P_m (Porosity) in the flow of ferromagnetic $NiZnFe_2O_4$-$C_2H_6O_2$, $NiZnFe_2O_4$-H_2O, $MnZnFe_2O_4$-$C_2H_6O_2$, $MnZnFe_2O_4$-H_2O, Fe_3O_4-$C_2H_6O_2$, and Fe_3O_4-H_2O nanofluids is observed in Figure 7.7. The existence of parameters P_m (Porosity) in the presence of Fe_3O_4 (magnetite ferrite), $NiZnFe_2O_4$ (nickel zinc ferrite) and $MnZnFe_2O_4$ (manganese zinc ferrite) nanoparticles in a viscous carrier ferromagnetic nanofluid slow down the axial velocity and as a result the axial velocity

reduces for enlarging values of parameter P_m (Porosity) as shown in Figure 7.7. It is depicted that for ferrites-water based ferromagnetic nanofluid in the presence of magnetic dipole, the axial velocity reduces rapidly. The physical interpretation is that an increase in P_m (Porosity) causes to produce more resistance to the fluid particles, and the magnetic dipole attracts the ferrite Fe_3O_4 (magnetite ferrite), $MnZnFe_2O_4$ (manganese zinc ferrite), and $NiZnFe_2O_4$ (nickel zinc ferrite) nanoparticles which result in the enhancement of the viscosity of the nanofluid inside the nano-boundary layer and as a result the axial velocity slow down. The highest velocity is observed for the $C_2H_6O_2$ (ethylene glycol, when $\varphi = 0$) and H_2O (water, when $\varphi = 0$), whereas the lowest axial velocity is observed for the $Fe_3O_4-C_2H_6O_2$ (magnetite ferrite-ethylene glycol, when $\varphi = 0.15$) and $Fe_3O_4-H_2O$ (magnetite ferrite-water, when $\varphi = 0.15$) nanofluids as evident in Figure 7.7.

The influence of conjugate parameter δ_h of Newtonian heating on axial velocity and temperature profile are addressed in Figures 7.8 and 7.9. It is disclosed from Figure 7.8 that an increase in the δ_h (conjugate parameter) prompts change in the axial velocity of the ferromagnetic $NiZnFe_2O_4$-$C_2H_6O_2$, $NiZnFe_2O_4$-H_2O, $MnZnFe_2O_4$-$C_2H_6O_2$, $MnZnFe_2O_4$-H_2O, Fe_3O_4-$C_2H_6O_2$, and Fe_3O_4-H_2O nanofluids, the consequence indicate that the axial velocity and relative nano-boundary layer declines for δ_h (conjugate parameter), i.e., the axial velocity is reduces. It is inspected that the response velocity reduces with rise (increasing values of δ_h) of an elastic force of the working fluid. The impacts of δ_h (conjugate parameter) on temperature field is characterized in Figure 7.9. Correspondingly an enhancement in conjugate parameter arises the rate of heat transfer that improves the temperature of the ferromagnetic $NiZnFe_2O_4$-$C_2H_6O_2$, $NiZnFe_2O_4$-H_2O, $MnZnFe_2O_4$-$C_2H_6O_2$, $MnZnFe_2O_4$-H_2O, Fe_3O_4-$C_2H_6O_2$, and Fe_3O_4-H_2O nanofluids. Moreover, thermal boundary layer thickness arises. It is likewise perceived that temperature at wall is higher for conjugate parameter.
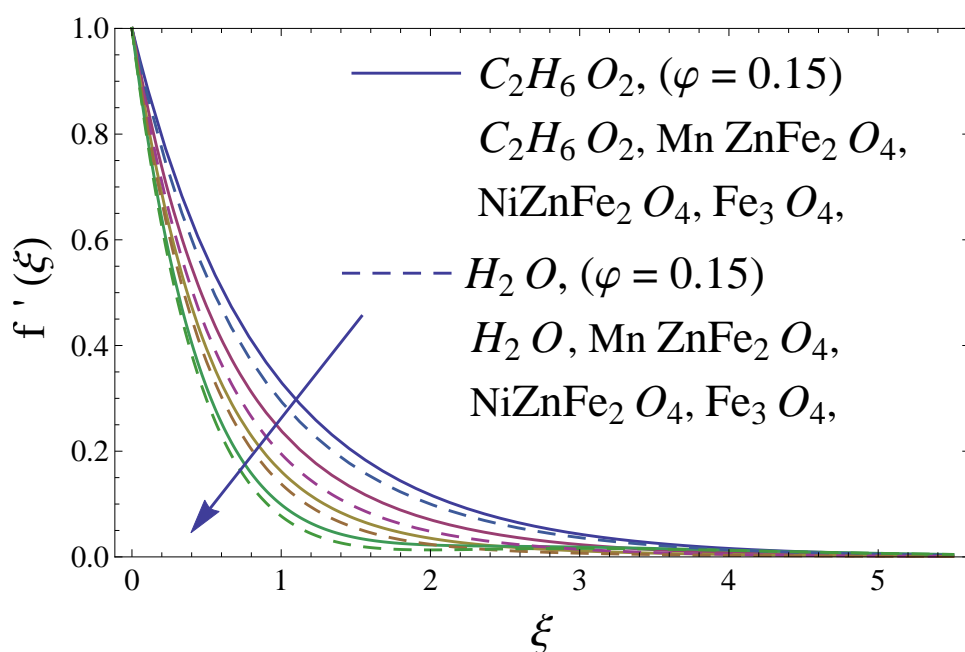
Figure 7.3: Comparitive inspection of parameter φ on axial velocity in $C_2H_6O_2$ and H_2O.
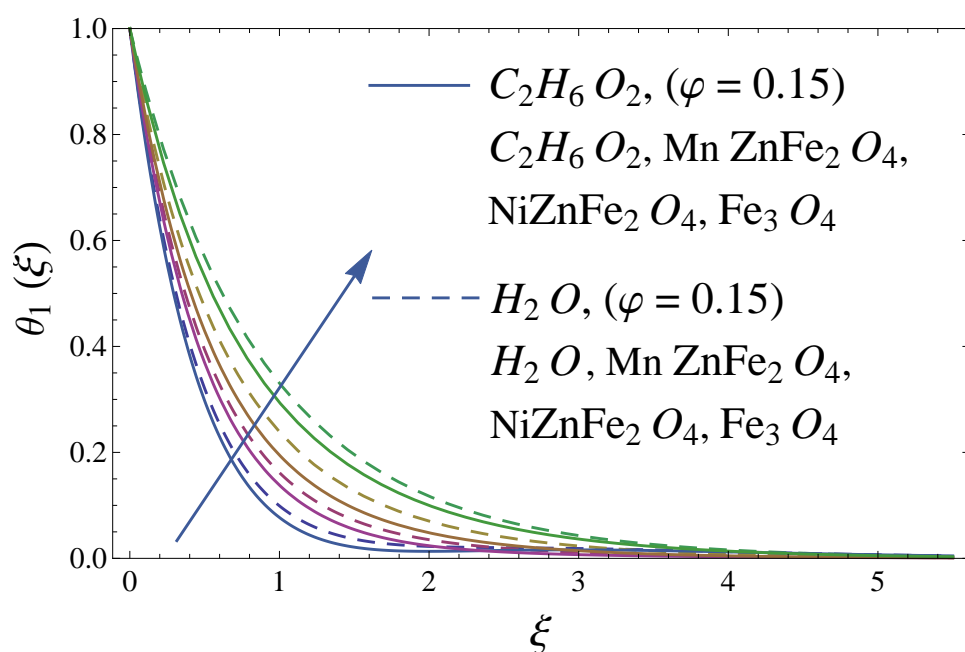
Figure 7.4: Comparitive inspection of parameter φ on distribution of temperature in presence of $C_2H_6O_2$ and H_2O.
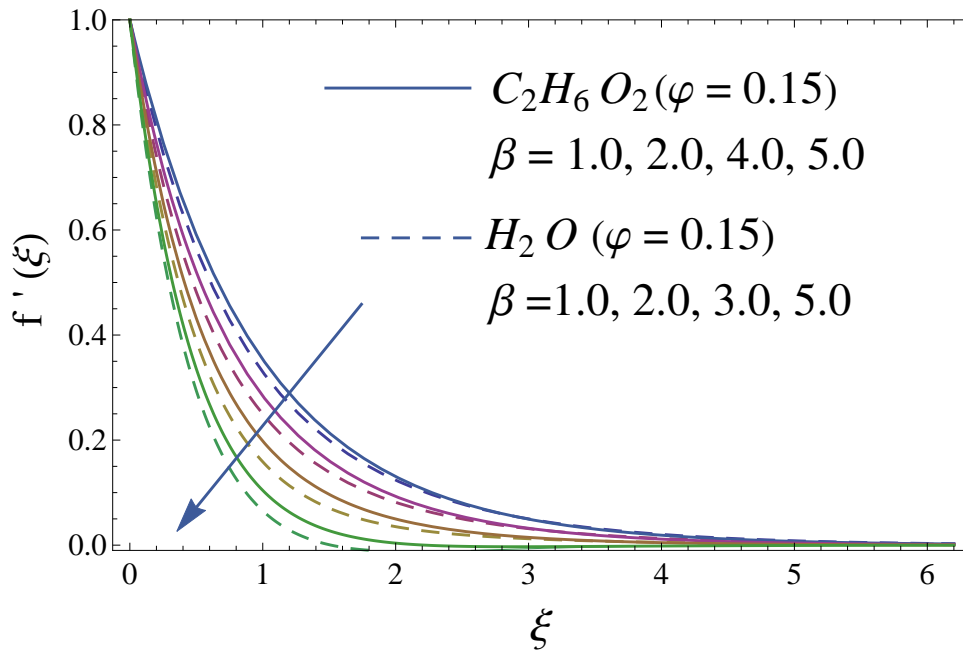
Figure 7.5: Comparitive study of ferrohydrodynamic interaction parameter on axial velocity in presence of H_2O and $C_2H_6O_2$.
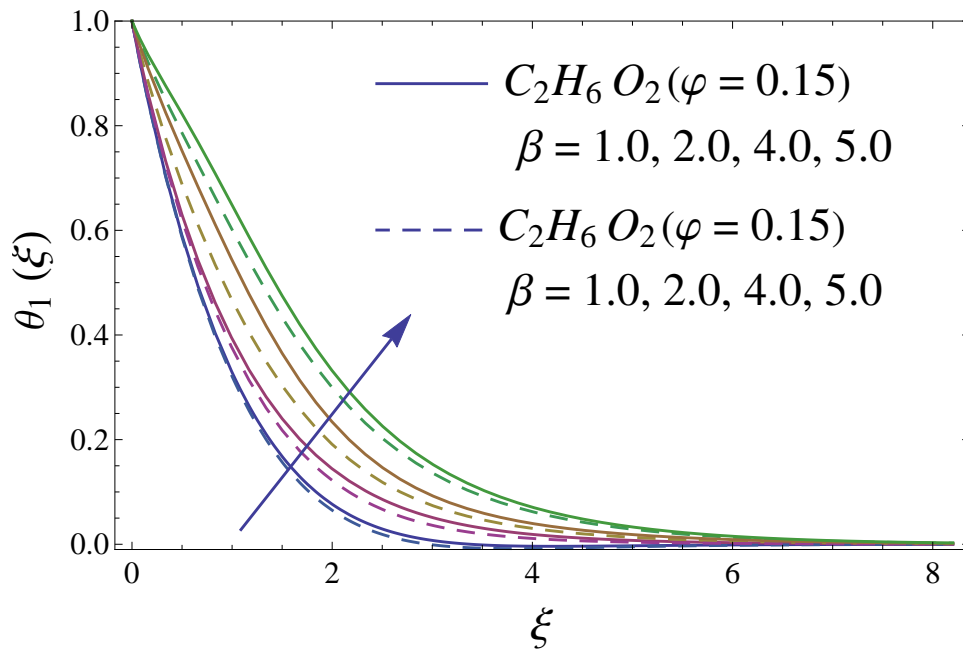
Figure 7.6: Comparitive study of parameter β on distribution of temperature in presence of H_2O and $C_2H_6O_2$.

Figure 7.7: Comparitive examination of parameter P_m on axial velocity in presence of $C_2H_6O_2$ and H_2O.

Figure 7.8: Comparitive examination of parameter δ_h on velocity distribution in presence of H_2O and $C_2H_6O_2$.

Figure 7.9: Comparitive examination of parameter δ_h on temperature field in presence of $C_2H_6O_2$ and H_2O.

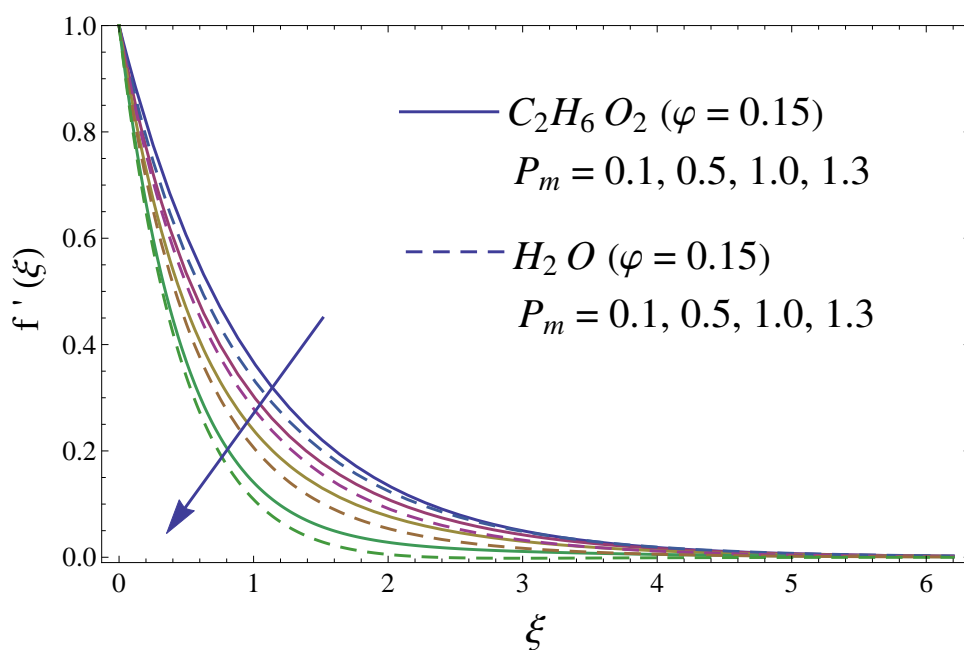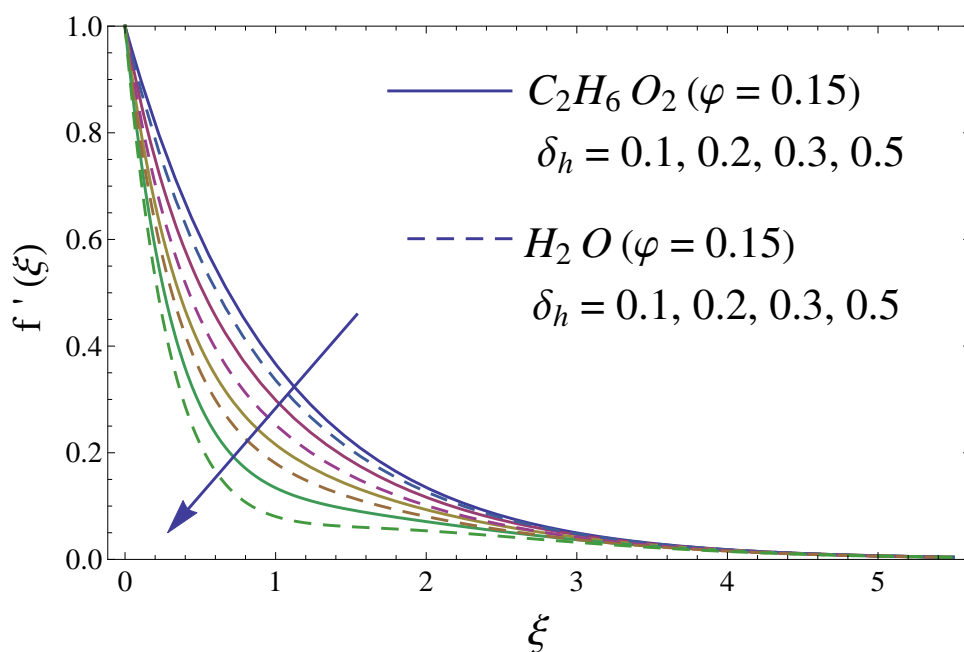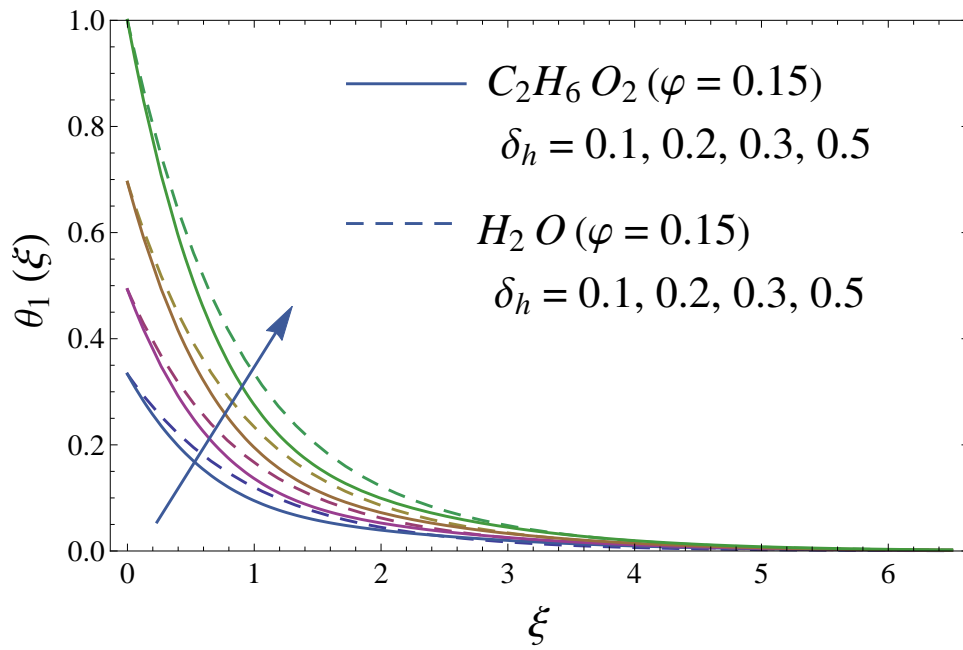## 7.5.1   Friction drag and local Nusselt number

The mathematical relations for the friction drag and rate of transfer of heat are expressed in Eqs. (7.15) and (7.16). The influence of parameter φ (solid volume fraction) on wall shear stress of the ferromagnetic $NiZnFe_2O_4$-$C_2H_6O_2$, $NiZnFe_2O_4$-H_2O, $MnZnFe_2O_4$-$C_2H_6O_2$, $MnZnFe_2O_4$-H_2O, Fe_3O_4-$C_2H_6O_2$, and Fe_3O_4-H_2O nanofluids in presence of the magnetic dipole is evident in Figures 7.10 and 7.11. It is seen that the presence of water based ferrite nanoparticles reduces the wall shear stress as compared to the case when ethylene glycol-based ferrite nanoparticles are used. The skin friction coefficient is analyzed in the presence of magnetic dipole. Since we know that the magnetic dipole attracts the Fe_3O_4 (magnetite ferrite), $NiZnFe_2O_4$ (nickel zinc ferrite) and $MnZnFe_2O_4$ (manganese zinc ferrite) nanoparticles which result in the enhancement of the viscosity of the nanofluid inside the boundary layer and yet the wall shear stress increases. The lowest wall shear stress is depicted for the $C_2H_6O_2$ (ethylene glycol, when $\varphi = 0$) and H_2O (water, when $\varphi = 0$) and the highest wall shear stress is observed for the Fe_3O_4-$C_2H_6O_2$ magnetite ferrite-ethylene glycol, when $\varphi = 0.15$) and Fe_3O_4-H_2O (magnetite ferrite-water, when $\varphi = 0.15$) nanofluids as evident in Figures 7.10 and 7.11. Moreover, φ (solid volume fraction) of the ferromagnetic $NiZnFe_2O_4$-$C_2H_6O_2$, $NiZnFe_2O_4$-H_2O, $MnZnFe_2O_4$-$C_2H_6O_2$, $MnZnFe_2O_4$-H_2O, Fe_3O_4-$C_2H_6O_2$, and Fe_2O_4-H_2O nanofluids in the presence of the magnetic dipole via heat transfer rate are analyzed in Figures 7.12 and 7.13. It is scrutinized from Figure 7.12 that the heat transfer rate reduces for ferromagnetic $NiZnFe_2O_4$-$C_2H_6O_2$, $NiZnFe_2O_4$-H_2O, $MnZnFe_2O_4$-$C_2H_6O_2$, $MnZnFe_2O_4$-H_2O, Fe_3O_4-$C_2H_6O_2$, and Fe_3O_4-H_2O nanofluids. The fast reduction in heat transfer rate is observed in presence of water based ferrite nanoparticles, instead, from Fig. 7.13, it is evident that an increase in heat transfer rate is depicted for the respective ferromagnetic nanofluids.
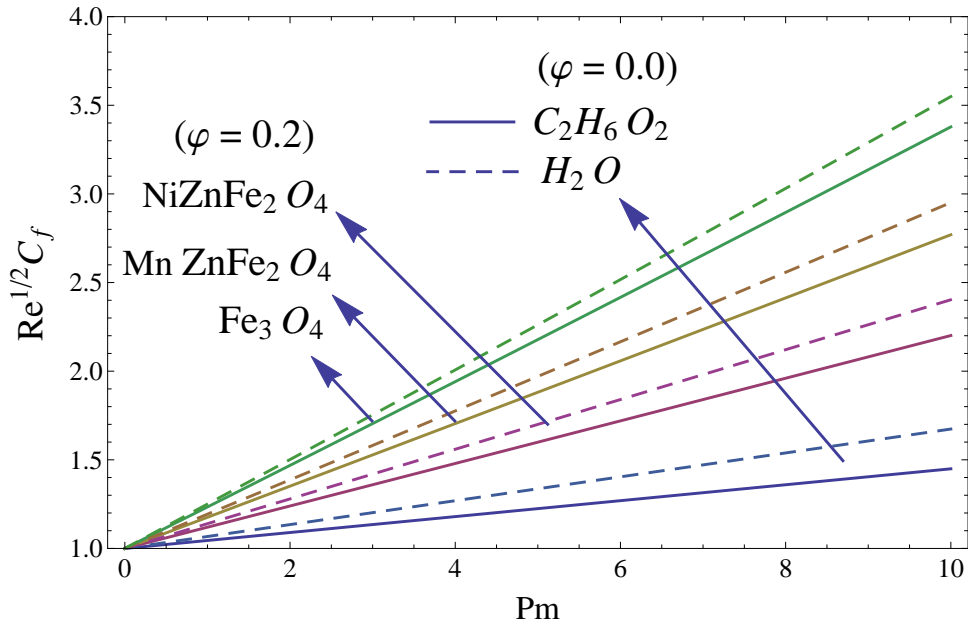
Figure 7.10: Wall shear stress versus P_m.
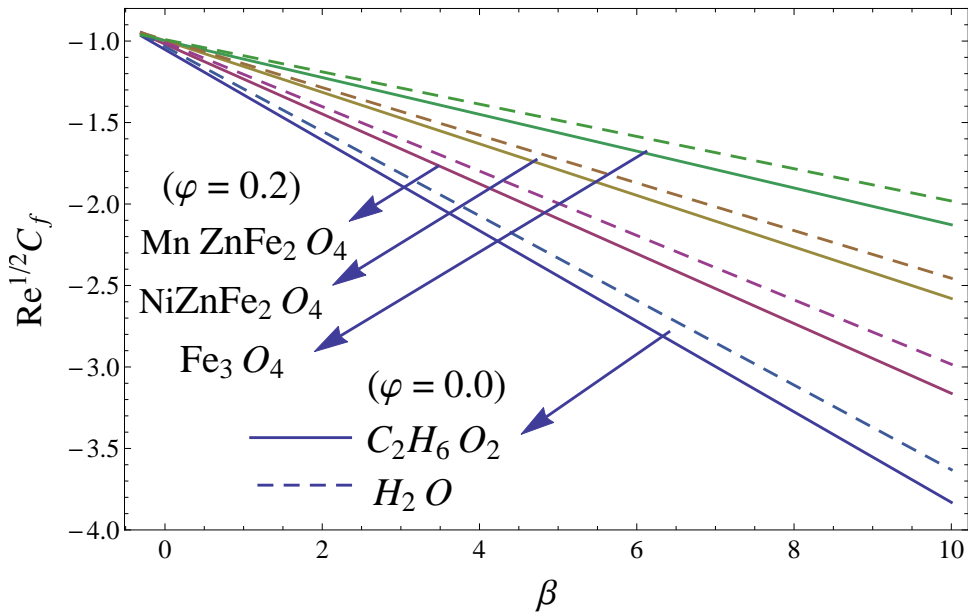
Figure 7.11: Wall shear stress versus β.
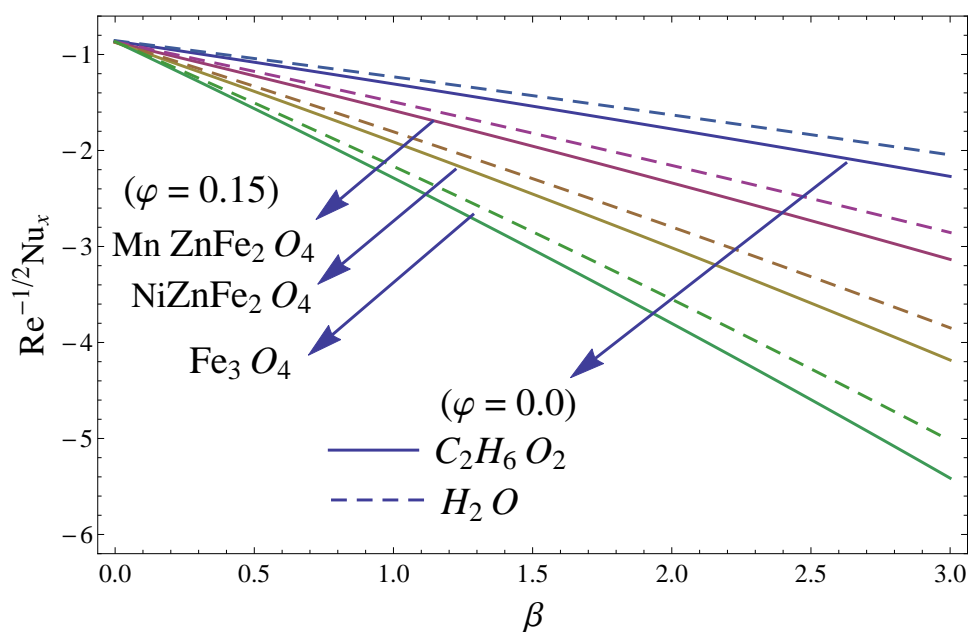
Figure 7.12: Heat transfer rate versus β.
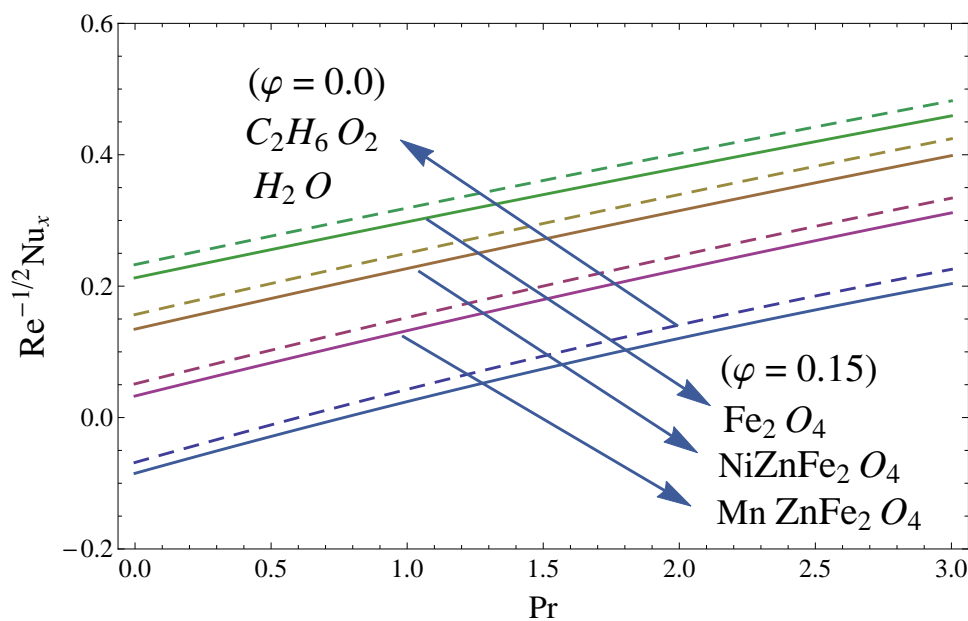
Figure 7.13: Heat transfer rate versus λ.

Pr	Rashidi [94]	$Re_x^{-1/2} Nu_x$ (Optimal HAM)	$Re_x^{-1/2} Nu_x$ (BVPh2-Midpoint)
0.72	0.808631	0.808641	0.808639
1.0	1.000000	1.000000	1.000000
3.0	1.923682	1.923690	1.923672
4.0	− − −	2.003170	2.003162
5.0	− − −	2.329810	2.329871
8.0	− − −	− − −	2.541990

Table 7.4: Comparison of Nusselt number.

Concluding remarks

The purpose of the article exhibit theoretically the practicability of the concept of ferromagnetic nanofluids with Fe_3O_4 (magnetite ferrite), $NiZnFe_2O_4$ (nickel zinc ferrite), and $MnZnFe_2O_4$ (manganese zinc ferrite) as ferrites nanoparticles and H_2O (water) and $C_2H_6O_2$ (ethylene glycol) as base fluid. The heat transport phenomenon is depicted in the resulting ferromagnetic nanofluids. The boundary value problem is scrutinized numerically and analytically as a consequence of BVPh2-midpoint method and optimal homotopy analysis method respectively. The determination of the analysis are

- An increase in φ (solid volume fraction) results in the reduction of axial velocity and enhances the temperature field.

- The existence of parameters P_m (Porosity) in the presence of Fe_3O_4 (magnetite ferrite), $NiZnFe_2O_4$ (nickel zinc ferrite) and $MnZnFe_2O_4$ (manganese zinc ferrite) nanoparticles in a viscous carrier ferromagnetic nanofluid slow down the axial velocity.

- Axial velocity reduces and the temperature field enhances rapidly for increasing values of β (ferromagnetic interaction) when magnetic dipole is present.

- The axial velocity and relative nano boundary layer of the ferromagnetic $NiZnFe_2O_4$-$C_2H_6O_2$, $NiZnFe_2O_4$-H_2O, $MnZnFe_2O_4$-$C_2H_6O_2$, $MnZnFe_2O_4$-H_2O, Fe_3O_4-$C_2H_6O_2$, and Fe_3O_4-H_2O nanofluids are decreasing functions of δ_h (conjugate parameter) and increasing function of temperature profile.

- The wall shear stress of the ferromagnetic $NiZnFe_2O_4$-$C_2H_6O_2$, $NiZnFe_2O_4$-H_2O, $MnZnFe_2O_4$-$C_2H_6O_2$, $MnZnFe_2O_4$-H_2O, Fe_3O_4-$C_2H_6O_2$, and Fe_3O_4-H_2O nanofluids enhances with parameters β (ferromagnetic interaction) and P_m (porosity).

- The fast devaluation in heat transfer rate is observed in presence of magnetic dipole.

References

[1] Schlichting, H., and Gersten, K., *Boundary layer theory springer-verlag*, Berlin, Heidelberg (2000).

[2] Bowles, R.S., Kolstad, J.J., Calo, J.M., and Andres, R.P., *Generation of molecular clusters of controlled size*, Surf. Sci. 106(1-3),(1981): 117-124.

[3] Choi, S.U.S, *Enhancing thermal conductivity of fluids with nanoparticles, Developments and applications of non-Newtonian flows*, D.A. Siginer and H.P. Wang, eds, 231(66), ASME, New York,(1995): 99-105.

[4] Buongiorno, J., *Convective transport in nanofluids*, ASME J. Heat Transfer 128,(2006): 240-250.

[5] Bowles, R.S., Kolstad, J.J., Calo, J.M., and Andres, R.P., *Heat transfer augmentation in a two-sided lid-driven differentially heated square cavity utilizing nanofluids*, Int. J. Heat Mass Transfer 50,(2007): 2002-2018.

[6] Kamali, R., and Binesh, A.R., *Numerical investigation of heat transfer enhancement using carbon nanotube-based non-Newtonian nanofluids*, Int. Commun. Heat Mass Transfer 37,(2010): 1153-1157.

[7] Nie, Z., Petukhova, A., and Kumacheva, E., *Properties and emerging applications of self-assembled structures made from inorganic nanoparticles*, Nat. Nanotechnol. 5(1),(2010): 15.

[8] Li, Z., Barnes, J.C., Bosoy, A., Stoddart, J.F., and Zink, J.I., *Mesoporous silica nanoparticles in biomedical applications*, Chem. Soc. Rev. 41(7),(2012): 2590-2605.

[9] Guo, Y., Cao, F., Lei, X., Mang, L., Cheng, S., and Song, J., *Fluorescent copper nanoparticles: recent advances in synthesis and applications for sensing metal ions*, Nanoscale. 8(9),(2016): 4852-4863.

[10] Ellahi, R., Hassan, M., and Zeeshan, A., *Shape effects of spherical and nonspherical nanoparticles in mixed convection flow over a vertical stretching permeable sheet*, Mech. Adv. Mater. Struc. 24(15),(2017): 1231-1238.

[11] Mahanthesh, B., Gireesha, B.J., Gorla, R.S., and Makinde, O.D., *Magnetohydrodynamic three-dimensional flow of nanofluids with slip and thermal radiation over a nonlinear stretching sheet: a numerical study*, Neural. Comput. Appl. 30(5),(2018): 1557-1567.

[12] Ghadikolaei, S.S., Hosseinzadeh, K., and Ganji, D.D., *MHD raviative boundary layer analysis of micropolar dusty fluid with graphene oxide (Go)-engine oil nanoparticle in a porous medium over a stretching sheet with joule heating effect*, Powder Technol. 338,(2018): 425-437.

[13] Surywanshi, P.L., Sonwane, S.H., Bhnvase, B.A., Ashokkumar, M., Pimplpure, M.S., and Gogate, P.R., *Synthesis of iron oxide nanoparticle in a continous flow spiral microreactor and Corning advanced flow reactor*, Green. Process. Synth. 7(1),(2018): 1-11.

[14] Ali, A., Sulaiman, M., Islam, S., Shah, Z., and Bonyah, E., *Three-dimensional magnetohydrodynamic (MHD) flow of Maxwell nanofluid containing gyrotactic micro-organisms with heat source/sink*, AIP Adv. 8(8),(2018): 085303.

[15] Khanafer, K., and Vafai, K., *Applications of nanofluids in porous medium*, J. Therm. Anal. Calorim. 4,(2018): 1-14.

[16] Shen, M., Chen, L., Zhang, M., and Liu, F., *A renovated Buongiorno's model for unsteady Sisko nanofluid with fractional Cattaneo heat flux*, Int. J. Heat. Mass. Tran. 126,(2018): 277-286.

[17] Pramuanjaroenkij, A., Tongkratoke, A., and Kaka, S., *Numerical study of mixing thermal conductivity models for nanofluid heat transfer enhancement*, J. Eng. Phys. Thermophys. 91(1),(2018): 104-114.

[18] Jahan, S., Sakidin, H., Nazar, R., and Pop, I., *Analysis of heat transfer in nanofluid past a convectively heated permeable stretching/shrinking sheet with regression and stability analyses*, Results Phys. 10,(2018): 395-405.

[19] Kashyap, D., and Dass, A.K., *Two-phase lattice Boltzmann simulation of natural convection in a Cu-water nanofluid-filled porous cavity: Effects of thermal*

boundary conditions on heat transfer and entropy generation, Adv. Powder Technol. 29(11),(2018): 2707-2724.

[20] Kasaiean, A., Sameti, M., Daneshazarian, R., Noori, Z., Adamian, A., and Ming, T., *Heat transfer network for a parabolic trough collector as a heat collecting element using nanofluid*, Renew. Energ. 123,(2018): 439-449.

[21] Shehzad, N., Zeeshan, A., and Ellahi, R., *Electroosmotic flow of MHD power law Al_2O_3-PVC nanofluid in a horizontal channel: Couette-Poiseuille flow model*, Commun. Theor. Phys. 69(6),(2018): 655.

[22] Javidi, M., Heydari, M., Attar, M.M., Haghpanahi, M., Karimi, A., Navidbakhsh, M., and Amanpour, S., *Cylindrical agar gel with fluid flow subjected to an alternating magnetic field during hyperthermia*, Int. J. Hyperther. 31(1),(2015): 33-39.

[23] Arulmurugan, R., Vaidyanathan, G., Sendhilnathan, S., and Jeyadevan, B., *Mn-Zn ferrite nanoparticles for ferrofluid preparation: study on thermal-magnetic properties*, J. Magn. Magn. Mater. 298(2),(2006): 83-94.

[24] Allendorf, M.D., Diver, R.B., Siegel, N.P., and Miller, J.E., *Two-step water splitting using mixed-metal ferrites: thermodynamic analysis and characterization of synthesized materials*, Energy Fuels. 22(6),(2008): 4115-4124.

[25] Nkurikiyimfura, I., Wang, Y., and Pan, Z., *Heat transfer enhancement by magnetic nanofluids-a review*, Renewable Sustainable Energy Rev. 21,(2013): 548-561.

[26] Seehra, M.S., Singh, V., Dutta, P., Neeleshwar, S., Chen, Y.Y., Chen, C.L., Chou, S.W., and Chen, C.C., *Size-dependent magnetic parameters of fcc FePt nanoparticles: applications to magnetic hyperthermia*, J. Phys. D: Appl. Phys. 43(14),(2010): 145002.

[27] Jeyadevan, B., Chinnasamy, C.N., Shinoda, K., Tohji, K., and Oka, H., *Mn-Zn ferrite with higher magnetization for temperature sensitive magnetic fluid*, J. Appl. Phys. 93(10),(2013): 8450-8452.

[28] Anupama, A.V., Kumaran, V., and Sahoo, B., *Magnetorheological fluids containing rod-shaped lithium-zinc ferrite particles: steady-state shear response*, Surf. Sci. 26,(2018): 5407-5419.

[29] Dinkar, D.K., Das, B., Gopalan, R., and Dehiya, B.S., *Effects of surfactant on the structural and magnetic properties of hydrothermally synthesized $NiFe_2O_4$ nanoparticles*, Mater. Chem. Phys. 218,(2018): 70-76.

[30] Alam, E.M.M., Rahman, M.M., and Uddin, M.S., *Study of exponential thermal boundary condition on unsteady magnetohydrodynamic convection in a square enclosure filled with Fe_3O_4-Water Ferrofluid*, Eng. Int. 6(1),(2018): 35-62.

[31] Alrashed, A.A., Karimipour, A., Bagherzadeh, S.A., Safaei, M.R., and Afrand, M., *Electro- and thermophysical properties of water-based nanofluids containing copper ferrite nanoparticles coated with silica: Experimental data, modeling through enhanced ANN and curve fitting*, Int. J. Heat Mass Tran. 127,(2018): 925-935.

[32] Pawar, R.A., Patange, S.M., Shitre, A.R., Gore, S.K., Jadhav, S.S., and Shirsath, S.E., *Crystal chemistry and single-phase synthesis of Gd 3+ substituted Co-Zn ferrite nanoparticles for enhanced magnetic properties*, RSC Adv. 8(44),(2018): 25258-25267.

[33] Gomes, G.A., da Costa, G.L., and da Silva Figueiredo, A.B.H., *Synthesis of ferrite nanoparticles $Cu_{1-x}Ag_xFe_2O_4$ and evaluation of potential antibacterial activity*, J. Mater. Sci. Technol. 7(3),(2018): 381-386.

[34] Han, J.K., and Choi, H.J., *Non-stoichiometric zinc-doped spinel ferrite nanoparticles with enhanced magnetic property and their magnetorheology*, Colloid. Polym. Sci. 296(2),(2018): 405-409.

[35] Singh, N.B., and Agarwal, A., *Preparation, characterization, properties and applications of nano zinc ferrite*, Mater. Today-Proc. 5(3),(2018): 9148-9155.

[36] Deraz, N.M., *Tailoring the physicochemical and magnetic properties of an Mn substituted cobalt ferrite system*, Interceram. 67(3),(2018): 14-19.

[37] Neuringer, J. L., *Some viscous flows of a saturated ferrofluid under the combined influence of thermal and magnetic field gradients*, Int. J. of Non-Linear Mech. 2(1),(1966): 123-137.

[38] Crane, L.J., *Flow past a stretching plate*, Z. Angew. Math. Phys. 4(21), (1970): 645-647.

[39] Andersson, H.I., and Valnes O.A., *Flow of a heated ferrofluid over a stretching sheet in the presence of a magnetic dipole*, Acta Mech. 2(128),(1998): 39-47.

[40] Tzirtzilakis, E.E., Kafoussias, N.G., and Raptis, A., *Numerical study of forced and free convective boundary layer flow of a magnetic fluid over a flat plate under the action of a localized magnetic field*, Z. Angew. Math. Phys. 54(61),(2010): 929-947.

[41] Sharma, D., and Sharma, R.C., *Effect of dust particles on thermal convection in ferromagnetic fluid saturating a porous medium*, J. Magn. Magn. Mater. 288,(2005): 183-195.

[42] Zeeshan, A., and Majeed A., *Heat transfer analysis of Jeffrey fluid flow over a stretching sheet with suction/injection and magnetic dipole effect*, Alex. Eng. J. 3,(2016): 2171-2181.

[43] Sharma, A. Sharma, D., and Sharma, R.C., *Effect of dust particles on thermal convection in a ferromagnetic fluid*, Z. Naturforsch A. 7(60),(2005): 494-502.

[44] Neuringer, J.L. and Rosensweig, R.E., *Ferrohydrodynamics*, Phys. Fluids. 12(7),(1964): 1927-1937.

[45] Kim, J.H., Seo, H.S., and Kim, Y.J., *Thermal-flow characteristics of ferrofluids in a rotating eccentric cylinder under external magnetic force*, Micromachines. 9(9),(2018): 457.

[46] Majeed, A., Zeeshan, A., Alamri, S.Z., and Ellahi, R., *Heat transfer analysis in ferromagnetic viscoelastic fluid flow over a stretching sheet with suction*, Neural Comput. Appl. 30(6),(2018): 1947-1955.

[47] Hussanan, A., Salleh, M.Z., and Khan, I., *Microstructure and inertial characteristics of a magnetite ferrofluid over a stretching/shrinking sheet using effective thermal conductivity model*, J. Mol. Liq. 255,(2018): 64-75.

[48] Jusoh, R., Nazar, R., and Pop, I., *Magnetohydrodynamic rotating flow and heat transfer of ferrofluid due to an exponentially permeable stretching/shrinking sheet*, J. Magn. Magn. Mater. 465,(2018): 365-374.

[49] Shafii, M.B., and Keshavarz, M., *Experimental study of internal forced convection of ferrofluid flow in non-magnetizable/magnetizable porous media*, Exp. Therm. Fluid. Sci. 96,(2018): 441-450.

[50] Astanina, M.S., Sheremet, M.A., Oztop, H.F., and Abu-Hamdeh, N., *MHD natural convection and entropy generation of ferrofluid in an open trapezoidal cavity partially filled with a porous medium*, Int. J. Mech. Sci. 136,(2018): 493-502.

[51] Van Atta, C.W., *The decay of turbulence in thermally stratified flow*, J. Fluid Mech. 210,(1990): 57-112.

[52] Foisal, A.A., and Alam, M., *Unsteady free convection fluid flow over an inclined plate in the presence of a magnetic field with thermally stratified high porosity medium*, J. Appl. Fluid. Mech. 9(3),(2016): 1467-1475.

[53] Antoniadis, P.D., and Papalexandris, M.V., *Numerical study of unsteady, thermally-stratified shear flows in superposed porous and pure-fluid domains*, Int. J. Heat Mass Transf. 96,(2016): 643-659.

[54] Besthapu, P., Haq, R.U., Bandari, S., and Al-Mdallal, Q.M., *Mixed convection flow of thermally stratified MHD nanofluid over an exponentially stretching surface with viscous dissipation effect*, J. Taiwan Inst. Chem. Eng. 71,(2017): 307-314.

[55] Rehman, K.U., Qaiser, A., Malik, M.Y., and Ali, U., *Numerical communication for MHD thermally stratified dual convection flow of Casson fluid yields by stretching cylinder*, Chin. J. Phys. 55(4),(2017): 1605-1614.

[56] Ahmed, N., Khan, U., and Mohyud-Din, S.T., *A theoretical investigation of unsteady thermally stratified flow of γAl_2O_3-H_2O and γAl_2O_3-$C_2H_6O_2$ nanofluids through a thin slit*, J. Phys. Chem. Solids 119,(2017): 296-308.

[57] Makinde, O.D., Sandeep, N., Ajayi, T.M., and Animasaun, I.L., *Numerical exploration of heat transfer and Lorentz force effects on the flow of MHD Casson fluid over an upper horizontal surface of a thermally stratified melting surface of a paraboloid of revolution*, Int. J. Nonlin. Sci. Num. 19(2-3),(2018): 93-106.

[58] Koriko, O.K., Animasaun, I.L., Reddy, M.G., and Sandeep, N., *Scrutinization of thermal stratification, nonlinear thermal radiation and quartic autocatalytic chemical reaction effects on the flow of three-dimensional Eyring-Powell alumina-water nanofluid*, MMMS 14(2),(2018): 261-283.

[59] Karim, A., Burnett, A., and Fawzia, S., *Investigation of stratified thermal storage tank performance for heating and cooling applications*, Energies 11(5),(2018): 1-15.

[60] Paradis, P.L., Rousse, D.R., Lamarche, L., Nesreddine, H., and Talbot, M.H., *One-dimensional model of a stratified thermal storage tank with supercritical coiled heat exchanger*, Appl. Therm. Eng. 134,(2018): 379-395.

[61] Gomez, M.A., Collazo, J., Porteiro, J., and Miguez, J.L., *Numerical study of an external device for the improvement of the thermal stratification in hot water storage tanks*, Appl. Therm. Eng. 144,(2018): 996-1009.

[62] Majumdar, R., Saha, S.K., and Singh, S., *Evaluation of transient characteristics of medium temperature solar thermal systems utilizing thermal stratification*, Appl. Energ. 224,(2018): 69-85.

[63] Kursun, B., and Okten, K., *Effect of rectangular hot water tank position and aspect ratio on thermal stratification enhancement*, Renew. Energ. 116,(2018): 639-646.

[64] Lawler, B., Lacey, J., Gralp, O., Najt, P., and Filipi, Z., *HCCI combustion with an actively controlled glow plug: The effects on heat release, thermal stratification, efficiency, and emissions*, Appl. Energ. 211,(2018): 809-819.

[65] Pilla, R.M., Williamson, C.E., Zhang, J., Smyth, R.L., Lenters, J.D., Brentrup, J.A., Knoll, L.B., and Fisher, T.J., *Browning-related decreases in water transparency lead to long-term increases in surface water temperature and thermal stratification in two small lakes*, J. Geophys. Res. Biogeo. 123(5),(2018): 1651-1665.

[66] Kandasamy, R., Dharmalingam, R., and Prabhu, K.S., *Thermal and solutal stratification on MHD nanofluid flow over a porous vertical plate*, Alexandria Eng. J. 57(1),(2018): 121-130.

[67] da Cunha, J.P., and Eames, P., *Compact latent heat storage decarbonisation potential for domestic hot water and space heating applications in the UK*, Appl. Therm. Eng. 134,(2018): 396-406.

[68] Merkin, J.H., *Natural-convection boundary-layer flow on a vertical surface with Newtonian heating*, Int. J. Heat Fluid Flow 15(5),(1994): 392-398.

[69] Salleh, M.Z., Nazar, R., and Pop, I., *Boundary layer flow and heat transfer over a stretching sheet with Newtonian heating*, J. Taiwan Inst. Chem. Eng. 41(6),(2010): 651-655.

[70] Qasim, M., Khan, I. and Shafie, S., *Heat transfer in a micropolar fluid over a stretching sheet with Newtonian heating*, PLoS One 8(4),(2013): e59393.

[71] Sarif, N.M., Salleh, M.Z., and Nazar, R., *Numerical solution of flow and heat transfer over a stretching sheet with Newtonian heating using the Keller box method*, Procedia Eng. 53,(2013): 542-554.

[72] Nadeem, S., Ahmad, S., and Muhammad, N., *Cattaneo-Christov flux in the flow of a viscoelastic fluid in the presence of Newtonian heating*, J. Mol. Liq. 237,(2017): 180-184.

[73] Imran, M.A., Riaz, M.B., Shah, N.A., and Zafar, A.A., *Boundary layer flow of MHD generalized Maxwell fluid over an exponentially accelerated infinite vertical surface with slip and Newtonian heating at the boundary*, Results Phys. 8,(2018): 1061-1067.

[74] Kamran, M., and Wiwatanapataphee, B., *Chemical reaction and Newtonian heating effects on steady convection flow of a micropolar fluid with second order slip at the boundary*, Eur. J. Mech. B. Fluids 71,(2018): 138-150.

[75] Mehmood, R., Rana, S., and Nadeem, S., *Transverse thermopherotic MHD Oldroyd-B fluid with Newtonian heating*, Results Phys. 8,(2018): 686-693.

[76] Kamran, M., Wiwatanapataphee, B., and Vajravelu, K., *Hall current, Newtonian heating and second-order slip effects on convective magneto-micropolar fluid flow over a sheet*, Int. J. Mod. Phys. C. 13,(2018): 1850090.

[77] Hussanan, A., Salleh, M.Z., Khan, I., and Tahar, R.M., *Heat and mass transfer in a micropolar fluid with Newtonian heating: an exact analysis*, Results Phys. 29(6),(2018): 59-67.

[78] Uddin, M.J., Sohail, A., Beg, O.A., and Ismail, A.M., *Numerical solution of MHD slip flow of a nanofluid past a radiating plate with Newtonian heating: a Lie group approach*, Alexandria Eng. J. 3,(2017): 1-10.

[79] Rao, A.S., Amanulla, C.H., Nagendra, N., Beg, O.A., and Kadir, A., *Hydromagnetic flow and heat transfer in a Williamson Non-Newtonian fluid from a*

horizontal circular cylinder with Newtonian heating, Int. J. Appl. Comp. Math. 3(4),(2017): 3389-3409.

[80] Nawaz, M., Zeeshan, A., Ellahi, R., Abbasbandy, S. and Rashidi, S., *Joules and Newtonian heating effects on stagnation point flow over a stretching surface by means of genetic algorithm and Nelder-Mead method*, Int. J. Numer. Methods Heat Fluid Flow 25(3),(2015): 665-684.

[81] Khan, A., Khan, D., Khan, I., Ali, F., Karim, F.U., and Imran, M., *MHD flow of sodium alginate-based Casson type nanofluid passing through a porous medium with Newtonian heating*, Sci. Rep. 8(1),(2018): 8645.

[82] Imran, M.A., Khan, I., Shah, N.A., and Aleem, M., *Applictions of noninteger Caputo time fractional derivative to natural convections flow subjects to arbitrary velocity and Newtonians heating*, Neurall Comput. Appll. 30(4),(2018): 1588-1599.

[83] Scott, S.K., *Chemical chaos*, Oxford University Press. 24,(1993).

[84] Gray, P., and Scott, S. K., *Chemical oscillations and instabilities: non-linear chemical kinetics*, Clarendon Press. Oxford University Press, 1990.

[85] Prasad, K.V., Vajravelu, K., Vaidya, H., and Datti, P.S., *Axisymmetric flow over a vertical slender cylinder in the presence of chemically reactive species*, Int. J. Appl. Comput. Math. 3(2),(2017): 663-678.

[86] Huang, M., Zhou, T., Wu, X., and Mao, J., *Distinguishing homogeneous-heterogeneous degradation of norfloxacin in a photochemical Fenton-like system (Fe_3O_4/UV/oxalate) and the interfacial reaction mechanism*, Water Res. 119,(2017): 47-56.

[87] Nadeem, S., Ahmad, S., Muhammad, N., and Mustafa, M.T., *Chemically reactive species in the flow of a Maxwell fluid*, Results Phys. 7,(2017): 2607-2613.

[88] Merkin, J.H., *A model for isothermal homogeneous-heterogeneous reactions in boundary-layer flow*, Math. Comput. Model. 24(8),(1996): 125-136.

[89] Chaudhary, M.A., and Merkin, J.H., *A simple isothermal model for homogeneous-heterogeneous reactions in boundary-layer flow. I Equal diffusivities*, Fluid Dyn. Res. 16(6),(1995): 311.

[90] Bachok, N., Ishak, A., and Pop, I., *On the stagnation-point flow towards a stretching sheet with homogeneous-heterogeneous reactions effects*, Commun. Nonlinear Sci. Numer. Simul. 16(11),(2011): 4296-4302.

[91] GKameswaran, P.K., Shaw, S., Sibanda, P., and Murthy, P.V.S.N., *Homogeneous-heterogeneous reactions in a nanofluid flow due to a porous stretching sheet*, Int. J. Heat Mass Transfer 57(2),(2013): 465-472.

[92] Khan, W.A. and Pop, I., *Flow near the two-dimensional stagnation-point on an infinite permeable wall with a homogeneous-heterogeneous reaction*, Commun. Nonlinear Sci. Numer. Simul. 15(11),(2010): 3435-3443.

[93] Chen, C.H., *Laminar mixed convection adjacent to vertical continuously stretching sheets*, Heat Mass Transf. 33,(1998): 471-476.

[94] Rashidi M.M., Ganesh N.V., Hakeem A.A., Ganga B., and Lorenzini G., *Influences of an effective Prandtl number model on nano boundary layer flow of $\gamma\ Al_2O_3$-H_2O and $\gamma\ Al_2O_3$-$C_2H_6O_2$ over a vertical stretching sheet*, Int. J Heat Mass Transf. 98,(2016): 616-623.

[95] Abel, M.S., Sanjayanand, E., and Nandeppanavar, M.M., *Viscoelastic MHD flow and heat transfer over a stretching sheet with viscous and ohmic dissipations*, Commun. Nonlinear Sci. Numer. Simul. 13(9),(2008): 1808-1821.

[96] Liao, S., *Beyond Perturbation: Introduction to Homotopy Analysis Method*, Chapman and Hall, CRC Press, Boca Raton, (2003).

[97] Liao, S., *Homotopy Analysis Method in Non-Linear Differential Equations*, Springer and Higher Education Press, Heidelberg (2012).

sources:

1 1% match (Internet from 18-Dec-2019)
https://www.mdpi.com/2227-9717/7/8/486/htm

2 1% match (publications)
Abbas Khan, Taza Gul, Zafar Zaheer, Iraj S Amiri. "The flow of ferromagnetic nanofluid over an extending surface under the effect of operative Prandtl model: A numerical study", Advances in Mechanical Engineering, 2019

3 < 1% match (publications)
Khan Md. Rabbi, M. Sheikholeslami, Anwarul Karim, Ahmad Shafee, Zhixiong Li, Iskander Tlili. "Prediction of MHD flow and entropy generation by Artificial Neural Network in square cavity with heater-sink for nanomaterial", Physica A: Statistical Mechanics and its Applications, 2019

4 < 1% match (publications)
Mahesha Narayana, L. S. Rani Titus, Annamma Abraham, Precious Sibanda. "Modelling micropolar ferromagnetic fluid flow due to stretching of an elastic sheet", Afrika Matematika, 2013

5 < 1% match (student papers from 09-Apr-2013)
Submitted to University of Pretoria on 2013-04-09

6 < 1% match (student papers from 05-Dec-2016)
Submitted to Universiti Teknologi Petronas on 2016-12-05

7 < 1% match (student papers from 01-Mar-2018)
Submitted to Higher Education Commission Pakistan on 2018-03-01

8 < 1% match (student papers from 22-Dec-2016)
Submitted to Universiti Teknologi Petronas on 2016-12-22

9 < 1% match (publications)
I. Muhaimin, R. Kandasamy. "Local Nonsimilarity Solution for the Impact of a Chemical Reaction in an MHD Mixed Convection Heat and Mass Transfer Flow over a Porous Wedge in the Presence Of Suction/Injection", Journal of Applied Mechanics and Technical Physics, 2010

10 < 1% match (publications)
Misbah Ijaz, Muhammad Ayub. "Simulation of magnetic dipole and dual stratification in radiative flow of ferromagnetic Maxwell fluid", Heliyon, 2019

11 < 1% match (student papers from 30-Dec-2013)
Submitted to Universiti Sains Malaysia on 2013-12-30

12 < 1% match (student papers from 29-Oct-2015)
Submitted to Indian Institute of Technology, Madras on 2015-10-29

13 < 1% match (publications)